ISSN 8755-6839

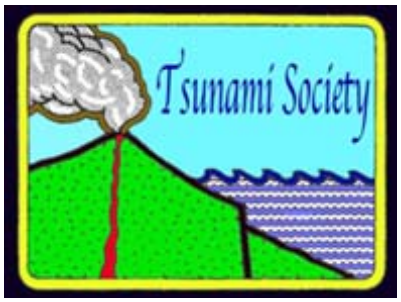

SCIENCE OF **TSUNAMI HAZARDS**

Journal of Tsunami Society International

Volume 35 **Number 3** **2016**

Copyright © 2016 - TSUNAMI SOCIETY INTERNATIONAL
WWW.TSUNAMISOCIETY.ORG

TSUNAMI SOCIETY INTERNATIONAL, 1741 Ala Moana Blvd. #70, Honolulu, HI 96815, USA.

SCIENCE OF TSUNAMI HAZARDS is a CERTIFIED OPEN ACCESS Journal included in the prestigious international academic journal database DOAJ, maintained by the University of Lund in Sweden with the support of the European Union. SCIENCE OF TSUNAMI HAZARDS is also preserved, archived and disseminated by the National Library, The Hague, NETHERLANDS, the Library of Congress, Washington D.C., USA, the Electronic Library of Los Alamos, National Laboratory, New Mexico, USA, the EBSCO Publishing databases and ELSEVIER Publishing in Amsterdam. The vast dissemination gives the journal additional global exposure and readership in 90% of the academic institutions worldwide, including nation-wide access to databases in more than 70 countries.

OBJECTIVE: Tsunami Society International publishes this interdisciplinary journal to increase and disseminate knowledge about tsunamis and their hazards.

DISCLAIMER: Although the articles in SCIENCE OF TSUNAMI HAZARDS have been technically reviewed by peers, Tsunami Society International is not responsible for the veracity of any statement, opinion or consequences.

EDITORIAL STAFF
Dr. George Pararas-Carayannis, Editor
mailto:drgeorgepc@yahoo.com

EDITORIAL BOARD
Dr. Charles MADER, Mader Consulting Co., Colorado, New Mexico, Hawaii, USA
Dr. Hermann FRITZ, Georgia Institute of Technology, USA
Prof. George CURTIS, University of Hawaii -Hilo, USA
Dr. Tad S. MURTY, University of Ottawa, CANADA
Dr. Zygmunt KOWALIK, University of Alaska, USA
Dr. Galen GISLER, NORWAY
Prof. Kam Tim CHAU, Hong Kong Polytechnic University, HONG KONG
Dr. Jochen BUNDSCHUH, (ICE) COSTA RICA, Royal Institute of Technology, SWEDEN
Dr. Yurii SHOKIN, Novosibirsk, RUSSIAN FEDERATION
Dr. Radianta Triatmadja - Tsunami Research Group, Universitas Gadjah Mada, Yogyakarta, INDONESIA

TSUNAMI SOCIETY INTERNATIONAL, OFFICERS
Dr. George Pararas-Carayannis, President;
Dr. Tad Murty, Vice President;
Dr. Carolyn Forbes, Secretary/Treasurer.

Submit manuscripts of research papers, notes or letters to the Editor. If a research paper is accepted for publication the author(s) must submit a scan-ready manuscript, a Doc, TeX or a PDF file in the journal format. Issues of the journal are published electronically in PDF format. There is a minimal publication fee for authors who are members of Tsunami Society International for three years and slightly higher for non-members. Tsunami Society International members are notified by e-mail when a new issue is available. Permission to use figures, tables and brief excerpts from this journal in scientific and educational works is granted provided that the source is acknowledged.

Recent and all past journal issues are available at: http://www.TsunamiSociety.org CD-ROMs of past volumes may be purchased by contacting Tsunami Society International at postmaster@tsunamisociety.org Issues of the journal from 1982 thru 2005 are also available in PDF format at the U.S. Los Alamos National Laboratory Library http://epubs.lanl.gov/tsunami/

ISSN 8755-6839

SCIENCE OF **TSUNAMI HAZARDS**

Journal of Tsunami Society International

Volume 35 **Number 3** **2016**

LANDSLIDE-TYPE TSUNAMI MODELLING BASED ON THE NAVIER - STOKES EQUATIONS

A.S. Kozelkov [1,2)], A.A. Kurkin[2)], E.N. Pelinovsky[2-4)], E.S. Tyatyushkina[1)], V.V. Kurulin[1)], N.V. Tarasova[1)]

1) Russian Federal Nuclear Center, All-Russian Research Institute of Experimental Physics, Sarov, Russia
2) Nizhny Novgorod State Technical University n.a. R. Alekseyev, Nizhny Novgorod, Russia
3) Institute of Applied Physics, Nizhny Novgorod, Russia
4) National Research University – Higher School of Economics, Moscow, Russia

ABSTRACT

The paper presents a unified computing technology for all stages of landslide-type tsunami. The computing technology is based on the numerical solution of the Navier – Stokes equations for multiphase flows. The method of numerical solution of the Navier – Stokes equations uses a fully implicit algorithm. This algorithm removes stiff restrictions on the time steps and allows simulating a tsunami propagation in arbitrarily large water basins. The basic sampling equation formulas, coefficient types as well as the basic steps of the computational procedure are presented. The landslide is modeled by a single phase with its density and viscosity, which is separated by the interface from water and air phases. A parallel algorithm of the method implementation based on an algebraic multigrid method is proposed for the effective usage of the method to calculate the tsunami in large water areas. The multigrid method of implementation is based on algorithms of global level and cascading collection. These algorithms do not impose restrictions on the scale parallelization and allow the use of the proposed technology in petaflop class systems. It shows the possibility of

simulating all the stages of the landslide-type tsunamis: generation, propagation and runup. The verification of the method is carried out by using the tests provided by the experimental data. The mechanism of bathymetric data accounting and the technology of constructing three-dimensional grid models are described. The results of the comparison with the non-linear dispersion theory are presented for the historical tsunami that resulted from a volcanic eruption on the island of Montserrat, the Caribbean. The results of this comparison are in good agreement.

1. INTRODUCTION

Tsunami database contains more than 2,200 registered events in the world and more than 9,000 observations of wave heights on a shore (http://tsun.sscc.ru/hiwg). More than 10% of them are tsunamis generated by underwater and aerial landslides, and 5% are generated by volcanic sources, to be more precise, by pyroclastic flows formed as a result of a volcanic explosion. According to the accumulated data, tsunamis generated by landslides have the highest runup heights, which can reach several hundred meters. The most famous landslide-type tsunamis are events in Alaska (Lituya Bay) (1853, 1936, 1958), Norway (1936) and Greenland (2000) (Rabinovich et al., 2003; Fine et al., 2005; Papadopoulos & Kortekaas, 2005). The greatest tsunami wave height of 60 meters was observed in Lituya Bay on 10 July, 1958 with a maximum splash in the bay itself 525 meters. The review of historical landslides and tsunamis generated by them can be found in (Langford, 2007; Papadopoulos & Kortekaas, 2005).

Waves excited by underwater and aerial landslides achieve the maximum possible runup directly near the source at a distance of 10-15 km along the coastline (Papadopoulos & Kortekaas, 2005). However, the tsunami of this kind can propagate significantly further. They can keep their destructive potential for hundreds of kilometers.

Tsunamigenic landslides can be divided into three types: aerial, partially submerged in the water and submarine. The initial position of the landslide is the basis for selecting physical and mathematical models suitable to describe tsunami generation and propagation. It is advisable to use a three-phase system: fluid-air-landslide to describe aerial and partially underwater landslides, whereas for underwater landslides it is enough to use a two-phase or a two-layer model with different density layers. The landslide itself is modeled by a non-deformable rigid body or a system of such bodies as well as by incompressible fluid or a separate layer with its own values of density and viscosity coefficients (Fedotova et al, 2004; Watts & Grilli, 2003; Heinrich et al, 1998; Imamura & Imteaz, 1995; Zahibo et al, 2010; Nikolkina et al, 2010; Didenkulova et al, 2010, 2011).

Surface waves generated by landslides are specific in their own way. The formation of the wave in the coastal zone takes a fairly long period of time comparable to the time of the landslide movement. The characteristic landslide size is often comparable with the depth. Unlike the tsunamis of seismic origin the landslide-type tsunamis are shorter (Dutykh & Dias, 2009), which requires considering wave dispersion. To simulate these waves nonlinear-dispersive shallow water equations are used which are able to reproduce the dispersion. These equations are solved by finite-difference methods built on the basis of the second-order accuracy schemes (Watts & Grilli, 2003). However, these systems include mixed higher order derivatives. Due to that, building efficient numerical algorithms to solve them it is

not a trivial task. The use of nonlinear dispersive equations for simulating landslide tsunamis is discussed in (Fedotova et al, 2004; Gusev et al., 2013).

It is worth noting that the type of landslide tsunami is paid enough attention to. A large series of experimental studies (Langford, 2007; Watts & Grilli, 2003; Sælevik et al., 2009; Fritz et al., 2009; Horrillo et al., 2013; Mohammed & Frits 2010; Mohammed, 2010)[1], and some theoretical works (Langford, 2007; Papadopoulos& Kortekaas, 2005; Fedotova et al., 2004; Watts & Grilli, 2003; Imamura & Imteaz, 1995; Dutykh & Dias, 2009; Gusev et al., 2013; Beizel et al., 2011; Harbitz et al., 2006) have allowed substantial progress in the development of numerical methods for tsunami calculation.

Besides experimental data, there are analytical solutions available for calibration and testing the developed methods (Pelinovsky, 2003; Okal & Synolakis, 2003; Didenkulova et al., 2010). Numerous articles discuss the results of historical landslide type tsunami simulation (Heinrich et al, 1998; Rabinovich et al, 2003; Fine et al, 2005; Sælevik et al, 2009; Fritz et al, 2009; Horrillo et al, 2013; Macías et al, 2015). The study of the various effects accompanying this phenomenon are described in (Pelinovsky, 2003; Watts & Grilli, 2003; Fedotova et al, 2004; Harbitz et al, 2006; Didenkulova et al, 2010; Beizel et al, 2011).

According to (Lynett, 2010) two approaches must be used to describe landslide-type tsunami formation correctly: the solution of fully 3D hydrodynamics equations or a simplified system based on them which is the result of depth integration. Depth integration, in fact, eliminates the vertical coordinate and reduces a 3D system to 2D, which serves as the basis for an NLSW (nonlinear shallow-water) class models. This class of models is well established in modeling seismic tsunami propagation over long distances. The use of NLSW models for landslide-type tsunami leads to the incorrect description of wave form and propagation time. It is caused by shorter wave generation in comparison with seismic sources (Lynett, 2010). For the majority of landslide-type tsunami it is more reasonable to use the Boussinesq equations, although they also have limitations (Watts et al, 2003). The use of 3D models to generate a landslide-type tsunami is reduced to the use of special systems on the basis of the Laplace equation (Cecioni & Bellotti, 2010 ; Grilli et al, 2002). An attempt to use three-dimensional models based on the fully Navier-Stokes equations is represented in a few works (Horrillo et al, 2013; Ma et al, 2013; Liu et al., 2005) due to their computational cost. However, in recent years there has been a significant increase in computing power and their affordability, so the development and application of these models is becoming an urgent task. The use of the Navier-Stokes equations together with the equation for calculating deformable landslide motion (Ma et al., 2013). LES (Large Eddy Simulation) approach to this class of problems (Liu et al., 2005) seems uncertain due to very strict requirements for the used numerical schemes and the calculation of the cascade transfer of turbulent kinetic energy for vortex structures of different scales (Kozelkov et al., 2016; Kozelkov & Kurulin, 2015). In (Horrillo et al., 2013) a simplified 3D model was used to generate the landslide-type tsunami source in the Gulf of Mexico. The use of a complete 3D model to calculate all tsunami waves stages including the runup seems promising enough. At present, to calculate the propagation (including formation) and runup the multi-layer models are used (Lynett & Liu, 2005): one model for propagation, and the other for the runup calculation. The review of physical

[1]Paper [14] gives an extensive bibliography on the experimental and analytical studies of landslide-type tsunami.

and mathematical models currently used to simulate the landslide-type tsunami is presented in (Mohammed, 2010).

The main difficulty in using the Navier-Stokes equations in scientific and industrial applications is their significant computational cost. The current system study is aimed at developing the methods of hydrodynamic calculation acceleration as well as at improving their accuracy (Volkov et al, 2013; Kozelkov et al, 2013; Kozelkov et al., 2016).

This paper presents a computed technique for landslide-type tsunami calculation on the basis of a fully implicit method of solution fully 3D Navier-Stokes equations which describe multiphase flows. The proposed method significantly weakens the demand for the time steps, which is one of the main advantages in the simulation of tsunami propagation over long distances. The fully implicit scheme also proves very stable. The algorithm for accelerating the convergence of the proposed method using multigrid technologies is presented in the paper. The basic sample formulae, the stages of the computational procedure and the algorithm for the bathymetric data accounting are given. The efficiency of the technology is tested on the known experimental data. The possibility of using the computed technology to calculate all landslide tsunami stages and to simulate tsunami in any part of the World Ocean is demonstrated in the paper. Section 2 presents the basic model equations and methodology of their numerical solution. The results of the proposed methodology validation in problems of tsunami generation which is the result of surface and underwater landslides having experimental data are given in Section 3. Section 4 presents the technology of three-dimensional grid model construction in the World Ocean with the detailed areas of the slide, runup and tsunami propagation. Section 5 describes the technology of calculation acceleration based on the algebraic multigrid method. Section 6 presents the landslide tsunami simulation results using different approaches from the source and with the simulated pyroclastic flow slide within the Navier - Stokes equations. The obtained results are summarized in Section 7.

2. BASIC MODEL EQUATIONS AND NUMERICAL SOLUTION METHOD

Let us consider the “air-water” system as a set of two incompressible media separated by the interface. We will use the one-velocity approximation, in which the continuity equation and the equation of momentum conservation are the same for both water and air. These equations are solved for the resultant medium, the properties of which are linearly dependent on the volume fraction (Hirt & Nichols, 1981). This approach is quite widespread and gives good results in solving problems with a free surface (Ubbink, 1997) including those for tsunami waves (Horrillo et al, 2013; Kozelkov et al., 2015; Kozelkov & Pelinovsky, 2016). In the framework of this approximation the motion is described by the Navier-Stokes equations, including equations of continuity, momentum conservation, as well as the equation for the volume fraction of the phases (Kolev, 2007; Volkov & Emelyanov, 2008):

$$\begin{cases} \nabla \cdot \mathbf{u} = 0, \\ \dfrac{\partial}{\partial t} \sum\limits_k \alpha^{(k)} \rho^{(k)} \mathbf{u} = -\nabla \cdot \sum\limits_k \left(\alpha^{(k)} \rho^{(k)} \mathbf{u}\mathbf{u} \right) + \nabla \cdot \sum\limits_k \left(\alpha^{(k)} \mu^{(k)} \nabla \mathbf{u} \right) - \nabla p + \sum\limits_k \alpha^{(k)} \rho^{(k)} \mathbf{g}, \\ \dfrac{\partial}{\partial t} \alpha^{(k)} \rho^{(k)} + \nabla \cdot \left(\alpha^{(k)} \rho^{(k)} \mathbf{u} \right) = 0, \end{cases} \qquad (1)$$

here $\mathbf{u}$ is a three-dimensional velocity vector $\rho^{(k)}$ is density of k-phase, and $\alpha^{(k)}$ is its volume fraction ($\sum\limits_k \alpha_k = 1$), p is pressure, $\mu^{(k)}$ is molecular viscosity of k-phase, $\mathbf{g}$ is gravity acceleration. This system is solved directly without the use of Reynolds averaging and the subsequent closure of the turbulence model. This allows solving turbulent structures, the minimum scale of which is determined by the grid resolution.

System sampling (1) can be carried out by any known method. The best choice is the finite volume method (Ubbink, 1997; Kozelkov & Kurulin, 2015) which possesses good conservative properties and enables sampling complex computational areas on arbitrary unstructured grids with cells of arbitrary shape. The main difficulty in the numerical solution of the system (1) is to determine the connection of the pressure field with the velocity field. The procedure of matching the pressure field with a rate field should lead to the simultaneous satisfaction of the continuity and momentum conservation equations. The most common methods are SIMPLE type methods based on pressure correction procedure, or the principle of splitting the unknown quantities (Ferziger & Peric, 2001; Kozelkov et al, 2013). For the SIMPLE-procedure the equation for the volume fraction and the mass forces is omitted, a cell P with the faces $f = nb(P)$ is considered, and the system of equations (1) is written in a discrete form:

$$\begin{cases} \sum\limits_{f=nb(P)} \mathbf{u}_f^n S_f = 0, \\ \sum\limits_k \alpha^{(k)} \rho^{(k)} \dfrac{\mathbf{u}^n - \mathbf{u}^{n-1}}{\tau} V = - \sum\limits_{f=nb(P)} \sum\limits_k \alpha^{(k)} \rho_f^{(k)} \mathbf{u}_f^{n-1} \mathbf{u}_f^n S_f + \sum\limits_{f=nb(P)} \sum\limits_k \alpha^{(k)} \mu_f^{(k)} \nabla \mathbf{u}_f^n S_f - \\ - \sum\limits_{f=nb(P)} p_f^n S_f + \sum\limits_k \alpha^{(k)} \rho^{(k)} \mathbf{g} V, \end{cases} \qquad (2)$$

where n is time layer, τ is time step, S_f is the area of the interface f between the control volumes of the computational grid (Fig. 1), $\mathbf{u}_f$ – is the value of the velocity on the edge (hereinafter, the index f means the affiliation of a value to a face), $nb(P)$ – is the number of cell edges (in this case, cell ***P***), see Fig. 1.

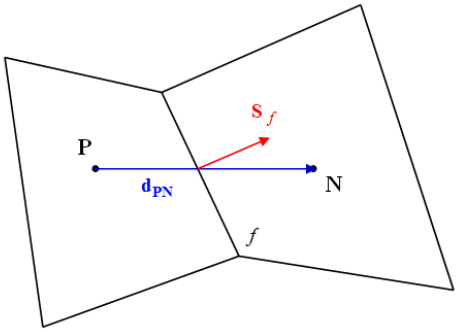

Fig. 1. Adjacent control volumes of the computational grid

The solution of system (1) by the SIMPLE algorithm assumes that the equation for the transfer of volume fractions (n – 1) for the volume fraction $\alpha^{(n)} = 1 - \sum_{k \neq n} \alpha^{(k)}$ of phases k is solved separately from continuity and momentum conservation equations. In the classic formulation of the SIMPLE algorithm the connection of velocity and pressure is carried out semi-implicitly. It takes place through the use of pressure from the previous iteration step, which often leads to slow the solution convergence. To improve the efficiency of work and the SIMPLE algorithm convergence modifications that best adapt to the velocity and pressure fields are developed. One such modification is a combined algorithm for solving velocity and pressure (Chen & Przekwas, 2010). The combination is done by implicit sampling of the pressure gradient and mass flow in the conservation of momentum and continuity equations. That helps to avoid the steps of predictor and corrector. Thus obtained implicit coefficients are summed into a single diagonally dominant matrix solved by using multigrid methods (Volkov et al, 2013; Kozelkov et al, 2013; Kozelkov et al, 2016; Tai & Zhao, 2003).

For the combined algorithm system solutions (1) the system of equations (2) is rewritten in the form of:

$$\begin{cases} \sum\limits_{f=nb(P)} \left\{ \overline{\mathbf{u}_f^n} + \overline{\mathbf{D}_f} \left[\left(\overline{\nabla p_f^{n-1}} \right) - \left(\nabla p_f^n \right) \right] \right\} S_f = 0, \\ \sum\limits_k \alpha^{(k)} \rho^{(k)} \dfrac{\mathbf{u}^n - \mathbf{u}^{n-1}}{\tau} V = - \sum\limits_{f=nb(P)} \sum\limits_k \alpha^{(k)} \rho_f^{(k)} \mathbf{u}_f^{n-1} \mathbf{u}_f^n S_f + \sum\limits_{f=nb(P)} \sum\limits_k \alpha^{(k)} \mu_f^{(k)} \nabla \mathbf{u}_f^n S_f - \\ - \sum\limits_{f=nb(P)} p_f^n S_f + \sum\limits_k \alpha^{(k)} \rho^{(k)} \mathbf{g} V, \end{cases} \quad (3)$$

here, the "upper line" indicates that the edge value is obtained by interpolation of the adjacent control volumes. The continuity equation in the system (3) uses the Rhie-Chow correction (Rhie & Chow, 1983) which levels the difference of pressure gradient approximation in the continuity and momentum conservation equations. The amendment also links the velocity and pressure fields at the simultaneous solution of continuity and motion equations.

To implement the fully implicit algorithm for the solution of (3) can be rewritten in its algebraic form:

$$\begin{cases} \sum\limits_{j\in\{p,u,v,w\}} a_P^{pj} j_P + \sum\limits_{N=NB(P)} \left[\sum\limits_{j\in\{p,u,v,w\}} a_N^{pj} j_N \right] = b_P^p, \\ \sum\limits_{j\in\{p,u,v,w\}} a_P^{ij} j_P + \sum\limits_{N=NB(P)} \left[\sum\limits_{j\in\{p,u,v,w\}} a_N^{ij} j_N \right] = b_P^i, \; i = \{u,v,w\}. \end{cases} \tag{4}$$

The summation over the index «*j*» for the first equation of the system (4) – continuity equation, gives general matrix coefficients to calculate the pressure in the control volume of the discrete model. These coefficients are:

$$a_N^{pp} = \frac{\left(\overline{\mathbf{D}_f}\mathbf{S}_f\right)\mathbf{S}_f}{\mathbf{S}_f \cdot \mathbf{d}_{PN}}, \quad a_P^{pp} = -\sum_{f=nb(P)} a_f^{pp},$$

$$a_N^{pu} = \left(1-\lambda_f\right)S_f^x, \quad a_N^{pv} = \left(1-\lambda_f\right)S_f^y, \quad a_N^{pw} = \left(1-\lambda_f\right)S_f^z, \tag{5}$$

$$a_P^{pu} = \sum_{f=nb(P)} \left|\lambda_f S_f^x\right|, \; a_P^{pv} = \sum_{f=nb(P)} \left|\lambda_f S_f^y\right|, \; a_P^{pw} = \sum_{f=nb(P)} \left|\lambda_f S_f^z\right|.$$

For these coefficients, a non-orthogonal correction algorithm is used (Jasak, 1996), allowing to correct the calculation on arbitrary unstructured grids. The formula of calculating the edge pressure by using linear interpolation from the values in the center cells is also used (Ferziger & Peric, 2001):

$$p_f = \lambda_f p_P + \left(1-\lambda_f\right)p_N. \tag{6}$$

For the first equation of the system (4) the right side has the form:

$$b_p^p = \sum_{f=nb(P)} \overline{\mathbf{D}_f \nabla p_f} \cdot \mathbf{S}_f - \overline{\mathbf{D}_f} \nabla p_f \cdot \left(\mathbf{S}_f - \frac{\mathbf{S}_f \cdot \mathbf{S}_f}{\mathbf{S}_f \cdot \mathbf{d}_{PN}} \mathbf{d}_{PN} \right). \tag{7}$$

The summation over the index «*i*» for the second equation of the system (4) – for the conservation momentum equation - gives the total matrix system coefficients to calculate the velocity component:

$$a_N^{uu} = a_N^{vv} = a_N^{ww} = \sum_k \alpha_f^{(k)} \mu_f \frac{\mathbf{S}_f \cdot \mathbf{S}_f}{\mathbf{S}_f \cdot \mathbf{d}_{PN}} + \min\left(0, \sum_k \alpha_f^{(k)} \rho_f^{(k)} S_f\right). \tag{8}$$

The first term of (8) refers to the diffusion term, and the total matrix system coefficients have the form:

$$a_N^{up} = (1-\lambda_f)S_f^x,\ a_N^{vp} = (1-\lambda_f)S_f^y,\ a_N^{wp} = (1-\lambda_f)S_f^z,$$
$$a_P^{up} = \sum_{f=nb(P)} \lambda_f S_f^x,\ a_P^{vp} = \sum_{f=nb(P)} \lambda_f S_f^y, a_P^{wp} = \sum_{f=nb(P)} \lambda_f S_f^z. \quad (9)$$

As well as for the coefficients (5), a non-orthogonal correction algorithm for recording is used.

The second term of the expressions (7) is a convective component, which is approximated by any known differential scheme applicable on arbitrary unstructured grids (Volkov et al., 2013; Kozelkov et al, 2015, 2016). Commonly used is an upwind difference (UD) or a counter-flow scheme with linear interpolation (linear upwind differences, LUD), the QUICK scheme, the central difference scheme (CD), the NVD family schemes (Normalized Variable Diagram), a hybrid scheme in which all the above mentioned schemes are mixed with a counter-flow scheme to increase monotony.

Non-stationary term sampling can be carried out by one of the known implicit schemes (Jasak, 1996; Ferziger & Peric, 2001). The contribution of diffusion and convection terms of conservation momentum equations applies to diagonal coefficients of the general matrix system, which, considering the non-stationary sampled term using the Euler scheme, have the form:

$$a_P^{uu} = -\sum_{N=NB(P)} a_N^{uu} + \sum_k \alpha_P^{(k)}\rho_P^{(k)}\frac{V}{\tau},$$
$$a_P^{vv} = -\sum_{N=NB(P)} a_N^{vv} + \sum_k \alpha_P^{(k)}\rho_P^{(k)}\frac{V}{\tau}, \quad (10)$$
$$a_P^{ww} = -\sum_{N=NB(P)} a_N^{ww} + \sum_k \alpha_P^{(k)}\rho_P^{(k)}\frac{V}{\tau}.$$

For the second equation of (4) the right-hand side has the form:

$$b_p^u = \sum_{f=nb(P)} \left[\nabla u \cdot \mu_f \cdot \left(\mathbf{S}_f - \frac{\mathbf{S}_f \cdot \mathbf{S}_f}{\mathbf{S}_f \cdot \mathbf{d}_{PN}}\mathbf{d}_{PN}\right)\right] + \sum_k \alpha_P^{(k)}\rho_P^{(k)}u_P\frac{V}{\tau} + \sum_k \alpha^{(k)}\rho^{(k)}g_x V,$$
$$b_p^v = \sum_{f=nb(P)} \left[\nabla v \cdot \mu_f \cdot \left(\mathbf{S}_f - \frac{\mathbf{S}_f \cdot \mathbf{S}_f}{\mathbf{S}_f \cdot \mathbf{d}_{PN}}\mathbf{d}_{PN}\right)\right] + \sum_k \alpha_P^{(k)}\rho_P^{(k)}v_P\frac{V}{\tau} + \sum_k \alpha^{(k)}\rho^{(k)}g_y V, \quad (11)$$
$$b_p^w = \sum_{f=nb(P)} \left[\nabla w \cdot \mu_f \cdot \left(\mathbf{S}_f - \frac{\mathbf{S}_f \cdot \mathbf{S}_f}{\mathbf{S}_f \cdot \mathbf{d}_{PN}}\mathbf{d}_{PN}\right)\right] + \sum_k \alpha_P^{(k)}\rho_P^{(k)}w_P\frac{V}{\tau} + \sum_k \alpha^{(k)}\rho^{(k)}g_z V.$$

Thus, the combined system of linear algebraic equations of the fully implicit algorithm for the simulation of a multiphase flow is as follows:

$$\begin{bmatrix} a_P^{pp} & a_P^{pu} & a_P^{pv} & a_P^{pw} \\ a_P^{up} & a_P^{uu} & a_P^{uv} & a_P^{uw} \\ a_P^{vp} & a_P^{vu} & a_P^{vv} & a_P^{vw} \\ a_P^{wp} & a_P^{wu} & a_P^{wv} & a_P^{ww} \end{bmatrix} \begin{bmatrix} p_P \\ u_P \\ v_P \\ w_P \end{bmatrix} + \sum_{N=NB(P)} \begin{bmatrix} a_N^{pp} & a_N^{pu} & a_N^{pv} & a_N^{pw} \\ a_N^{up} & a_N^{uu} & a_N^{uv} & a_N^{uw} \\ a_N^{vp} & a_N^{vu} & a_N^{vv} & a_N^{vw} \\ a_N^{wp} & a_N^{wu} & a_N^{wv} & a_N^{ww} \end{bmatrix} \begin{bmatrix} p_N \\ u_N \\ v_N \\ w_N \end{bmatrix} = \begin{bmatrix} b_P^p \\ b_P^u \\ b_P^v \\ b_P^w \end{bmatrix}. \quad (12)$$

This system is written to calculate the total velocity and pressure of the multiphase flow, but it can be generalized in case each phase has its own speed and physical properties such as compressibility and turbulence. These generalizations will be held in further.

To simulate the phase boundaries after solving the system (12), the equation of volume fraction transfer is solved (third equation (1)), which can be solved for (n – 1) the volume fractions of phases. Its sampling by the finite volume method is carried out according to the scheme completely similar to the one used for the conservation momentum equation. To approximate the convective term of volume fraction transfer, equation M-CICSAM scheme (Waclawczyk & Koronowicz, 2008) is used. It refers to a class of compression schemes of high resolution; it ensures the lowest possible thickness of the interface and preserves the volume fraction distribution under parallel transfer and rotation.

In the algebraic form the given system of equations for the k-phase is as follows:

$$a_P^{(k)}\alpha_P^{(k)} + \sum_{N=NB(P)} a_N^{(k)}\alpha_N^{(k)} = b_P^{(k)}. \quad (13)$$

The coefficients of the matrix of the equation implicit solution (13) are of the form:

$$\begin{aligned} a_N^{(k)} &= \min\left(0, u_f^{(n-1)} S_f\right) \quad a_P^{(k)} = -\sum_{N=NB(P)} a_N^{(k)} + \frac{V}{\tau}, \\ b_P^{(k)} &= -u_f^{(n-1)} S_f \cdot \left(\alpha_{MC}^{(k)} - \alpha_{UD}^{(k)}\right) + \frac{V}{\tau}\alpha_P^{(k),n-1}, \end{aligned} \quad (14)$$

where $\alpha_{MC}^{(k)}$, $\alpha_{UD}^{(k)}$ are values of the volume fraction on the edge found by MCICSAM scheme and, the counter-flow scheme, respectively, $\alpha_P^{(k),n-1}$ is the value of the volume fraction on the previous time step. These terms are obtained by a non-orthogonal correction along with sampling.

For the numerical solution the resulting equation system must be supplemented by initial and boundary conditions. On solid walls (such as the bottom of the basin), the pressure and the volume fraction gradient and the speed is zero: $\frac{\partial p}{\partial n} = 0$, $\frac{\partial \alpha_k}{\partial n} = 0$, $\mathbf{u} = 0$.

On the «free» borders static pressure is fixed, velocity and volume fraction gradients are equal to zero: $\frac{\partial u}{\partial n} = 0$, $\frac{\partial v}{\partial n} = 0$, $\frac{\partial w}{\partial n} = 0$, $\frac{\partial \alpha_k}{\partial n} = 0$. In modeling geophysical problems the upper limit should be placed high enough to avoid “spilling” water from the computational domain.

Initially, water and air are at rest: $u_0 = v_0 = w_0 = 0$, the pressure distribution is hydrostatic, i.e. satisfies the equation:

$$\nabla p = \mathbf{g} \sum_k \rho^{(k)} \alpha^{(k)} \ . \tag{15}$$

The volume fraction of phases (e.g. water and air) is determined in accordance with a predetermined level of the free surface position.

The calculation of the landslide movement in this model is carried out by means of a separate phase having its own density and viscosity, as well as water and air, i.e. a three-phase hydrodynamic system is obtained. Additional boundary conditions for landslide modeling are not required; all interactions with the liquid and air are modeled by the corresponding terms of the original system of equations. The fully implicit formulation of the numerical scheme relieves severe restrictions on the time step and ensures the stability of the iterative process at the maximum possible Courant number.

The presented method is implemented in the LOGOS software package - a software product designed to solve conjugated three-dimensional problems of convective heat transfer, aerodynamics and hydrodynamics on parallel computers (Betelin et al, 2014; Kozelkov et al, 2016). The LOGOS software package has successfully been verified and shown quite good results in a series of different hydrodynamic problems (Volkov et al, 2013; Kozelkov et al, 2013; Betelin et al, 2014) including turbulent and unsteady flow calculations (Kozelkov et al, 2015, 2016), as well as tsunami waves of cosmogenic origin (Kozelkov & Pelinovsky, 2016; Kozelkov et al., 2015). All the calculations in this article are conducted by using the LOGOS software package.

3. VERIFICATION OF THE NUMERICAL MODEL

The proposed methodology can be validated by using a number of the available experimental data (Langford, 2007; Watts&Grilli, 2003; Sælevik et al, 2009; Fritz et al, 2009; Horrillo et al, 2013; Mohammed&Frits, 2010; Mohammed, 2010; Chen & Przekwas, 2010; Grilli et al, 2003; Watts, et al., 2001). Here we describe some tests for verification of numerical model.

3.1. Aerial landslide simulation

Figure 2 shows a schematic configuration of experimental tank with a pneumatic installation to generate a tsunami by deformed granular landslides (Fritz et al, 2009; Mohammed & Frits, 2010; Mohammed, 2010).

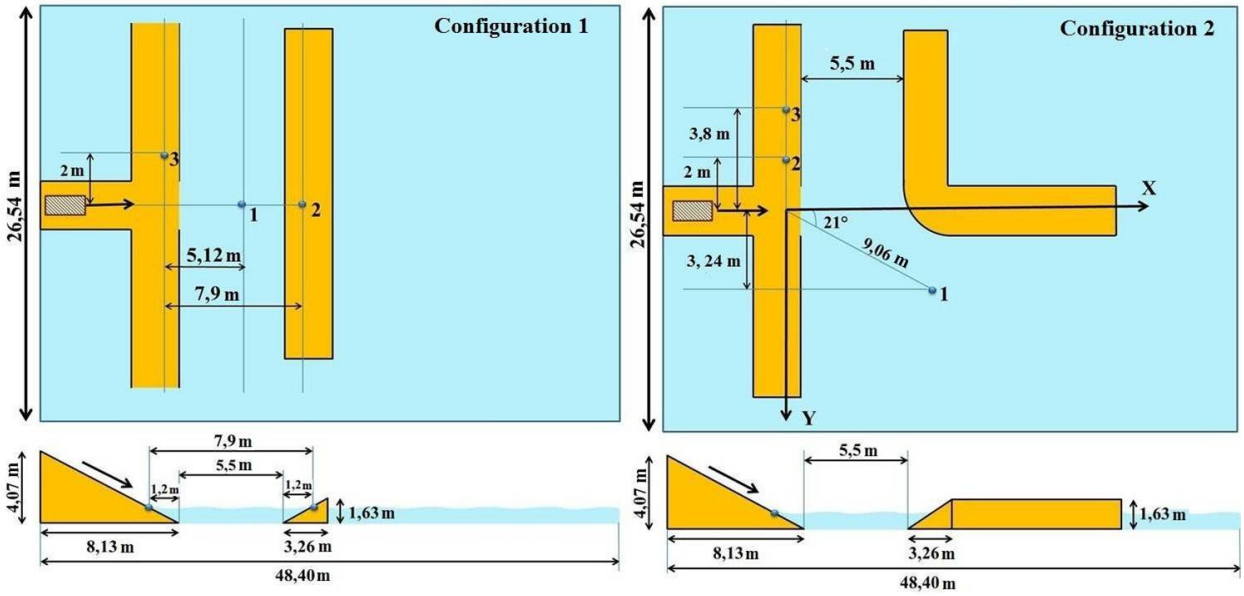

Fig. 2. A tank configuration to study a landslide-type tsunami

(landslide location, tide-gauge location)

The landslide starts its motion along the inclined plane with a predetermined initial velocity of 3.8 m/s. During the experiment the input landslide speed into the water is measured as well as the water displacememnt in some tide-gauge points located in both the "open" water (tide-gauge 1) and in the vicinity of artificial barriers to measure the runup (tide-gauges 2, 3). Tide-gauge 1 in "configuration 1" is located directly in the wave propagation path, and in "configuration 2" it is aimed at measuring the envelope of the barrier wave.

The computational grid consisting of 10 million cells is used for the simulation (Fig. 3). In the area of the landslide and wave propagation the grid has a concentration to describe the motion of the landslide and flow characteristics more accurately.

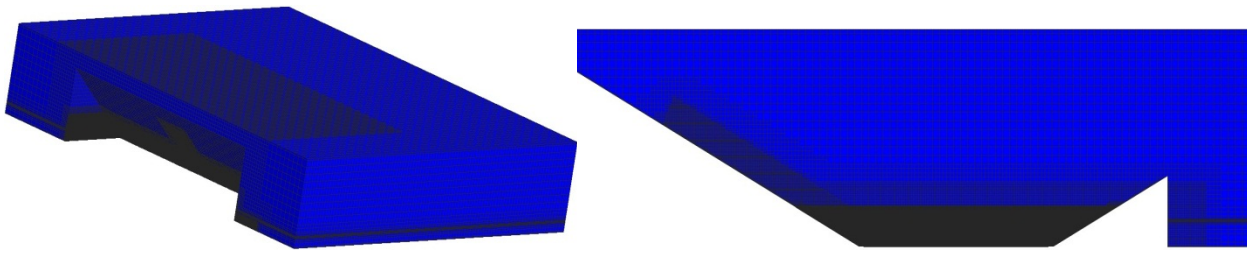

Fig. 3. Grid area (left - a general view, right – the cross section)

The parameters of all three phases: water, air and landslide - are chosen in accordance with the experiment (Table 1). The water depth is 0.6 m. The landslide dimensions constitute 2.1 m × 1.2 m × 0.3 m with its rear edge at a distance of 2.8 m from the top of the inclined plane.

Table 1

Phase characteristics

Phase	Molecular viscosity (kg/m/s))	Density (kg/m^3)
Water	0,001	1000
Air	1,85e-05	1,205
Landslide	26	2600

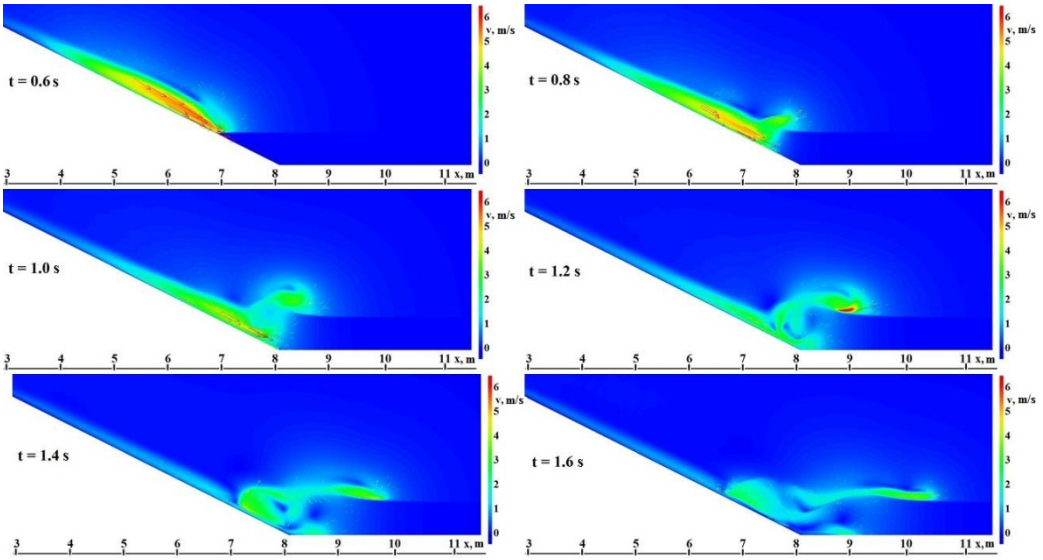

Fig. 4. The fluid velocity field at different times

The simulation is carried out with automatic selection of the time step in accordance with the given Courant number equal to unity. The pattern of the landslide entry into the water and its spread to the barriers is the same for both configurations. So, the following result presentation refers to configuration 1. Fig. 4 shows the velocity field at different points in time of the landslide entering the water. The figure shows that at the time of entry into the water (t = 0.6 s), the landslide has a speed of about 5.5 m/s, which is in good agreement with the experiment. The maximum medium speed is observed for the water phase at the wave breaking point (t = 1.2 s) and is greater than 6 m/s.

The velocity distribution pattern also allows us to see air disturbances which are very low (about 1 m/s) as compared with the other phases, which legalizes that air compressibility ca be neglected. At the overturn moment the wave has the amplitude of about 50 cm that corresponds to the water displacement in the basin (Fig. 5).

After the first wave overturn, the landslide still continues moving along the bottom. After the main mass sliding at the time of 2 sec the second wave with the amplitude 2 times smaller than the first is formed. At the time of 4 sec the landslide is completely in the water, and two waves move on its surface one after the other. At time point of 6 sec a wave runup on the artificial "fiords" is observed. Their amplitude is about the same and is about 10 cm (Fig. 6). The wave runup is also observed on the "fiords" from which the landslide occurred, and its magnitude is about the same.

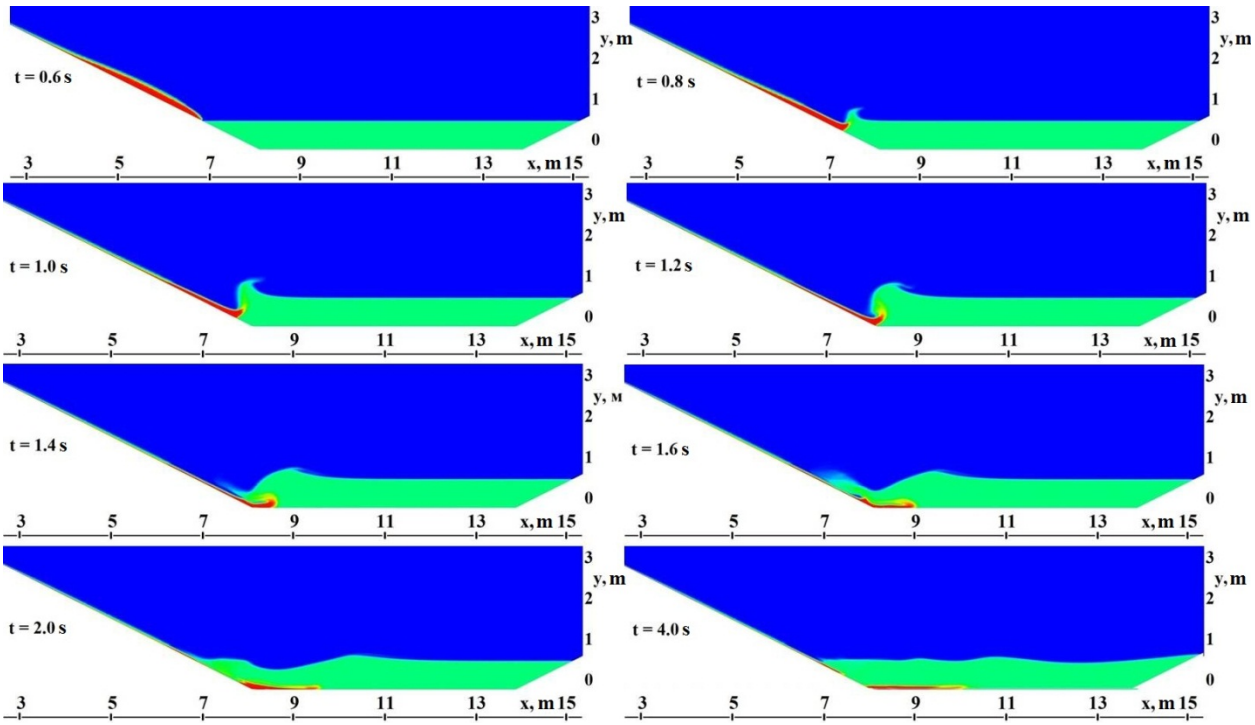

Fig. 5. Snapshots of water displacement in the basin at different times

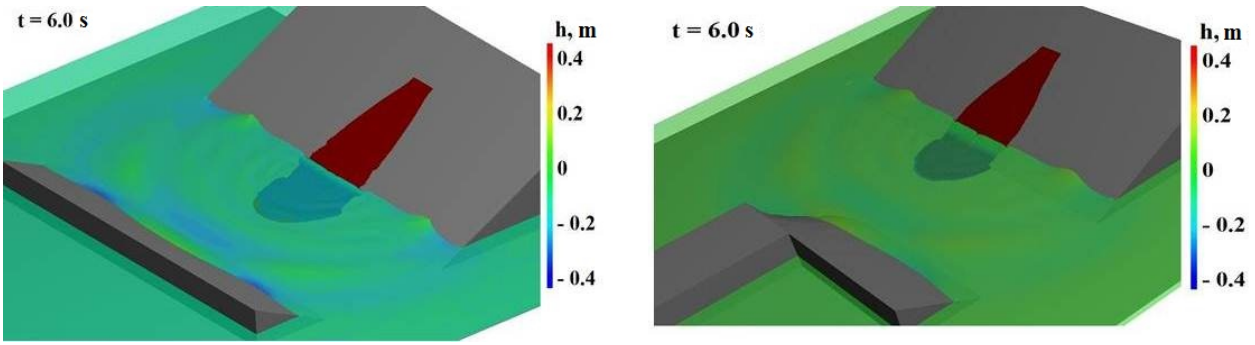

Fig. 6. Wave pattern (left – configuration 1, right – configuration 2)

The computed quantitative characteristics of a wave pattern in the tank can be estimated by tide-gauge data (Figs 7 and 8). As can be seen from the figures, numerical calculation reproduces the tide-gauge records of all the incoming waves, and their amplitude is almost identical with that obtained in the experiment. This applies to both the first wave and the last waves. The only significant difference in the numerical experiment is obtained for tide-gauge 1 in configuration 1 for the "averaged" incoming waves. In the numerical calculation, the re-reflection wave processes strengthened its amplitude even more than it was observed in the experiment. In the experiment there is also a certain gain, although much weaker. For fiord 2 all tide-gauges also gave a good agreement on the wave pattern. The slight difference in wave heights is observed for the third tide gauge.

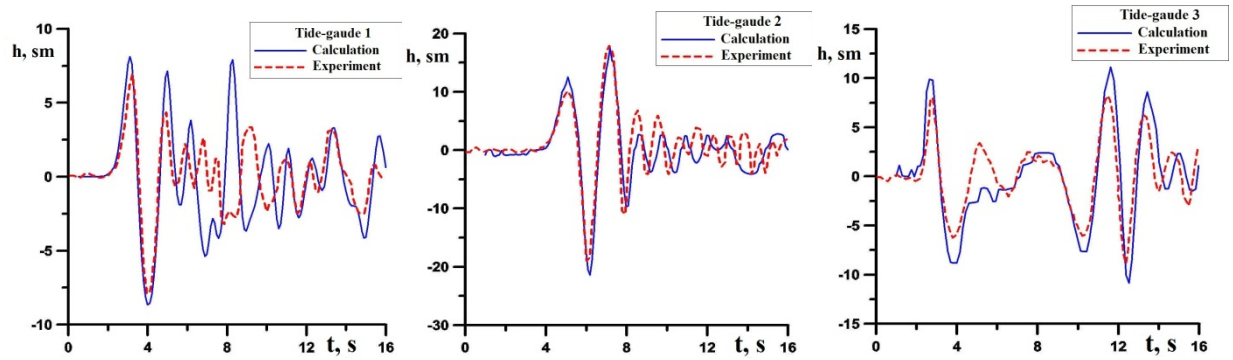

Fig. 7. Tide-gauge records for configuration 1

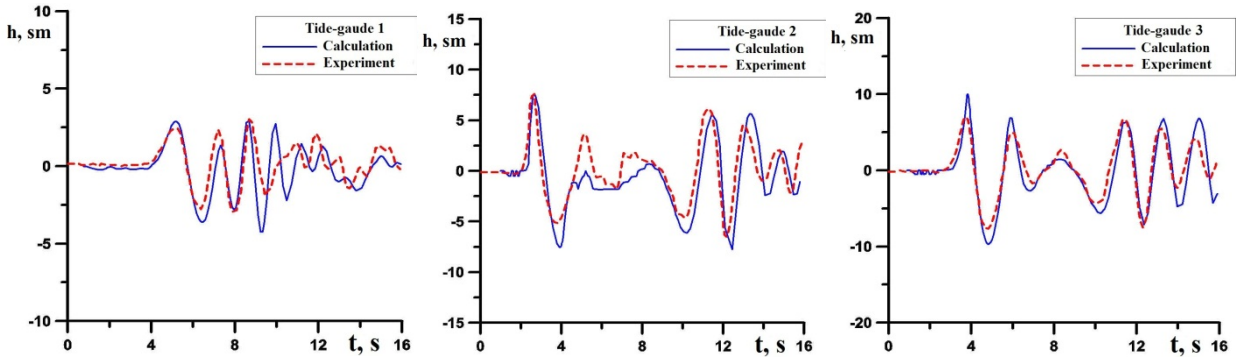

Fig. 8. Tide-gauge records for configuration 2

3.2. Underwater landslide simulation

Here we use the results of (Langford, 2007; Grilli et al, 2003; Watts, et al., 2001) which describe a series of experiments on partially submerged landslides. Schematically, the tank configuration is shown in Fig. 9.

The landslide starts free sliding down on an inclined plane at an angle of 15^0. During the experiment the surface displacement is measured at several tide-gauge points located on a water surface at a certain distance from the shore.

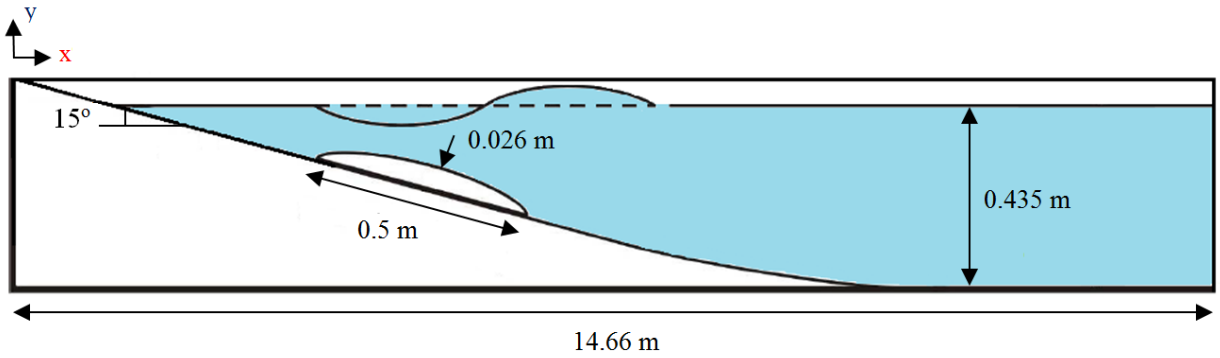

Fig. 9. Tank configuration to study underwater landslide

The experimental configuration SG3_IS5 is chosen for the study, according to which the landslide density is 2830 kg/m^3, the water and air parameters are set in accordance with the values of Table 1. For the modeling the same type computational grid is used as for the surface landslide (Fig. 3), consisting of ~ 100,000 cells. In the area of the landslide movement and wave propagation the grid has a thickening to describe the landslide motion and flow characteristics more accurately. The water depth is 0.435 m, the tank length is 14.66 m. The inclined plane along which the landslide moves is set by the equation

$$f(x)=\begin{cases} -x\cdot\tan(15^0),\ 0\le x\le 1.297\ \text{m},\\ 0.19\cdot(x-1.297)^3+0.1024\cdot(x-1.297)^2-0.2728\cdot(x-1.297)-0.3475,\ 1.297\ \text{m}\le x\le 1.807\ \text{m},\\ -0.435,\ \ 1.807\ \text{m}\le x\le 14.66\ \text{m}. \end{cases}$$

In this case the landslide dimensions are 0.5 m × 0.026 m × 0.25 m. The initial landslide position is also set according to the selected configuration (half-emerged state), with its mass located at a distance of 0.19 m from the coast and at a depth of 0.1 m below the water level (Fig. 10).

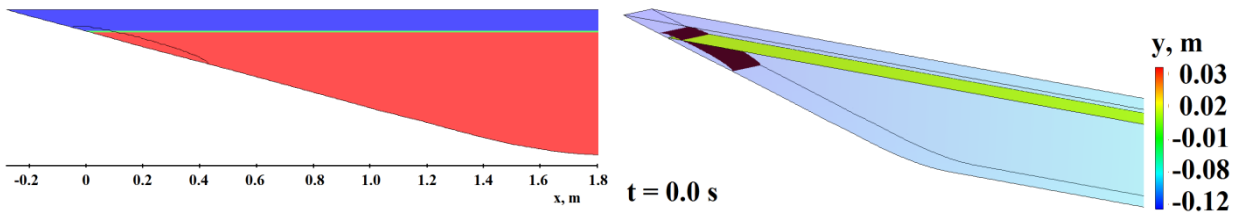

Fig. 10. Landslide location at the initial time

The simulation is carried out with time step automatic selection with the given Courant number equal to 0.5. The pattern of the landslide into the water, its moving along the inclined plane and wave propagation is observed in the time interval of 7 sec. After the first wave overturn the landslide continues moving along the inclined bottom (Fig. 11).

After the main mass sliding at one time moment of 1.6 sec the second wave is formed with the amplitude smaller than the first. At the point of time of 2.6 sec the landslide is completely in the water and successive waves move on its surface.

The quantitative characteristics of the waves can be found from the tide-gauge data (Fig. 12). Here tide gauge 1 is located at a distance of 1.5 m, tide gauge 2 - at a distance of 2.5 m, tide gauge 3 - at a distance of 3.5 m, and tide gauge 4 - at a distance of 4.5 m (all distances from the left boundary). Computed and observed wave amplitudes are almost the same. This applies to both the first and the last waves. Only strengthening (weakening) of the second wave is observed. The most significant difference in the numerical experiment is obtained for tide-gauge 1 for the "first" negative and the "second" positive incoming waves. In the numerical calculation re-reflection processes more strengthened/weakened the wave than is observed in the experiment. The experiment also has a certain gain, although much weaker. On the whole, the simulation results well correlate with the experimental data.

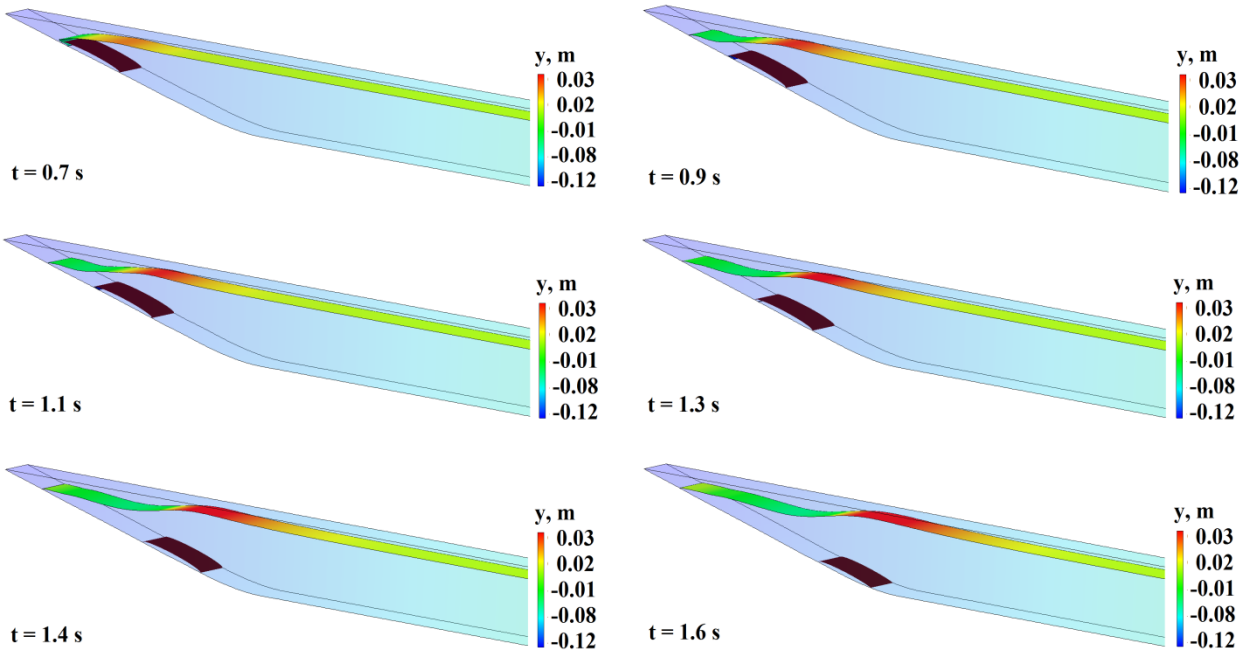

Fig. 11. Snapshots of landslide motion and wave propagation

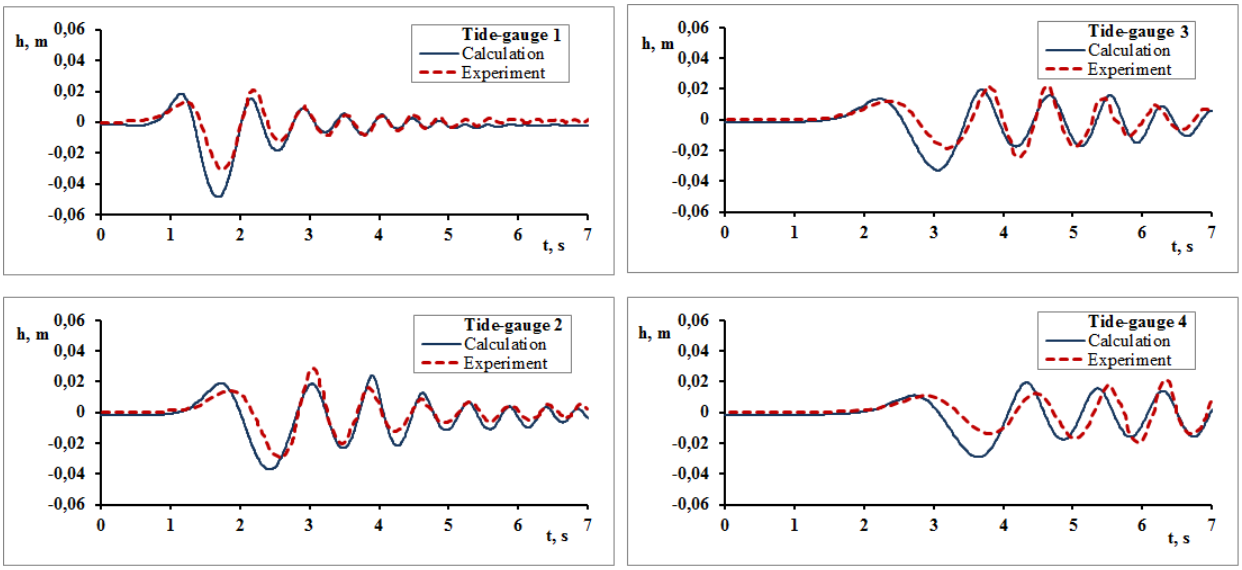

Fig. 12. Tide-gauge records

4. GRID PATTERN CONSTRUCTION TECHNOLOGY

Building a grid model for the numerical solution of the Navier-Stokes equations is one of the key and most difficult stages of the entire modeling process. The experience of solving various classes of problems shows (Kozelkov et al, 2016; Betelin et al., 2014) that the grid model construction can take more than 70% of the time beginning with the task up to obtaining the final result. The quality of the constructed grid directly depends on the accuracy of the solution. The most universal type of grid models are unstructured grids consisting of arbitrary shape polyhedra. The level of development of unstructured grid automatic generators allows building a grid model of the required quality in the field of arbitrarily complex geometric configuration in a relatively short time. Automatic generation means choosing the average grid cell size for the entire computational domain, which ultimately results in a major drawback of this method – the size of the final grid model can reach enormous sizes (hundreds of millions and even billions of counting cells). Therefore, the use of this generator type involves the introduction of sub-areas of the grid model with its own size and then their aggregation. In addition, this grid type imposes restrictions on the used numerical schemes. Then the order of approximation schemes, as a rule, does not exceed the second order unless special methods to increase accuracy are used (Volkov et al., 2014). In addition, the classical scheme of the second order of the central-difference type on such grids are completely unstable, and to make calculations on their basis it is necessary to build a hybrid scheme adding a share of counter-flow (Jasak, 1996; Ferziger & Peric, 2001; Kozelkov et al, 2016; Kozelkov & Kurulin, 2015). Despite all the difficulties, these grids are essential for most industrial-oriented tasks, and at present they are an integral part of the technological chain of the process of mathematical modeling.

Another way to build a grid model is the use of block-structured grids. When constructing them, it is possible to control the size of the cells and their growth rate in a given direction, and, therefore, to control their quantity. The advantage of this method is the ability to use high-order accuracy schemes due to pre-known grid model structure. A significant disadvantage of this method is that the construction of acceptable quality grid patterns in the areas of complex geometric configuration may require the introduction of a substantial number of units and their further conjugation. It results in back-breaking manual labor that can last for months. If a total pattern can allocate large blocks which enable building a block- structured grid, it is advantageous to do so. The current practice of hydrodynamic calculations often uses a combination of block- structured and automated approaches.

When the Navier- Stokes equations are used in tsunami problems, it is expedient to resort to the combination of the two presented approaches. This is primarily due to the different scales of the considered tsunami stages as well as wave characteristics. It should be stressed that this applies to all types of tsunamis, modeled by using the Navier-Stokes equations: seismic, cosmogenic and landslide origin. For the seismic-origin tsunami the different scales of the source and propagation area are not as critical as, for example, for cosmogenic and landslide origin, as the size of the seismic source can amount to tens of kilometers. In this case, the cell size in the area of the tsunami generation and propagation is comparable. For cosmogenic and landslide tsunamis the situation is different. Cosmogenic tsunami generation can be caused by a meteorite of only a few meters large (Kozelkov & Pelinovsky, 2016; Kozelkov et al., 2015), whereas wave propagation is thousands of kilometers. Grid pattern sell dimensions in the area of meteorite movement is times (and, perhaps, dozens of times) different from the cell size in the tsunami propagation area.

This is also characteristic of landslide-origin tsunami, though, perhaps, with less stringent requirements, since the landslide size however large, is unlikely to amount to tens of kilometers. Also, when modeling the landslide motion it is necessary to take into account the force of friction on the "underlying" surface. It involves the selection of the boundary layer for calculating it accurately by analogy with the turbulent boundary layer (Kozelkov et al, 2015, 2016; Kozelkov & Kurulin, 2015).

In addition, to describe tsunami wave propagation in the ocean where the wave amplitude amounts to tens of centimeters, it is necessary to use a grid with about the same cell size. Given, that the ocean depth can be hundreds of meters and grid generation with cell size of tens of centimeters will lead to a grid model of enormous size, it is advisable to apply the mechanism of cell size thickening of the grid model to the interface "air water". All these considerations are the basis of unstructured grid model construction technology for tsunami wave simulation on the basis of the Navier-Stokes equations presented below.

Let us consider landslide-origin tsunami near the island of Montserrat in the Caribbean based on the works of (Pelinovsky et al, 2004; Heinrich et al., 2001). The calculation area highlighting landslide (area 1) and tsunami propagation sub-domains (area 2) is shown in Fig. 13.

The bathymetric map of the area of the Lesser Antilles, Caribbean is downloaded from the website of the International Data Centre for Digital Bathymetry [https://www.ngdc.noaa.gov]. When building a grid model, accounting bathymetric data is carried out by excluding from calculation the cells located below the earth's surface bathymetric line and the ocean floor. To do this, the whole bathymetric model is immersed in a box with the correct dimensions exceeding the size of the model. Then the

extra cells are simply removed. This method of constructing the computational model includes 3 stages:

- the construction of a computational grid with a flat bottom, the depth of which is determined by the maximum depth of the considered water area section according to bathymetric data;
- the calculation of the local water depth for the coordinates of the each calculated cell center by interpolating the data from the next bathymetric points;
- the exclusion from the calculation model the cells, the vertical coordinate of which lies below the bottom.

Fig. 13. Calculation domain of highlighting landslide (area 1) and tsunami propagation (area 2)

This technology is simple to implement, but it leads to a step change in the level of the water area bottom (Fig. 14) which is determined by the characteristic cell dimension near the bottom, and can be reduced by local refinement of the computational grid. Obviously, the smaller the grid near the bottom is, the more accurately it describes the bathymetric line. After the procedure provided, a surface grid describing the bathymetric relief of the earth's surface and the ocean floor is formed on the basis of a set of bathymetric points.

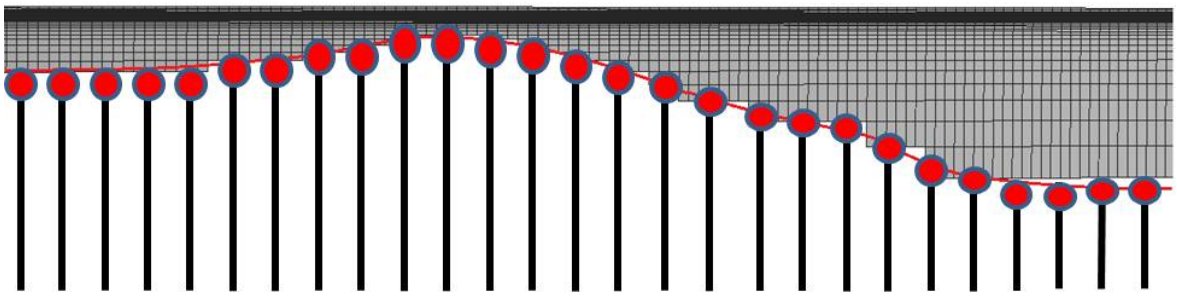

Fig. 14. Computational grid near the bottom, the line is bathymetric line built on the basis of map points (●)

To construct a grid in the landslide area (area 1 in Fig. 13) is used an automatic unstructured grid generator with highlighting the prismatic boundary layer. Using the boundary layer allows to describe the landslide rheology and the frictional force between the landslide and the underlying surface more accurately. It is assumed that at the initial time the landslide has a parallelepiped shape with dimensions 800×2000×25 m in width, length and height, respectively (Fig. 15). This corresponds to the parameters set out in [52, 57] and the volume of pyroclastic flow descended into the sea is 40×10^{6} $м^{3}$

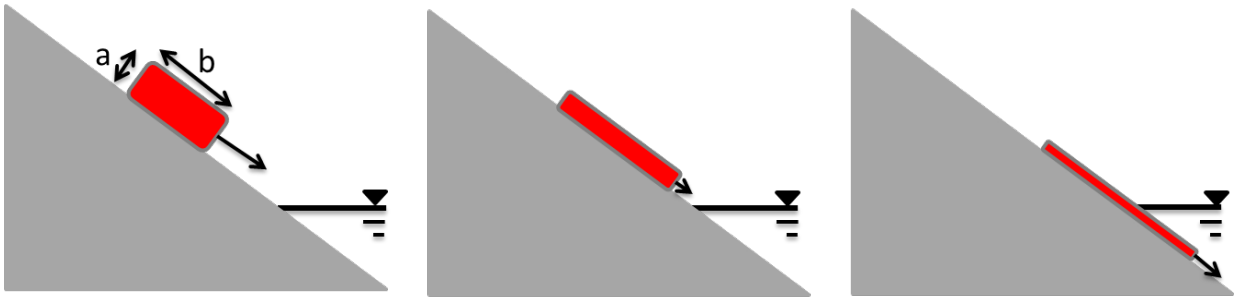

Fig. 15. Landslide motion

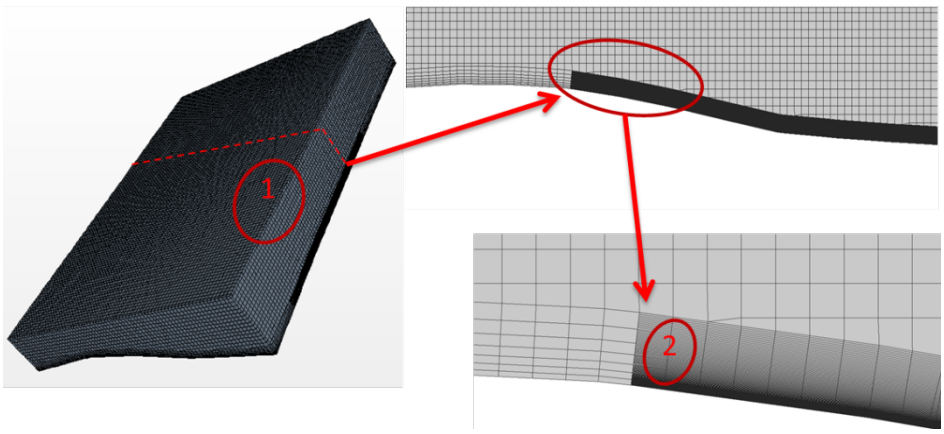

Fig. 16. Grid model for the pyroclastic flow gathering field

In this case, the input data for the grid generator is a surface grid area 1 (Fig.13). The specification of a slope surface in the pyroclastic formation area is achieved by using a refinement unit for the boundary layer. The width of the boundary layer is about 30 meters (dimension "a" in Fig.15). This value is slightly higher than the maximum height of the pyroclastic flow at the initial time and allows simulating it the necessary detailing. When needed, this value can be increased or decreased in accordance with the required dimensions of the modeled landslide, i.e. the size of the refinement unit is set out considering the pyroclastic flow initial position and its motion size range. With these parameters, the base cell size is 75 m (Fig. 16, area 1). In the zone of the boundary layer considering the first refinement, the near-wall cell height is 1 m (Fig.16, area 2) with 1.15 growth factor. Fig. 16 (right) shows an enlarged fragment of the section in the zone of the refinement unit. These grid resolution parameters are optimized for the geometry of the problem and can adequately simulate all the features of the pyroclastic flow movement and its entry into the water, thus creating a pulse provoking a tsunami wave. The size of the grid model of the pyroclastic flow gathering (area 1 in Fig.13) contains about 7 million cells.

In the open ocean, where it is necessary to simulate tsunami propagation, it is advisable to build a block-structured grid specifying the interface of "water-air" section. The main purpose of constructing the grid in such a way is thus providing a sufficient size cells near the interface of the "water-air" section in the entire area for simulating both energy-bearing and fading tsunami waves of small amplitude. With the help of the block-structured grid generator is built a regular parallelepiped with dimensions 230 km × 230 km, the depth of 5200 m and 1100 m height (it is determined by the maximum depth and the height of the area under consideration according to the bathymetric data) (Fig.13, area 2). Since the pyroclastic gathering detailing area is not taken into account, from the main block a parallelepiped is cut whose coordinates coincide with the coordinates of the block for area 1 (Fig.13). The methodology of interface separation is as follows. After building the model geometry, a three-dimensional block is divided on its edge into 2 parts. The main coordinate of the rib is aligned with the surface of the "water-air" section ($z = 0$). The linear dimension of the cells adjacent to the top and bottom of "water-air" interface is 0.1 m. This size is specified increasing by the law of geometrical progression with the growth rate from the surface to the bottom and to the top interface of the air by a factor of 1.15. This allows to get rid of too "small" cells in the areas that do not require simulation. The thickening of the "water-air" section interface is shown in Fig. 17 left. In addition, the area is divided into blocks of additional cell refinement near the dock to provide a smooth transition from the small cell size in the detailing area to a bigger size in the area of the free wave propagation (Fig.17, right).

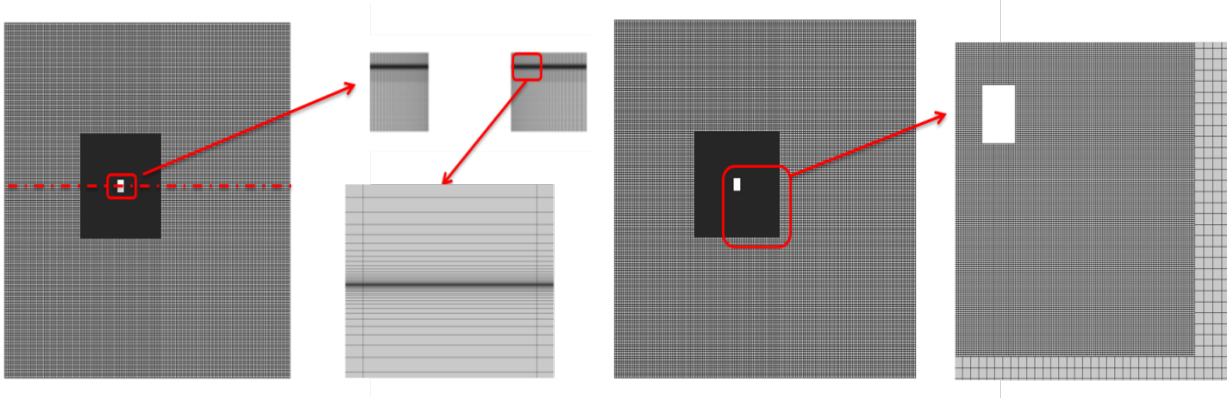

Fig. 17. Computational grid block with interface “water – air” condensation (left) and a transition area between the grid blocks (right)

Next, according to the algorithm described above, the accounting of bathymetric data is carried out by excluding the cells, located below the earth’s surface bathymetric line and the ocean floor, from the computational domain. Thus constructed the grid model for area 2 contains approximately 13 million cells, i.e., the general model consisting of these two areas will contain about 20 million cells. To construct the final grid model the grids, obtained in the previous two stages, are to be linked. To do this, both grid models are loaded in the LOGOS pre-post-processor package. Further, both grids are united into one using the node connection procedure (Fig. 18). Figure 18 below shows an enlarged fragment of the section in the joining zone of the two grid models.

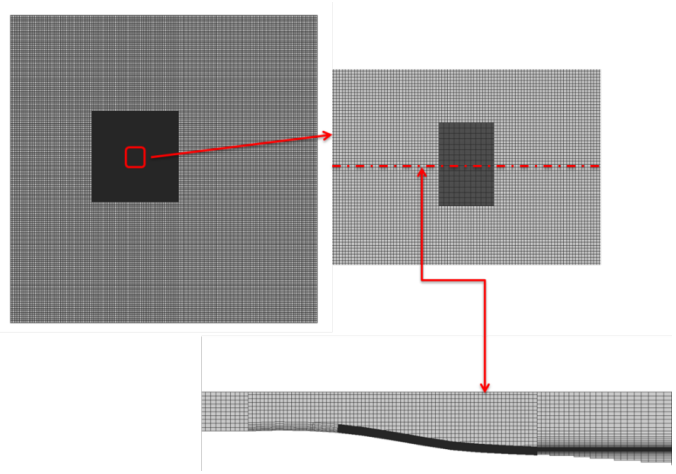

Fig. 18.The final grid model for the computational domain

Thus, the presented technology of this class grid building provides an adequate quality grid model, which consists mostly of regular hexahedral cells with adequate resolution for numerical simulation of both the pyroclastic flow gathering area and the propagation of waves of varying amplitude. It should be noted here that this technology allows constructing grid models for a more accurate calculation of tsunami runup. To do this a coast zone must be selected and a grid constructed by an automatic

generator in the same way as for area 1 in Fig. 13. The selection of the boundary layer in the runup area allows not only setting the desired properties of the underlying surface (roughness accounting with special boundary conditions), but also simulating the turbulent wave transformation in the collapse by the method of wall functions.

5. TECHNOLOGY TO ACCELERATE THE COMPUTATIONS

In many practical problems the discretization of the Navier-Stokes equations yields a system of difference equations with ill-conditioned matrix, the condition number of which is often 10^7-10^8, but for some cases it may be close to 10^{10} (Kozelkov et al., 2013, 2016). As a result, that the matrix SLAE decision is the most costly step. When using classical iterative methods it takes about 90% of the calculated step computing time. These classical iterative methods either do not work or give a very slow rate of convergence. One way to accelerate convergence and improve the stability of the iterative process is a multigrid method (Tai & Zhao, 2003; Volkov et al, 2013; Kozelkov et al., 2013, 2016), based on the use of a sequence of nested grids and transition operators from one grid to another. Here the algebraic and geometric approaches are distinguished. In the algebraic approach the discrete equation of the sequence of nested grids are formed without constructing nested grids on the matrix level, whereas in the geometric approach – the hierarchy of networks created by merging the control volumes of the upper level of the grid (the detailed one). It is easy to build grid levels using original matrices generated by implicit discretization of the Navier-Stokes equations. It leads to the simplicity of building operators of restriction and continuation thus making the algebraic approach very attractive from a computational point of view. The geometric method requires additional algorithms of rebuilding the computational grid which can be justified for certain classes of problems. Advantages and disadvantages of both approaches are discussed in (Volkov et al., 2013).

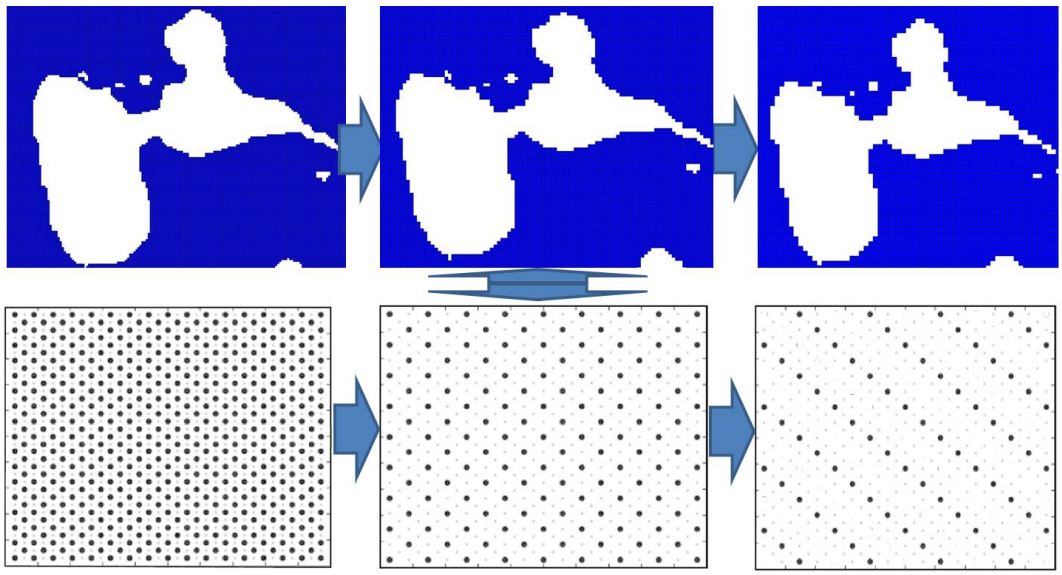

Fig. 19. The sequence of nested grids in the matrix (below) and grid levels (top)
(the top of the figure shows Guadeloupe, Lesser Antilles, Caribbean)

The construction of an algebraic multigrid method for geophysical problems involves automatic coarsening of the original grid on the matrix level (Fig. 19). The calculation of the equation (12) using a multigrid method is as follows. Equation (12) can be represented in the general form:

$$A_h x^h = b^h, \tag{16}$$

where h is the index of discrete equation belonging to h grid. The interpolation operator P from a coarse grid H on a detailed grid h allows you to represent the operator A_H on the coarse grid in the form of

$$A_H = R\, A_h\, P, \tag{17}$$

where $R = P^T$. The solution correction step is as follows:

$$x^h_{new} = x^h_{old} + Pe^H\,. \tag{18}$$

The solution correction e^H is an exact solution of the equation

$$A_H\, e^H = r^H, \tag{19}$$

where $r^H = R\, r^h$, $r^h = b^h - A_h x^h_{old}$.

Thus, the multigrid method using solution correction scheme represents the following sequence of steps (Fig. 20, left):

1. μ_1 solution approximations on the grid h by using the Zeidel method (pre-smoothing) are done.

2. The residual $r^h = b^h - A_h x^h_{old} \in V_h$ is projected onto the space V_H, т.е. $r^H = Rr^h$.

3. The approximate solution $A_H\, e^H = r^H$ on the coarse grid is found. γ multigrid cycles are done recursively for this.

4. The correction e^H is interpolated on a detailed grid and decision correction is made on the detailed grid $x^h_{new} = x^h_{old} + Pe^H$.

5. μ_2 decision approximations are done on the detailed grid to suppress interpolation errors (final smoothing)

Depending on the number of recursive method calls γ on each grid level emit different types of cycles are singled out. When $\gamma = 1$ there is a V-cycle, if $\gamma = 2$ – there is a W-cycle (Fig. 20, right). If at each level is recursively called one a W-cycle, and then the a V-cycle , we obtain an F- cycle (Kozelkov et al., 2015).

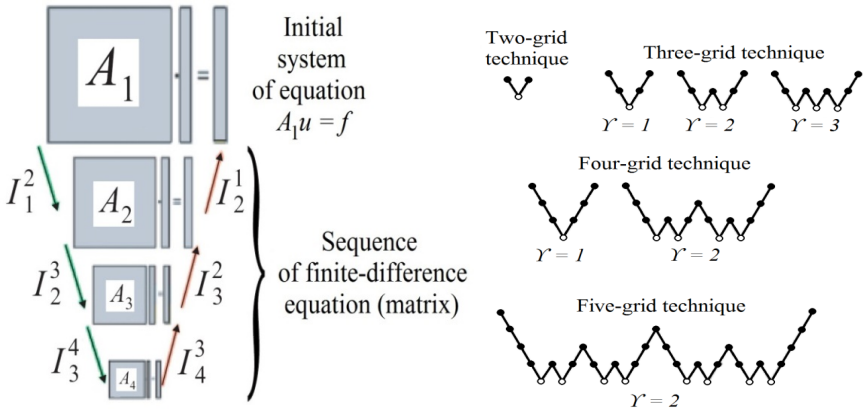

Fig. 20. Matrix sequence (left) and the V- and W- cycles (right)

In the aggregation method of coarsening with constant interpolation all variables divided into I_k units containing all the indices i, which correspond to the cells included in the unit k. The operator construction on the coarse grid is produced by the relation:

$$A_H = RA_hP = \left(a_{kl}^H\right), \quad a_{kl}^H = \sum_{i \in I_k} \sum_{j \in I_l} a_{ij}^h, \ (k, l \in C). \tag{20}$$

The multigrid method parallelization implies that the matrix coarsening during the transition from one level to another occurs independently on each MPI-process (Kozelkov et al., 2016a,b). The coarsening process in parallel mode creates two problems. Firstly, the coarsening is stopped if in each the process there is one left. Secondly, on a gross level where the matrix dimension is small the time spent on the inter-processor communication, due to communication environment latency, begins to repeatedly exceed computed time. To solve these problems (Kozelkov et al., 2016) suggests performing the collection of small matrices in one process, forming one global level and continuing coarsening and solution in sequential mode (Fig. 21, left).

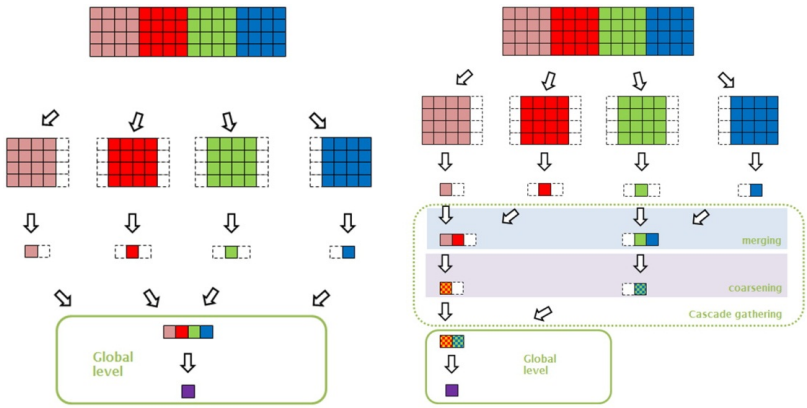

Fig. 21. Global level formation (left) and its cascading collection (right)

Using a global level can complete the coarsening process in a parallel case, and also, can avoid the overhead expenses resulting from inter-processor communication in the coarse grid level processing because of the global level storage on one process. The analysis of the proposed algorithm effectiveness, held in (Kozelkov et al., 2016), showed that the average time of computations increasing as compared with the classical iterative methods is 4-6 times. A major shortcoming of the global level is that it is performed in a sequential mode. When determining the amount of the problem, the memory of the unit on which the main processor is located may not be enough to build a global level. This aspect will also affect the limitation of the algorithm when using large-scale grids of hundreds of millions of cells (such grids are typical of geophysical problems). The way out here is the use of cascading level algorithm to gradually reduce the number of processes involved in the analysis while maintaining the advantages of the global level. The cascading level algorithm is also presented in (Kozelkov et al., 2016). It includes the stage of breaking the whole initial set of residual matrix after coarsening in pairs and performing their twinning. In the second stage the operation is repeated until the total coarse level matrix is obtained (Fig. 21, right). The level consolidation level in itself, in addition to generating information on a new level, contains a procedure of re-definition information about inter-processor exchanges, which also requires spending some of the CPU time. In addition, the parallel procedure of cascade level coarsening requires the introduction of additional inter-processor communication, which are absent in the case of scalar implementation at the global level collection.

The main advantage of the cascade summation scheme is the algorithm scalability. It actually removes restriction on the maximum size of the problem to be solved because of the possible lack of memory unit on which the global level is developed. Furthermore, the global level speed increases since its component parts are formed and coarsened independently.

6. TSUNAMI SIMULATION

6.1. Tsunami from the “model” source

To verify the performance of the presented methodology was simulate the tsunami propagation in the one part of the World Ocean. It is based on the tsunami generated by the slide of the pyroclastic flow into the water resulting from the eruption of the Soufriere Hills Volcano on Montserrat, Caribbean (Pelinovsky et al., 2004). In (Pelinovsky et al., 2004) this tsunami modeled by using two approaches. In the first case the model cone-shaped source was used as initial approximation, and the wave propagation was computed using the code TUNAMI (Goto et al., 1997) (recommended by UNESCO for tsunami research), which is based on shallow-water theory. In the second case the pyroclastic flow was generated by the model described in (Watts & Waythomas, 2003) and the propagation was computed by the code FUNWAVE (Kirby et al., 1998) based on the nonlinear-dispersive theory. Later, after adding the block to calculate different initial perturbations this code got the name

GEOWAVE. In (Pelinovsky et al., 2004) is shown quite a significant difference in the results obtained using these approaches both in predicting wave heights and wave pattern as a whole. It is also noted there that non-linear dispersion theory is more preferable to use. Taking into account that hydrodynamic cone-shaped source (Fig. 22,a) was used in (Pelinovsky et al., 2004) for both calculations as an initial tsunami approach, here, to compare tsunami propagation adequately, was taken a source generated by the model described in (Watts & Waythomas, 2003). The source produced by this model is also cone-shaped (Fig. 22,b). Its geometric parameters correspond to the descended pyroclastic flow. The amplitude of the initial wave in the tsunami source is 1.26 m. The distance between the nodes of the computational grid has a resolution of 500 m. Fig. 23 shows the comparison of wave patterns produced by different approaches (here is the comparison only with the GEOWAWE code (the wave pattern with use the TUNAMI program is similar). As you can see, qualitatively, the pictures are practically identical.

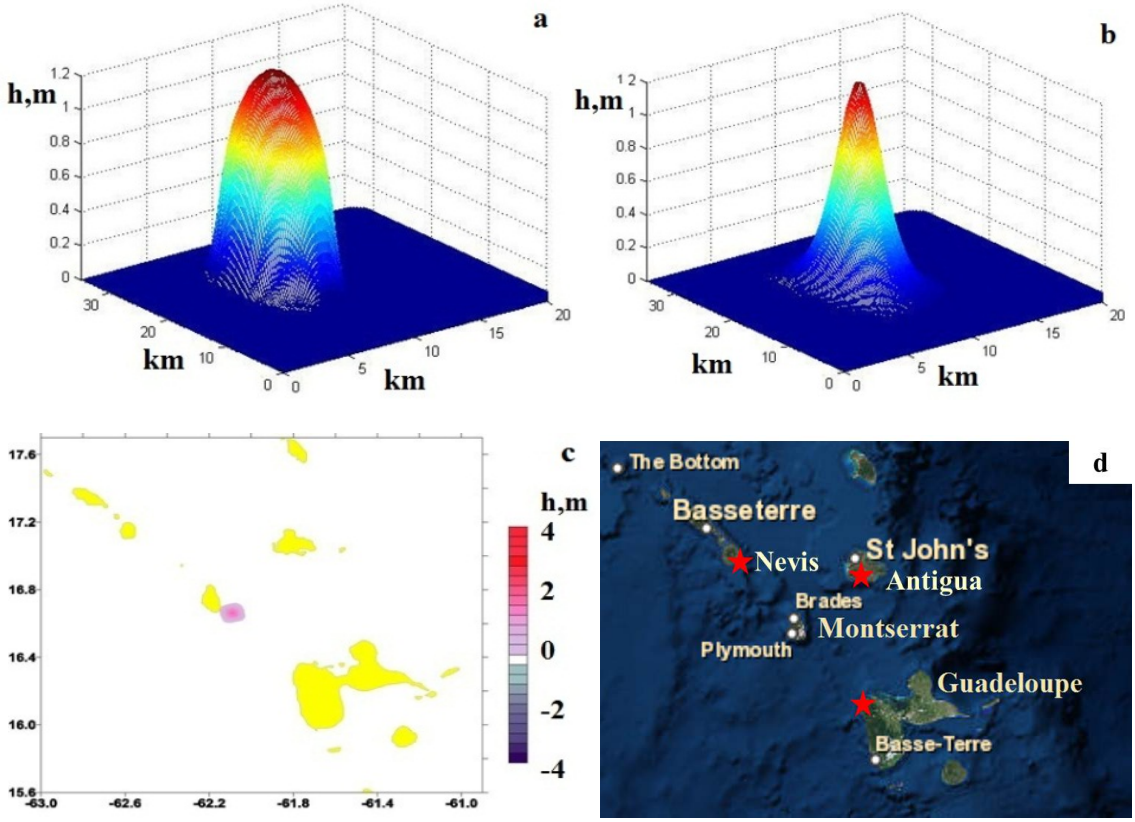

Fig. 22. Tsunami source: *a* – hydrodynamic source; *b* – source gained by code GEOWAVE; *c* – computation domain; *d* – the location of gauges

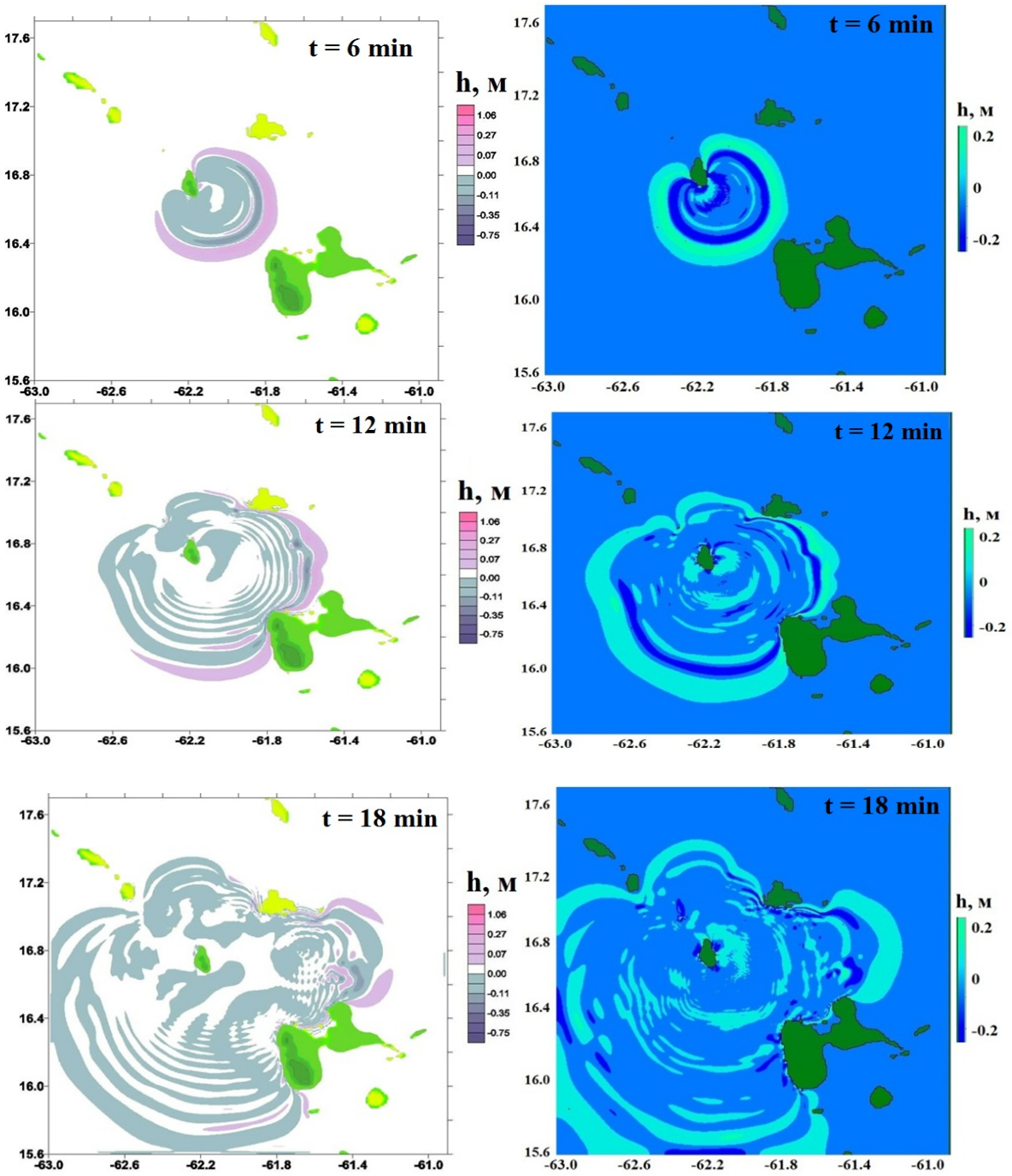

Fig. 23. Snapshots of tsunami propagation: GEOWAVE (left) and LOGOS (right)

Quantitative comparison of tide-gauge records shown in Fig. 24 can also be considered very satisfactory. The leading waves that came in the north-western part of the island of Guadeloupe and

the island of Antigua are almost identical. The first three waves are predicted by both calculations, though they have slightly different heights. Subsequent waves are described differently, and the Navier-Stokes equations give a more pronounced oscillatory character, while the waves calculated by nonlinear-dispersive shallow-water theory fade quicker. These differences may be related to many factors and require further study. These factors include primarily the models themselves - they are different and are solved by various numerical approaches - finite differences and finite volumes. The secondary factors include grid model resolution and numeric approximation schemes.

Here should be noted the temporal characteristics of the calculations. The grid model for programs based on the shallow water and nonlinear dispersive equations are always two-dimensional with a fixed height above sea level at each computational point. The total number of points is only about 200 million (the grid is 430×430). With the help of these models on the grid only tsunami propagation is calculated which requires about 3 hours of computer time opposed to 40 minutes of physical time on a single processor. The LOGOS software package carries out the numerical solution of the Navier-Stokes equations exclusively in three-dimensions. In the three-dimensional grid, taking into account topographic features, tsunami propagation requires within 40 minutes of physical time about 15 hours on 96 processors. So, the computation is 5 times longer than two-dimensional and occupies 100 times greater volume of CPU field. The difference can be explained by the models used. The above-mentioned two-dimensional models only describe the wave propagation and do not allow supplementing by source and runup calculation. In this regard, the three-dimensional model based on the Navier-Stokes equations is more versatile - it includes the presence of these stages, and does not limit the physical properties of propagation such as viscosity, dispersion and nonlinearity. Expectedly, in any in any case, the Navier-Stokes equations reproduce the process more accurately, but they require more resources than such simplified models as the shallow water equations.

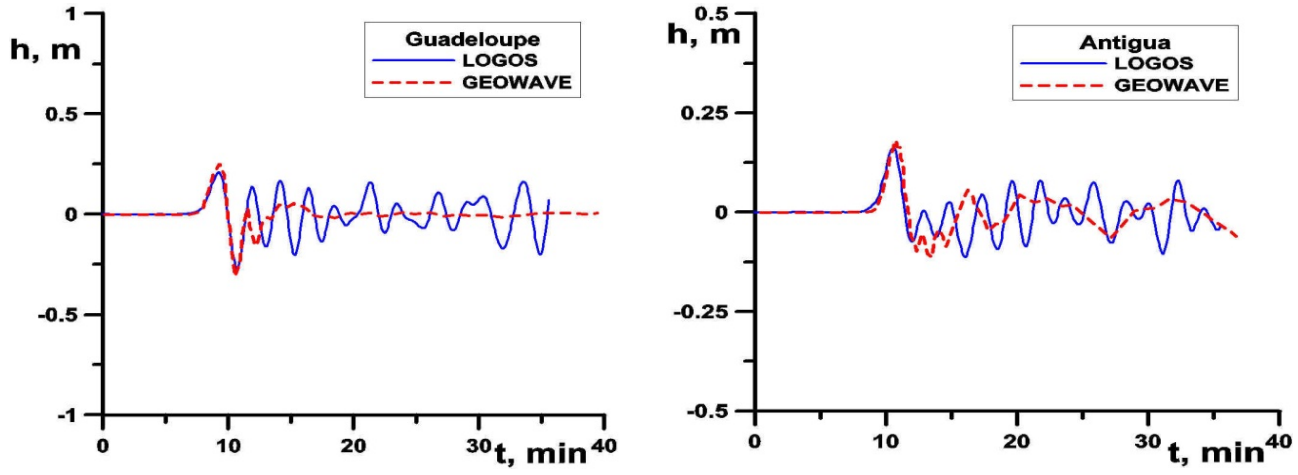

Fig. 24. Comparison of tide-gauge records on Guadeloupe and Antigua

6.2. Tsunami with the simulated slide of the pyroclastic flow

To generate a tsunami directly by pyroclastic flow slide a multi-phase system of the Navier-Stokes equations and the method described in Section 2 will be used. In this problem setting the landslide is modeled as a Newtonian fluid with its physical characteristics. The properties of all system phases correspond to Table 1 (Section 3). The grid model, the technology of its construction and the geometric parameters of the computational area the landslide are described in Section 4. The movement of the pyroclastic stratum is due to gravity, the initial velocity is absent. The input speed of a landslide in the water as well as sea-level in the same gauges is recorded. The simulation is carried out with the automatic selection of the time step in accordance with the given Courant number equal to 1. Figure 25 presents the velocity field at different moments of the landslide entering the water. The figure shows that at the time of entering the water (t = 10 c) the landslide has a speed of about 25-30 m/s. The landslide maximum speed is observed at the moment of it entering the water (t = 30 c) and exceeds 35 m/s. The velocity pattern also allows seeing the disturbance of the air, which are negligible in comparison with the other phases. This fact proves air compressibility neglect justified.

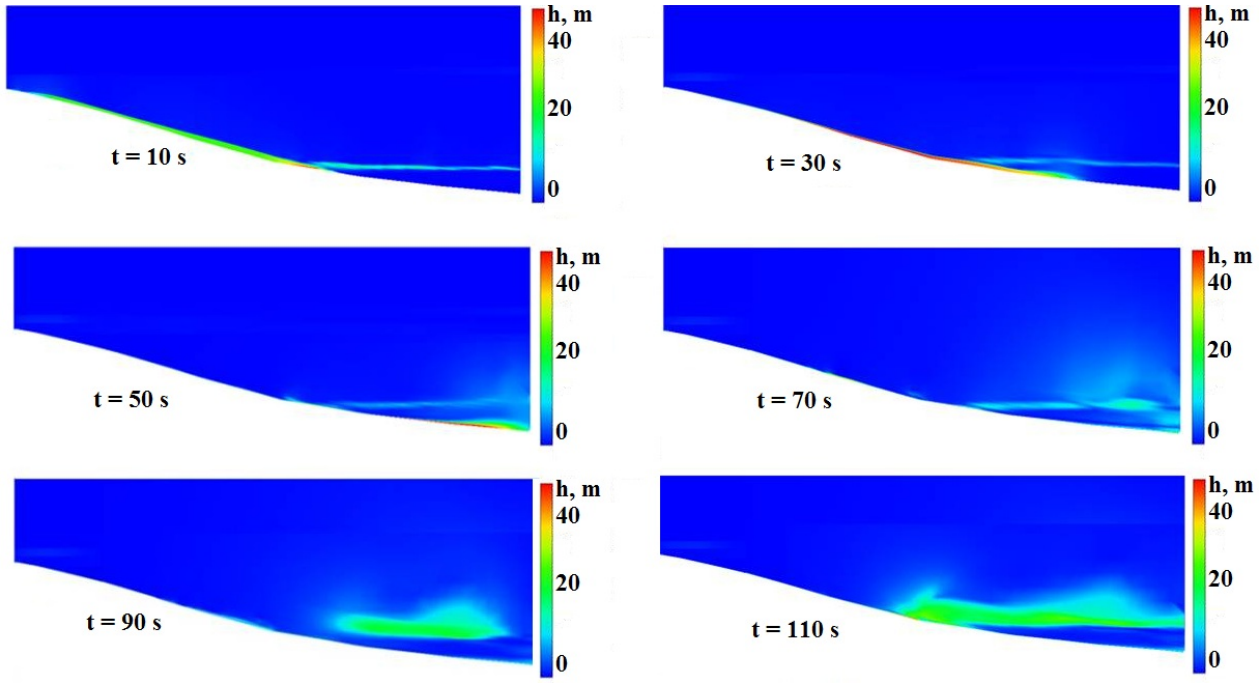

Fig. 25. Snapshots of velocity of the multiphase system at the landslide entering the water (on the axes are marked meters)

Figure 26 demonstrates 3D view of wave pattern in the entrance area of the landslide. As you can see, the model based on the Navier-Stokes equations gives a more detailed picture of the landslide motion than the previously discussed models (Fig. 22,a and 22,b), and can essentially give a comprehensive

picture of the landslide tsunami source. Moving along the side of the mountain, the landslide takes the form of its topography precisely fitting all its features. About a minute later the landslide completely enters the water, at the same time a tsunami wave is generated. The wave height at the source is high enough and reaches 20 meters, which is equal to the data (Heinrich et al., 2001).

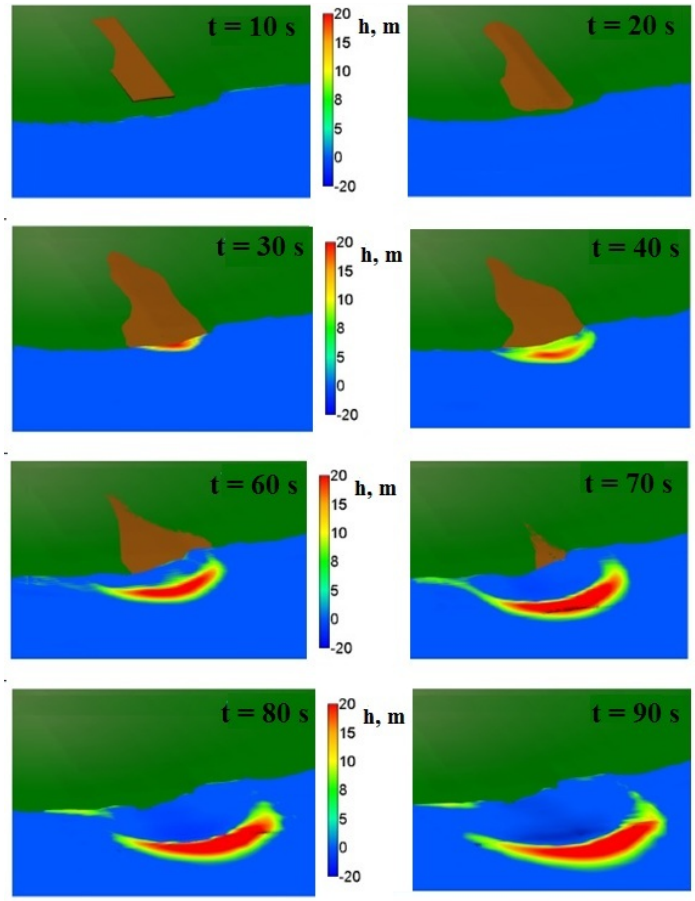

Fig. 26. 3D view of the entrance area

Figure 27 shows a further development of 3D wave perturbations. Here secondary waves departing from major wave at the source can be observed. These are edge waves propagating along the shoreline, and their amplitude is small as compared with the main source of the disturbance. All this points to the capabilities of the model used to describe complex fluid physics. Wave propagation in the Caribbean is shown in Fig. 28. It is next to impossible to define the difference in the wave pattern between the three models used.

It should be recalled that the grid model used in these calculations is built with a detailed landslide area and consists of about twenty million three-dimensional cells. On this grid tsunami propagation for 40 minutes of physical is calculated for about 72 hours on 320 processors when using the implicit integration method of the Navier-Stokes equations. It is 5 times longer than a similar 3D calculation with a model source and 12 times longer than the 2D calculation. It takes 320 times bigger processor

field as compared with the 2D calculation and more than 3 times bigger as compared with the 3D calculation, but with the model source. This increase in the time of the calculation can be accounted for by the detailed entrance area of the landslide. However, the latter made it possible not only to track the movement of the landslide on the slope, but also to identify additional physical aspects of a tsunami generation formed by a pyroclastic flow slide.

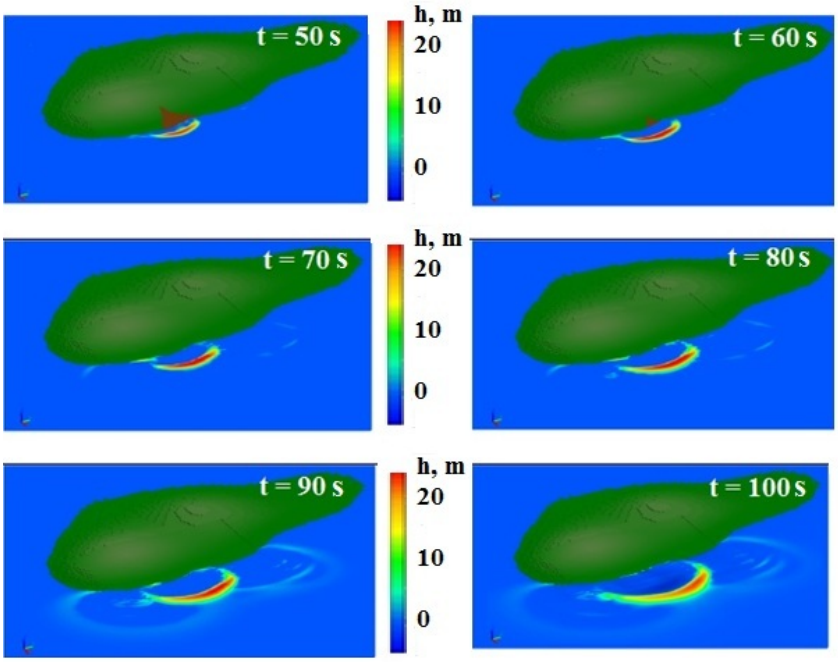

Fig. 27. Snapshots of 3Dl wave pattern with detailed wave disturbances

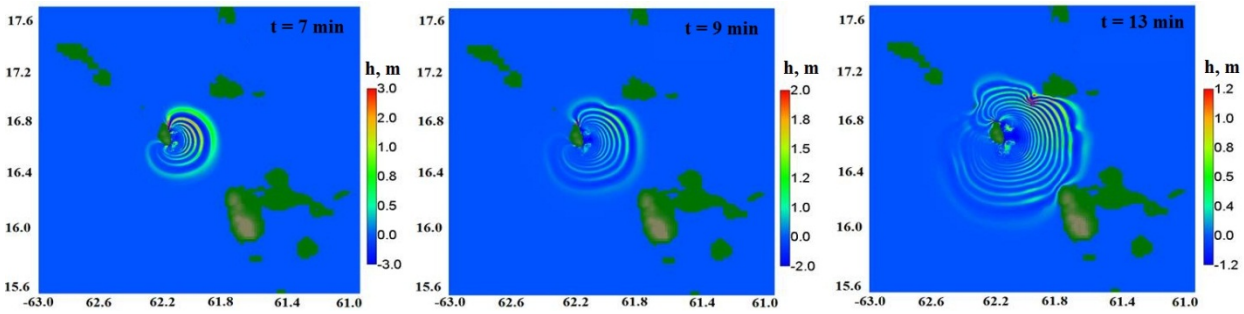

Fig. 28. Snapshots of tsunami propagation

Figure 29 demonstrates the comparison of tide-gauge records in the framework of the Navier-Stokes equations with a pyroclastic flow slide (LOGOS), shallow-water equations (TUNAMI) and nonlinear-dispersive equations (GEOWAVE). The first waves that came on the north-western part of the island Guadeloupe differ greatly. The wave height computed by the LOGOS is twice higher, which better agrees with observations. The gauges «OldRoad» located on the island of Antigua shows a higher

result, which better agrees with reality as the island is in close proximity to Montserrat, and there has to be one of the peaks. The gauges on Nevis Island, located on the opposite side from the eruption site, shows at once a fading wave. The result obtained by LOGOS is closer to the result obtained by the shallow-water equations. Nonlinear-dispersive equations give much greater attenuation (fading). Subsequent waves are described in different ways, and the Navier-Stokes equations give a more pronounced oscillatory character, while the waves, calculated by the nonlinear-dispersion model, also fade faster.

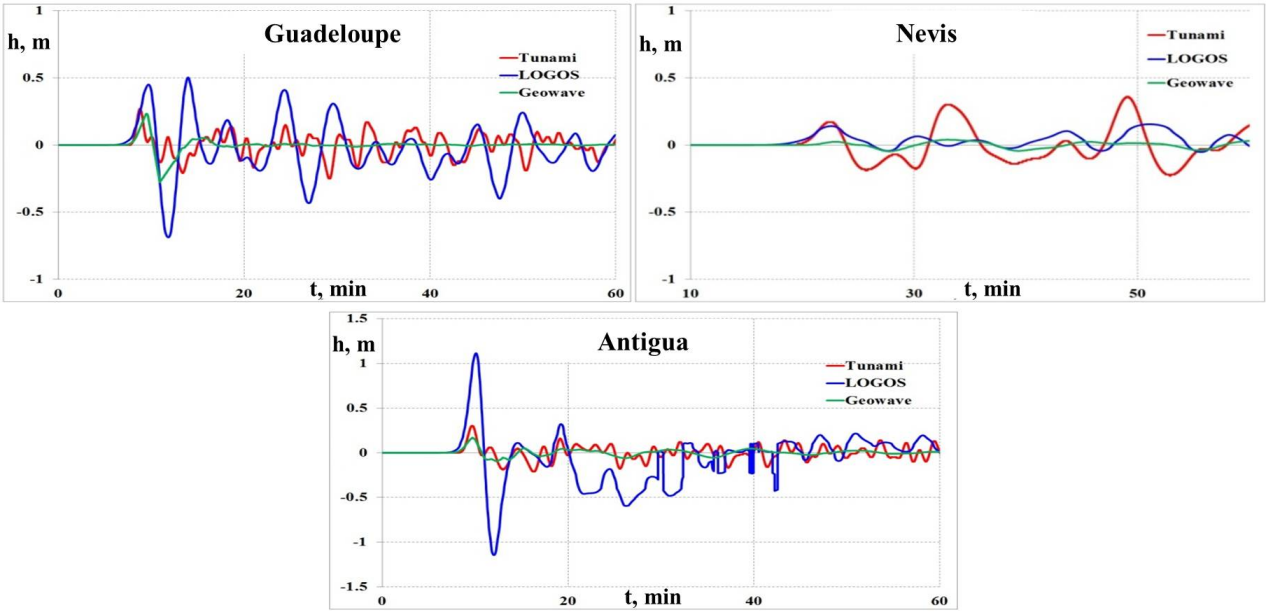

Fig. 29. Comparison of tide-gauge records according to three models

As a result, all the models show that in the north-western part of the island of Guadeloupe a tsunami wave is generated, although the shallow-water and nonlinear-dispersive theories show a more modest result in amplitude. The model based on the Navier-Stokes equations is much closer to the observations (Pelinovsky et al, 2004). It is not difficult to guess and, it really is obvious, that it all depends on the description of the tsunami source. The Navier-Stokes equations reproduce the landslide tsunami source more accurately.

7. CONCLUSION

The paper describes the technology for computations the landslide-origin tsunami based on the Navier-Stokes equations. The landslide source is modeled by a separate phase representing a Newtonian fluid with its own density and viscosity. The methodology of numerical solution of multiphase system is based on a fully implicit method, which removes strict restrictions on the time step, and allows simulating tsunami propagation at arbitrarily large distances. The formulas for

discretization of equation sampling and coefficient types are given. To effectively calculate tsunami propagation in large water areas is presented an algorithm based on an algebraic multigrid method. The results of a full-scale experiment calculation are given. They demonstrate the possibility of using computed technology provided all stages of the landslide-origin tsunami - generation, propagation and runup. The algorithm to account bathymetric data for tsunami simulation in real waters of the World Ocean is described. The technology of building 3D grid models with the detailed area of generation and runup is demonstrated. The results of the comparison with the nonlinear- dispersive theory on the example of the historical tsunami of volcanic origin are presented, which showed a fairly good agreement for identical sources but different results for the parametric source and the actual slide.

ACKNOWLEDGEMENTS

The presented results were obtained with the financial support of the grants of the President of the Russian Federation for state support of leading scientific schools of the Russian Federation (NSH-6637.2016.5) and with the financial support of the RFBR grants 16-01-00267, 15-45-02961.

REFERENCES

1. Beizel, S.A., Chubarov, L.B. and Khakimzyanov, G.S. Simulation of surface waves generated by an underwater landslide moving over an uneven slope // Russ. J. Numer. Anal. Math. Modelling, 2011, vol. 26, no. 1, 17-38.

2. Betelin, V.B., Shagaliev, R.M., Aksenov, S.V., Belyakov, I.M., Deryuguin, Yu.N., Kozelkov, A.S., Korchazhkin, D.A., Nikitin, V.F., Sarazov, A.V. and Zelenskiy, D.K. Mathematical simulation of hydrogen–oxygen combustion in rocket engines using LOGOS code // Acta Astronautica 2014, vol. 96, 53-64.

3. Cecioni, C. and Bellotti, G. Modeling tsunamis generated by submerged landslides using depth integrated equations // Applied Ocean Research, 2010, vol. 32, 343-350.

4. Chen, Z.J. and Przekwas, A.J. A coupled pressure-based computational method for incompressible/compressible flows // J Computational Physics, 2010, vol. 229, 9150-9165.

5. Chin Hoe Tai and Zhao Yong. Parallel unsteady incompressible viscous flow computations using an unstructured multigrid method // J Computational Physics, 2003, vol. 192, 277-311.

6. Didenkulova, I., Nikolkina, I., Pelinovsky, E. and Zahibo, N. Tsunami waves generated by submarine landslides of variable volume: analytical solutions for a basin of variable depth // Natural Hazards and Earth System Sciences, 2010, vol. 10, 2407-2419.

7. Didenkulova, I.I., Nikolkina, I.F. and Pelinovsky, E.N. Resonant amplification of tsunami waves from an underwater landslide // Doklady Earth Sciences, 2011, vol. 436, no. 1, 66-69.

8. Dutykh, D. and Dias, F. Energy of tsunami waves generated by bottom motion // Proc. R. Soc. A, 2009, vol. 465, 725-744.

9. Fedotova, Z.I., Chubarov, L.B. and Shokin, Y.I. Simulation of surface waves caused by landslides // Vycisl. tehnologii – Computational Technologies, 2004, vol. 9, no. 6, 89-96 [In Russian].

10. Ferziger, J.H. and Peric, M. Computational methods fluid dynamics. 3rd edition. – Berlin; Heidelberg; New York; Barcelona; Hong Kong; London; Milan; Paris; Tokyo: Springer, 2002. 423 p.

11. Fine, I.V., Rabinovich, A.B., Bornhold, B.D., Thomson, R.E. and Kulikov, E.A. The Grand Banks landslide-generated tsunami of November 18, 1929: preliminary analysis and numerical modeling // Marine Geology 2005, vol. 215, 45-57.

12. Fritz, H.M., Mohammed, F. and Yoo, J. Lituya Bay Landslide Impact Generated Mega-Tsunami 50th Anniversary // Pure Appl. Geophys., 2009, vol. 166, 153-175.

13. Goto, C., Ogawa, Y., Shuto, N. and Imamura, N. Numerical method of tsunami simulation with the leap-frog scheme (IUGG/IOC Time Project), IOC Manual, UNESCO, no. 35, 1997, 96 p,

14. Grilli, S.T., Vogelmann, S. and Watts, P. Development of 3D numerical wave tank for modeling tsunami generation by underwater landslides // Engineering Analysis with Boundary Elements, 2002, vol.26, 301-313.

15. Grilli, S.T., Kirby, J.T., Liu, P.L.F., Brandes, H. and Fryer, G.J. «Workshop on Model Validation and Benchmarking For Tsunami Generation by Submarine Mass Failure - Proposal Submitted to NSF», 2003, Honolulu, Hawaii.

16. Gusev, O.I., Shokina, N.Y., Kutergin, V.A. and Khakimzyanov, G.S. Numerical modelling of surface waves generated by underwater landslide in a reservoir // Vycisl. tehnologii – Computational Technologies, 2013, vol. 8, no. 5, 74-90 [In Russian].

17. Harbitz, C.B., Løvholt, F., Pedersen, G. and Masson, D.G. Mechanisms of tsunami generation by submarine landslides: a short review // Norwegian Journal of Geology, 2006, vol. 86, 255-264.

18. Hirt, C.W. and Nichols, B.D. Volume of Fluid (VOF) method for the dynamics of free boundaries // Journal of Computational Physics, 1981, vol. 39, 201-225.

19. Heinrich, P., Schindele, F., Guibourg, S. and Ihmle, P. Modeling of the February 1996 Peruvian tsunami // Geophys. Res. Lett. 1998, vol. 25, no. 14, 2687-2690.

20. Heinrich, F., Boudon, G., Komorowski, J.C., Sparks, R.S.J., Herd, R. and Voight, B. Numerical simulation of the December 1997 debris avalanche in Montserrat // Geophys. Research Letters, 2001, vol. 28, 2529-2532.

21. Horrillo, J., Wood, A., Kim, G.B. and Parambath, A. A simplified 3-D Navier-Stokes numerical model for landslide-tsunami: Application to the Gulf of Mexico // Journal of Geophysical Research: Oceans, 2013, vol. 118, 6934-6950.

22. http://tsun.sscc.ru/hiwg (accessed 3 July 2015).
23. https://www.ngdc.noaa.gov (accessed 25 April 2015).

24. Imamura, F. and Imteaz, M.A. Long waves in two-layers: Governing equations and numerical model // Science of Tsunami Hazards, 1995, vol. 13, no. 1, 3-24.

25. Jasak, H. Error Analysis and Estimation for the finite volume method with applications to fluid flows. Thesis submitted for the degree of doctor. – London: Department of Mechanical Engineering, Imperial College of Science, 1996.

26. Kirby, J., Wei, G., Chen, Q., Kennedy, A. and Dalrymple, R. Fully Nonlinear Boussinesq Wave Model Documentation and Users Manual // Center for Applied Coastal Research Department of Civil Engineering University of Delaware, Newark DE 19716, Research Report №. CACR-98-06, 1998.

27. Kolev, N. Multiphase Flow Dynamics. – Berlin, Heidelberg: Springer-Verlag, 2007.

28. Kozelkov, A.S., Deryugin, Yu.N., Lashkin, S.V., Silaev, D.P., Simonov, P.G. and Tyatyushkina, E.S. Implementation in LOGOS software of a computational scheme for a viscous incompressible fluid using the multigrid method based on an algorithm SIMPLE // VANT. Ser.: Mat. Mod. Phys. Proc., 2013. no. 4, 31-43. [In Russian]

29. Kozelkov, A.S., Kurkin, A.A., Pelinovsky, E.N., Kurulin V.V. and Tyatyushkina, E.S. Modeling the Disturbances in the Lake Chebarkul Caused by the Fall of the Meteorite in 2013 // Fluid Dynamics, 2015, vol. 50, no. 6, 828-840.

30. Kozelkov, A.S. and Kurulin, V.V. Eddy resolving numerical scheme for simulation of turbulent incompressible flows // Computational Mathematics and Mathematical Physics, 2015, vol. 55, no. 7, 1255-1266.

31. Kozelkov, A.S., Kurkin, A.A., Legchanov, M.A., Kurulin, V.V., Tyatyushkina, E.S. and Tsibereva, Y.A. Investigation of the application of RANS turbulence models to the calculation of nonisotermal low-Prandtl-number flows // Fluid Dynamics, 2015, vol. 50, no. 4, 501-513.

32. Kozelkov, A.S., Kurkin, A.A., Pelinovsky, E.N. and Kurulin V.V. Modeling the cosmogenic tsunami within the framework of the Navier–Stokes equations with sources of different types // Fluid Dynamics, 2015, vol. 50, no. 3, 306-313.

33. Kozelkov, A., Kurulin, V., Emelyanov, V., Tyatyushkina, E. and Volkov, K. Comparison of convective flux discretization schemes in detached-eddy simulation of turbulent flows on unstructured meshes // Journal of Scientific Computing, 2016a, vol. 67, 176-191.

34. Kozelkov, A.S., Shagaliev, R.M., Kurulin, V.V., Yalozo, A.V. and Lashkin S.V. Investigation of Supercomputer Capabilities for the Scalable Numerical Simulation of Computational Fluid Dynamics Problems in Industrial Applications // Computational Mathematics and Mathematical Physics, 2016b, vol. 56, no. 8, 1506-1516.

35. Kozelkov, A. and Pelinovsky, E. Tsunami of the meteoritic origin // In Book «Dynamics of Disasters - key Concepts, Models, Algorithms, and Insights», Eds: Kotsireas I.S. et al., Springer Proceedings in Mathematics & Statistics 185, Berlin: Springer, 2016. DOI 10.1007/978-3-319-43709-5_8

36. Langford, P.S. Modeling of tsunami generated by submarine landslides. PhD Thesis. – New Zealand: University of Canterbury, 2007.

37. Liu, P.L.-F., Wu, T.-R., Raichlen, F., Synolakis, C.E. and Borrero, J.C. Runup and rundown generated by three-dimensional sliding masses // J. Fluid Mech., 2005, vol. 536, 107-144.

38. Lynett, P. and Liu, P.L.-F. A numerical study of the run-up generated by three-dimensional landslides // Journal of Geophysical Research, 2005, vol. 110, C03006.

39. Lynett, P. Hydrodynamic Modeling of Tsunamis Generated by Submarine Landslides: Generation, Propagation, and Shoreline Impact // 4-th International Symposium Submarine Mass Movements and Their Consequences, Advances in Natural and Technological Hazards Research, 2010, vol. 28, 685-694.

40. Ma, G., Kirby, J.T. and Shi, F. Numerical simulation of tsunami waves generated by deformable submarine landslides // Ocean Modelling, 2013, vol. 69, 146-165.

41. Macías, J., Vázquez, J.T., Fernández-Salas, L.M., González-Vida, J.M., Bárcenas, P., Castro, M.J., Díaz-del-Río, V. and Alonso, B. The Al-Borani submarine landslide and associated tsunami. A modelling approach // Marine Geology, 2015, vol. 361, 79-95.

42. Mohammed, F. and Frits, H.M., Experiments on tsunamis generated by 3D Granular Landslides // Submarine Mass Movements and Their Consequences, Advances in Natural and Technological Hazards Research, 2010, vol. 28, 705-718.
43. Mohammed, F. Physical Modeling of tsunamis generated by three-dimensional deformable granular landslides. PhD Thesis. – Atlanta: Georgia Institute of Technology, 2010.
44. Nikolkina, I.F., Pelinovsky, E.N. and Talipova, T.G. Nonlinear dynamics of gravity flows in sloping channels // Doklady Earth Sciences, 2010, vol. 432, pt. 2, 812-815.
45. Okal, E. and Synolakis, C.E. A Theoretical comparison of tsunamis from dislocations and landslides // Pure Appl. Geophys., 2003, vol. 160, 2177-2188.

46. Papadopoulos, G.A. and Kortekaas, S. Characteristics of Landslide Generated Tsunamis From Observational Data // Submarine Mass Movements and Their Consequences Advances in Natural and Technological Hazards Research., 2005, 367-374.
47. Pelinovsky, E.N. Analytical models of tsunami generation by submarine landslides // In NATO Science Series, ed. by A. Yalciner et al., Earth Environ. Sci., 21, Kluwer, Dordrecht, Boston 2003, 111-128.

48. Pelinovsky, E., Kozelkov, A., Zahibo, N., Dunkly, P., Edmonds, M., Herd, R., Talipova, T. and Nikolkina, I. Tsunami generated by the volcano eruption on July 12-13, 2003 at Montserrat, Lesser Antilles // Science of Tsunami Hazards, 2004, vol. 22, no. 1, 44-57.

49. Rabinovich, A.B., Thomson, R.E., Bornhold, B.D., Fine, I.V. and Kulikov, E.A. Numerical modelling of tsunamis generated by hypothetical landslides in the Strait of Georgia, British Columbia // Pure Appl. Geophys., 2003, vol. 160, 1273-1313.

50. Rhie, C.M. and Chow, W.L. A numerical study of the turbulent flow past an isolated airfoil with trailing edge separation // AIAA, 1983, vol. 21, 1525-1532.

51. Sælevik, G., Jensen, A. and Pedersen, G. Experimental investigation of impact generated tsunami; related to a potential rock slide, Western Norway // Coastal Engineering, 2009, vol. 56, 897-906.

52. Ubbink, O. Numerical prediction of two fluid systems with sharp interfaces. PhD Thesis. – London: Department of Mechanical Engineering Imperial College of Science, Technology & Medicine, 1997.

53. Volkov, K.N. and Emelyanov, V.N. Particle laden flows. – Moscow: Fizmatlit, 2008. 600 p. [In Russian].

54. Volkov, K.N., Deryugin, Yu.N., Emelyanov, V.N., Karpenko, A.G., Kozelkov, A.S. and Teterina, I.V. Methods of the detached eddy for gas-dynamic calculation on unstructured grids. – Moscow: Fizmatlit, 2013. 536 p. [In Russian].

55. Volkov, K.N., Deryugin, Yu.N., Emelyanov, V.N., Kozelkov, A.S. and Teterina, I.V. Difference schemes in problems of gas dynamic on unstructured grids. – Moscow: Fizmatlit, 2014. 416 p. [In Russian].

56. Watts, P., Grilli, S.T., Kirby, J.T., Fryer, G.J. and Tappin, D.R. Landslide tsunami case studies using a Boussinesq model and a fully nonlinear tsunami generation model // Natural Hazards and Earth System Sciences, 2003, vol. 3, 391-402.

57. Watts, P. and Grilli, S.T. Underwater landslide shape, motion, deformation, and tsunami generation // Proc. of the 13th Intern. Offshore and Polar Eng. Conf., Honolulu, Hawaii, 2003, vol. 3, 364-371.

58. Waclawczyk, T. and Koronowicz, T. Remarks on prediction of wave drag using VOF method with interface capturing approach // Archives of civil and mechanical engineering, 2008, vol. 8, 5-14.

59. Watts, P., Imamura, F., Bengston, A. and Grilli, S.T. Benchmark cases for tsunamis generated by underwater landslides // Proceedings of the Fourth International Symposium Waves, San Francisco, 2001, 1505-1514.

60. Watts, Ph. and Waythomas, C.F. Theoretical analysis of tsunami generation by pyroclastic flows // Journal of Geophysical Research, 2003, vol. 108, no. B12, 21 p.

61. Zahibo, N., Pelinovsky, E., Talipova, T. and Nikolkina, I. The Savage-Hutter model for the avalanche dynamics in inclined channels: analytical solutions // J. Geophys. Res., 2010, vol. 115, B03402.

ISSN 8755-6839

SCIENCE OF **TSUNAMI HAZARDS**

Journal of Tsunami Society International

Volume 35 **Number 3** **2016**

ASSESSING LANDSLIDE-TSUNAMI HAZARD IN SUBMARINE CANYONS, USING THE COOK STRAIT CANYON SYSTEM AS AN EXAMPLE

William Power
GNS Science, 1 Fairway Drive, Avalon, Lower Hutt, New Zealand
Joshu Mountjoy
NIWA, 301 Evans Bay Parade, Hataitai, Wellington, New Zealand
Emily Lane
NIWA, 10 Kyle Street, Riccarton, Christchurch, New Zealand
Stephane Popinet
Université Pierre et Marie Curie, 4 Place Jussieu, 75005 Paris, France
Xiaoming Wang
GNS Science, 1 Fairway Drive, Avalon, Lower Hutt, New Zealand

ABSTRACT

Tsunami generated by submarine landslides are now recognised as an important hazard, following several historical events. Submarine landslides can occur in a variety of settings such as on continental slopes, volcanic slopes, and submerged canyons and fjords. While significant progress has been made in understanding tsunami generation processes on open slopes, the problem of tsunami generation by landslides within submarine canyons has received less attention. In this paper we examine the tsunami hazard posed by submarine landslides in the Cook Strait canyon system, near Wellington, New Zealand. Understanding of the hazard posed by this tsunami source has practical value because of its proximity to a populated coast. Our studies also provide general results highlighting the differences between tsunami generation on open coasts and tsunami generation

within canyons. Geotechnical and geological studies of the Cook Strait region reveal evidence for many large landslide scars in the canyon walls, these are interpreted to be failures of consolidated material which descend the slopes on the sides of the canyon. Scouring of the base of the canyon slopes by strong tidal currents is believed to be an important process in bringing slopes to the point of failure, with most large failures expected to occur during earthquake shaking. We present the results of computer simulations of landslide failures using simplified canyon geometries represented in either 2D (vertical slice) or 3D. These simulations were made using Gerris, an adaptive-grid fluid dynamics solver. A key finding is that the sudden deceleration of the landslide material after reaching the canyon floor, leads to larger amplitude waves in the back-propagation direction (i.e. in the opposite direction to the initial landslide motion).

1. INTRODUCTION

Submarine landslide-generated tsunami are now a widely recognised hazard with documented historical events (Fine et al., 2005; Labbe et al., 2012; Rahiman et al., 2007; Tappin et al., 2008), landslide-specific hazard assessments (e.g. Argnani et al., 2011; Iglesias et al., 2012; Walters et al., 2006), and a limited number of regional hazard assessments (e.g. Grilli et al., 2009). Submarine landslides are recognised to occur in relatively specific geological environments, including open slopes, submarine canyons, fiords, and volcanic cones and ridges (Hampton et al., 1996). Submarine canyons are an environment where relatively few landslide studies have been carried out, yet where the hazard associated with landslide-generated tsunami may be high due to steep slopes, proximity to land, and the potential for landward-directed slope failures.

Whereas much of the world's landmass sits adjacent to a wide continental shelf, providing a buffer zone to continental slopes, submarine canyons enable areas of steeply sloping seafloor to come within close proximity of populated coastal areas. Examples of canyons in reasonably close proximity to populated areas can be found in Mediterranean Europe, Central eastern USA, and New Zealand. In comparison to open slopes, where landslide features are commonly beautifully preserved (e.g. Berndt et al., 2012), landslides in submarine canyons are frequently represented by relatively subtle geomorphic features (e.g. Greene et al., 2002; Lastras et al., 2007; Mountjoy et al., 2009). Landslides in submarine canyons typically occur on canyon walls and can be subject to geologically rapid post-failure modification, making them difficult to parameterise. In addition, failure often involves bedrock rather than recent sedimentary deposits adding additional complications for landslide analysis.

An important aspect of the submarine canyon geological environment in terms of landslide tsunami hazard is that material is falling into a confined seafloor environment, meaning that failed slope material and hydrodynamic disturbance is likely to interact with the complex terrain of the canyon system. Modelling of landslide-tsunami sources has predominantly considered material displaced down a planar slope with an unconstrained lower boundary (e.g. Ward, 2001; Watts et al., 1999). Applying this simplified source geometry to the complex terrain in submarine canyons may not be appropriate and could lead to failure to identify wave focussing areas, and under-estimation of the tsunami hazard.

Here we use a regional case study to explore the difficulties associated with landslide-generated tsunami hazard analysis in complex canyon terrain. The Cook Strait canyon system in New Zealand is a large submarine canyon that comes within 15 km of the capital city of Wellington, and has a large number of mapped submarine landslide scars (Micallef et al., 2012; Mountjoy et al., 2009). We present some results for this specific area regarding the age distribution of observed landslides, as this is a particularly difficult issue for landslide-tsunami hazard assessments. However the study is primarily focussed on identifying pitfalls for landslide-generated tsunami studies in submarine canyon terrain and suggesting a way forward for quantifying landslide tsunami hazard and risk in these complex environments.

We also present a modelling study into the tsunami-generation properties of landslides on canyon slopes, with particular regard for the differences compared to tsunami-generation on open slopes. The geometrical model of a submarine canyon that is used as the baseline for these studies is based on a simplified cross-section of part of the Cook Strait Canyon, yet is sufficiently generic to be used to draw general conclusions. Modelling was conducted using Gerris, a solver for the variable density Navier-Stokes equations, permitting more accurate fluid dynamics to be represented than can be achieved using standard depth-integrated tsunami models. The specific features of tsunami-generation by slope failures in canyon systems were investigated by varying the representation of the far wall, i.e. the slope opposite the mass failure, in the geometrical model of the canyon.

2. LOCAL SETTING

The seaway of Cook Strait divides North Island and South Island of New Zealand. The Cook Strait canyon system is a deeply incised submarine canyon formed on the continental slope of the southern Hikurangi Margin subduction system (Figure 1). The canyon is highly sinuous across the continental slope but branches into three canyon heads from the shelf break and extends 40 km across the continental shelf. Following Mountjoy et al (2013) the Cook Strait canyon system is divided into four components: the upper canyons - Cook Strait Canyon, Nicholson Canyon, and Wairarapa Canyon; and the Lower Cook Strait Canyon which extends from the shelf break to the deep sea Hikurangi Channel (Figure 1). In this study we focus on the upper, shelf-incising canyons as these are in shallower ocean depths, and come closer to land, meaning they are most likely to pose a tsunami hazard.

The head of Nicholson Canyon lies just 8 km off the coast of Wellington, New Zealand's capital city with a population of approximately 400,000. Wairarapa Canyon is just over 1 km from the coast at its closest point and all three of the upper canyons are less than 20 km from the coastline. The upper canyon rims vary in water depth from 50 – 200 m, and the canyon floor depths from 250 – 1200 m depth. The upper canyons are between 18 and 45 km long and 3 – 10 km wide.

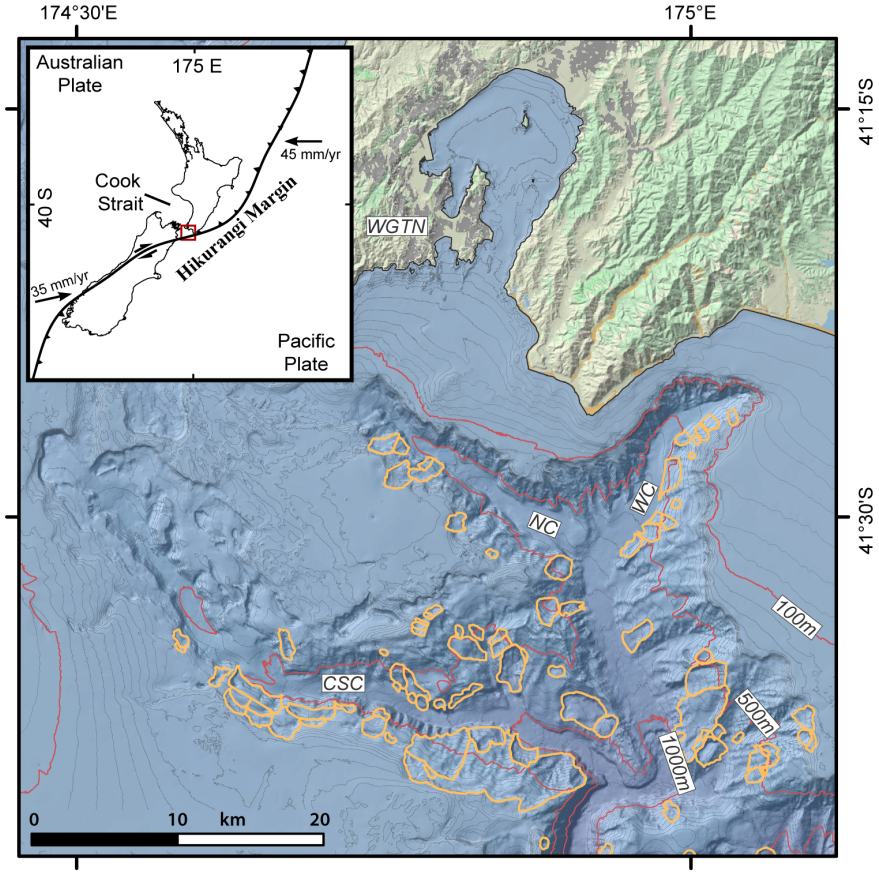

Figure 1. Regional setting. A) Study location in the context of the New Zealand tectonic setting. B) Canyon physiography showing mapped landslides (after Micallef et al. 2012). 'NC' is Nicholson Canyon, 'WC' is Wairarapa Canyon, 'CSC' is Cook Strait Canyon, and 'WGTN' labels the southern suburbs of Wellington City.

2.1 Tectonic and geologic setting

The Cook Strait canyon system sits at the southern termination of the Hikurangi Margin at the transition from subduction to continental collision on the Pacific-Australian plate boundary. Reflecting this active plate boundary setting, the region is dissected by numerous active faults that can be divided into reverse faults related to contraction in the convergent margin and strike slip faults from partitioning of oblique strain (Pondard and Barnes, 2010). In New Zealand's largest historical earthquake, the Wairarapa Fault ruptured in 1855 producing a Mw 8.2 earthquake centred onland and extending into the Nicholson and Wairarapa canyons (Barnes, 2005; Dowrick, 2005). Terrestrial seismic hazard assessments indicate that areas of the Wellington region are capable of producing peak ground accelerations (pga) greater than 0.4g at a 475 year return period, and they can exceed 1.0g at a 2500 year return period (Stirling et al., 2012). Earthquake ground shaking is thought to be the main trigger of slope failure within the canyon system (Micallef et al., 2012; Mountjoy et al., 2013).

2.2 Landslides in the Cook Strait Canyon System

130 landslides have been mapped through the Cook Strait canyon system (Figure 1). Landslides are recognised solely by scars in the canyon walls and canyon floor, as almost no evidence of landslide deposits remains in the system. Based on scar geometry, the metrics of the landslide source areas can be quantified in terms of key parameters like volume, failure depth and slope angle of the basal failure surface (Figure 2). These data indicate a predominance of landslides at volumes less than $10x10^6$ m^3, however a few failures are also above $1x10^8$ m^3. Frequency histograms of landslide depth have a peak between 70-90 m defining them as deep seated. The failure angle of the basal surface is predominantly controlled by bedrock structure and is mainly less than 10°, though it is likely that this value is overestimated as surficial material covering the landslide scar will skew results.

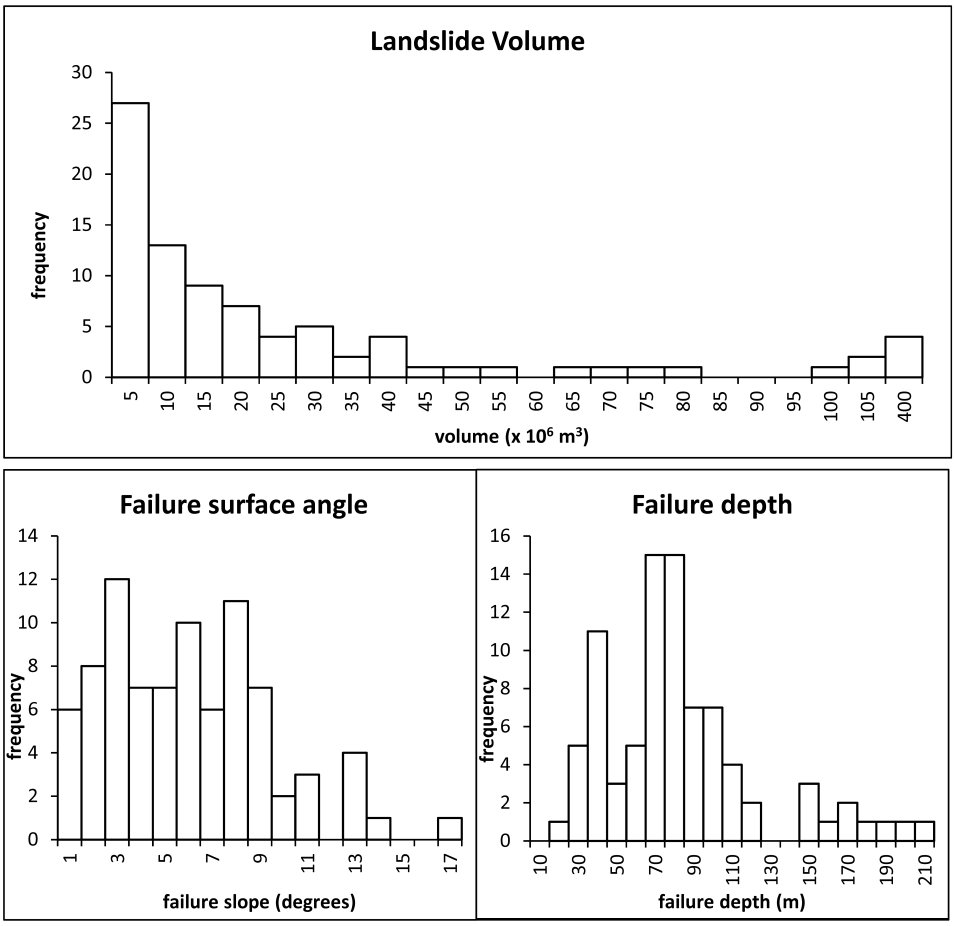

Figure 2. Landslides metrics after Micallef et al. (2012). Frequency histograms have been derived from measured geometries of landslide scars in multibeam bathymetry. Note the last bin for Landslide Volume is discontinuous in terms of scale.

3. DATA AND METHODS

3.1 Determining Landslide Age

Geophysical data and geological samples were collected in 2011 during the *RV Tangaroa* voyage Tan1103 (Mountjoy et al., 2013). Data relevant to this study was collected from several landslide scars within the canyon to assess the age of landslides (Table 2). Cores were collected with a standard gravity corer using a 6 m long barrel and a 1.2 tonne weight. Cores were capped and stored upright on-board then transferred to a refrigerated facility and logged onshore. Radiocarbon dating has been carried out on carbonate material (shell fragments or benthic foraminifera) picked from these sediment samples to determine sedimentation rates. The combination of sediment thickness and sedimentation rate data allow determination of the age of the surface underlying the sediment drape.

Digital high-resolution seismic data was collected using a hull-mounted Knudsen Chirp 3260 3.5 kHz Subbottom Profiler. Sub-bottom penetration was to a maximum of 60 m.

3.2 Modelling methodology

The modelling for this work took place in two parts. The first part investigated the process of the tsunami wave being created by the submarine mass failure, identifying general features that differentiate tsunamis caused by landslides in canyons from those on open slopes. This was done using modelling of simplified geometries in 2D (vertical slice) and 3D. The second part developed a scenario model specific to the Nicholson Canyon of Cook Strait, based on the actual seafloor bathymetry of this location and modelled the effect of that scenario.

The modelling was conducted using Gerris. Gerris is an extensible framework for the solution of partial differential equations describing fluid flows and other phenomena (Popinet, 2003). Gerris solves the variable-density Navier-Stokes equations with boundary conditions at the interface between phases, and uses adaptive mesh refinement to allow the model to adjust dynamically to the details of the problem being solved. For the purposes of long-range tsunami propagation modelling, Gerris can also solve the (depth-averaged) non-linear shallow water equations to simulate tsunami propagation over real bathymetry. The code is parallelised to enable speeding-up of expensive computations.

Navier-Stokes equation solver in Gerris was used to simulate the processes of landslide failure and wave generation at water surface in vertically 2D slice modelling and 3D modelling. Using a volume of fluid (VoF) approach, the air and water are represented by different phases of fluid. The landslide was modelled both as a third dense semi-rigid fluid. Solid boundaries were used at the edges of the domain for the VoF modelling. In the specific scenario the propagation of tsunami away from the source region was modelled with non-linear shallow water equation solver in Gerris using the water surface displacement and depth-averaged velocities from 3D modelling as initial condition. A subcritical boundary condition was used for sea boundaries allowing the tsunami energy to propagate out of the domain (Bristeau and Coussin, 2001).

3.3 Generalised landslide modelling

For the purposes of using a 2D vertical slice model to study the influence of canyon walls on tsunami generation, a baseline configuration was developed as shown in Figure 3. This geometry was based approximately on that estimated for past and future landslides in a cross-section of Nicholson Canyon. By modelling a landslide and subsequent tsunami in the baseline configuration, and then varying individual parameters, it was possible to estimate the sensitivity of tsunami wave generation to those parameters.

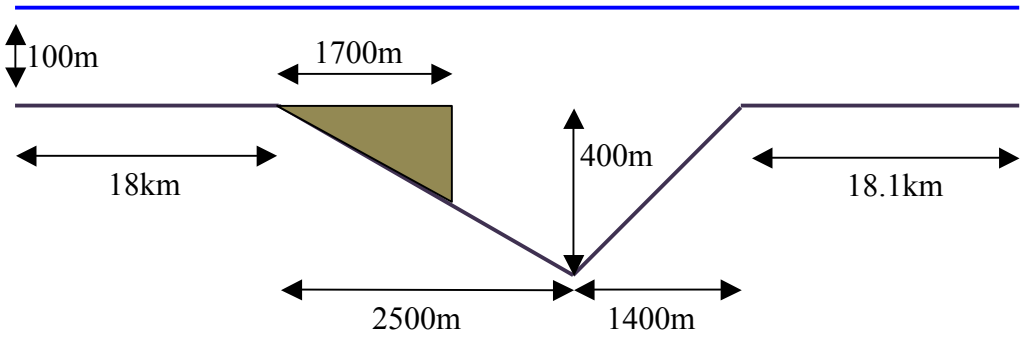

Figure 3. Baseline geometry used for modelling of a sliding block descending into a canyon. X co-ordinates in subsequent figures are measured relative to the position of the left post-landslide lip of the canyon.

For the purposes of this model it was assumed that the landslide material slides as a coherent block until the point where it hits the bottom of the canyon, after which it is assumed to behave as a dense fluid (due to break-up of the landslide body). This was achieved in Gerris by tracking the centre of mass motion of the slide and constraining the velocities in model-grid cells within the slide body to equal the centre of mass velocity until the canyon bottom was reached. The relative density of the landslide was assumed to be 2.0.

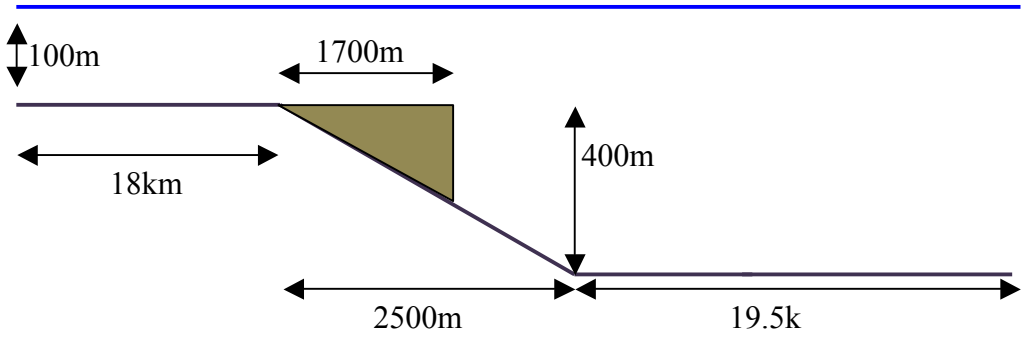

Figure 4. Geometry used for the models of a sliding block descending an open slope to a flat bottom. The influence of the far canyon wall was studied by constructing an alternative model in which there was no far wall, i.e. an open slope leading to a flat bottom. In this model the sliding block still descends as a solid body, but is assumed to become a dense fluid once it reaches the bottom of the slope.

A third configuration was also modelled in order to better understand the role of the far canyon slope. In this configuration the far wall is assumed to be almost vertical (Figure 5).

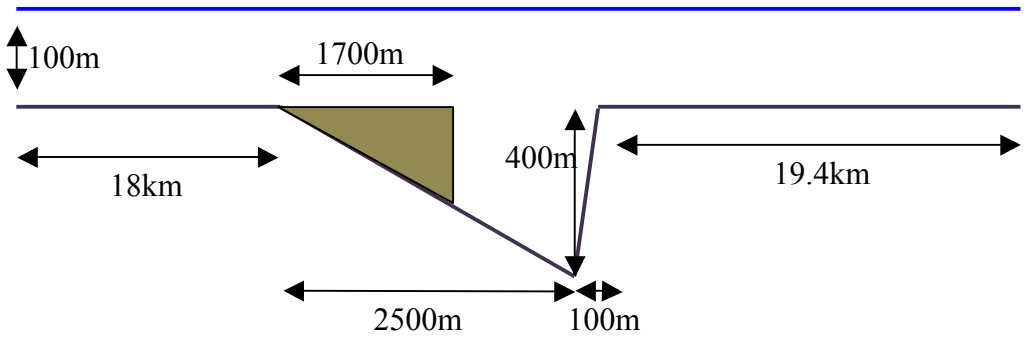

Figure 5. Geometry used for the models of a sliding block descending to a canyon with a very steep (near vertical) far wall.

Equivalent 3D simulations were conducted to investigate the effect the finite width of the landslide has on tsunami wave created. Figure 6 shows the configuration modelled. The cross-sections of the landslide and canyon remains the same as the baseline shown in Figure 3. However the landslide has

a finite width while the canyon extends unchanged in both directions.

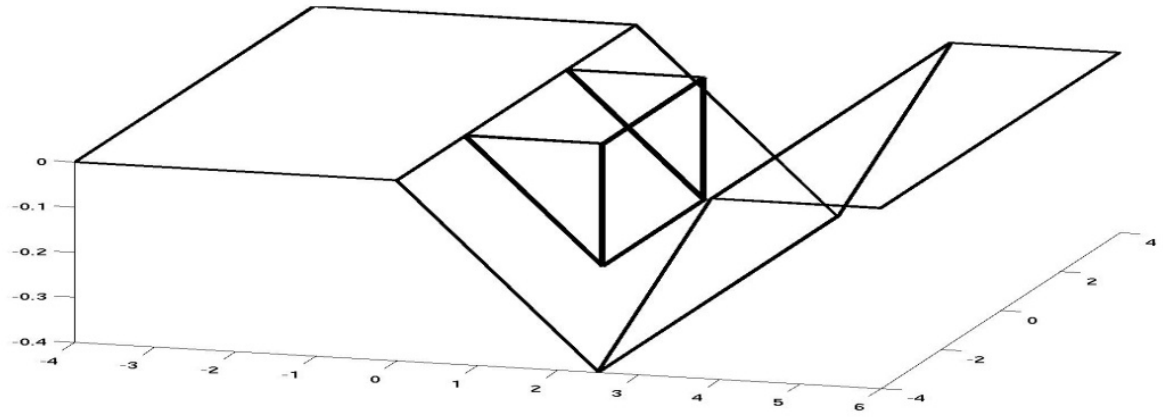

Figure 6. Three dimensional equivalent of baseline landslide geometry (Figure 3), dimension labels are in km. For the baseline 3D scenario the width of the slide, along the canyon axis, was 1.7km, in cross-section (perpendicular to the canyon axis) the dimensions are the same as in Figure 3.

The width of the landslide was varied from 1km, to 1.7km, to 2.5km and separate simulations made for each case, in order to understand how the validity of the 2D approximation varies according to the width of the slide. Watts et al (2005) discuss approaches for approximating 3D models with 2D vertical slice models, these use functions of the slide width to correct for the radiation in off-axis directions.

3.4 Cook Strait landslide modelling

In Section 2 potentially tsunamigenic submarine landslides within the Cook Strait region were identified. An estimate of the likely worst case scenario, in terms of overall impact on people and the built environment, in this region was identified as being caused by a landslide on the south side of Nicholson Canyon. The head of this canyon lies within 10 km of Wellington (see Figure 1). Table 1 shows the parameters used for modelling of this scenario.

Slide Parameters	**Nicholson Canyon**
Latitude (^{0} N)	-41.46
Longitude (^{0} E)	174.8
Azimuth (^{0})	50
Depth (m)	250
Slope (^{0} down from horizontal)	11.31
Length (m)	1500
Width (m)	1500
Thickness (m)	200
Volume (km^3)	0.4
Relative Density	2.0

Table 1. Parameters used in 3D initialisation of the Nicholson Canyon scenarios

This scenario was modelled in 3D as a rigid descending block, similar to that in Figure 6, which becomes a dense fluid after reaching the bottom of the canyon. After 100 seconds of modelled time had elapsed the water surface state and the depth-integrated velocity were used to form inputs to the non-linear shallow-water equation tsunami propagation model. Bathymetric and topographic data for this model were compiled from Land Information New Zealand bathymetric charts and ?.

4. RESULTS

4.1 Landslide age models

To get the required magnitude frequency model for landslide occurrence the most difficult aspect is determination of the frequency with which landslides occur. Whereas tectonic faulting is a repeated process over longer time periods mass instability is more of a stochastic process being dependant on many different local and external forcing factors. Any model for landslide recurrence requires some validation of the determined age model. A first order validation for this is the known ages of prior landslides, giving an indication that landslides are occurring over short enough timescales to pose a hazard.

To provide some validation that there is a landslide tsunami hazard associated with the Cook Strait Canyons we have analysed data from four separate landslides to get an idea of the age population of the landslides observed in geomorphology.

4.2 Radiometric dating results

Benthic Foraminifera and shell fragments extracted from sediment near the base of sediment cores have been dated using c14 radiometric dating techniques (Table 2). A local, averaged sediment accumulation rate is calculated between the seafloor (t=0) and the depth of the dated horizon. Other radiocarbon analysis in the Cook Strait canyons (Mountjoy et al., 2013) has shown that dating of foraminifera is unreliable for definite ages, likely due to both the lack of hemipelagic material and reworking of foraminifera material. However dates provide a maximum for stratigraphic ages as material cannot be older than the reported age but could be younger if reworked.

Table 2: Landslide dating data

Core ID	Date depth	C14 date (yrs BP)	Cover depth	Landslide age (yrs BP)
Stn 18	1.8 m	14217 +/- 127	NA	14217 +/- 127[1]
Stn 32	2.7 m	1031 +/- 85	6.96 +/- 0.2 m	2658 +/- 295
Stn 37	2.5 m	159 +/- 79	3.2 +/- 0.2 m	204 +/- 125
Stn 42	2.4 m	1470 +/- 75	5.84 +/- 0.2 m	3090 +/- 486

[1]The calibrated age is for material from sea level lowstand, which agrees with relict shell hash material observed in core. This age is applied to the landslide scar with no assumption of accumulation rate.

4.3 Subsurface imaging

To determine the amount of sediment that has been placed over the evacuated landslide scars since failure occurred we analyse high resolution (3.5 kHz) seismic reflection data. The example shown in Figure 8 illustrates the thin sediment drape overlying a landslide scar in Wairarapa Canyon.

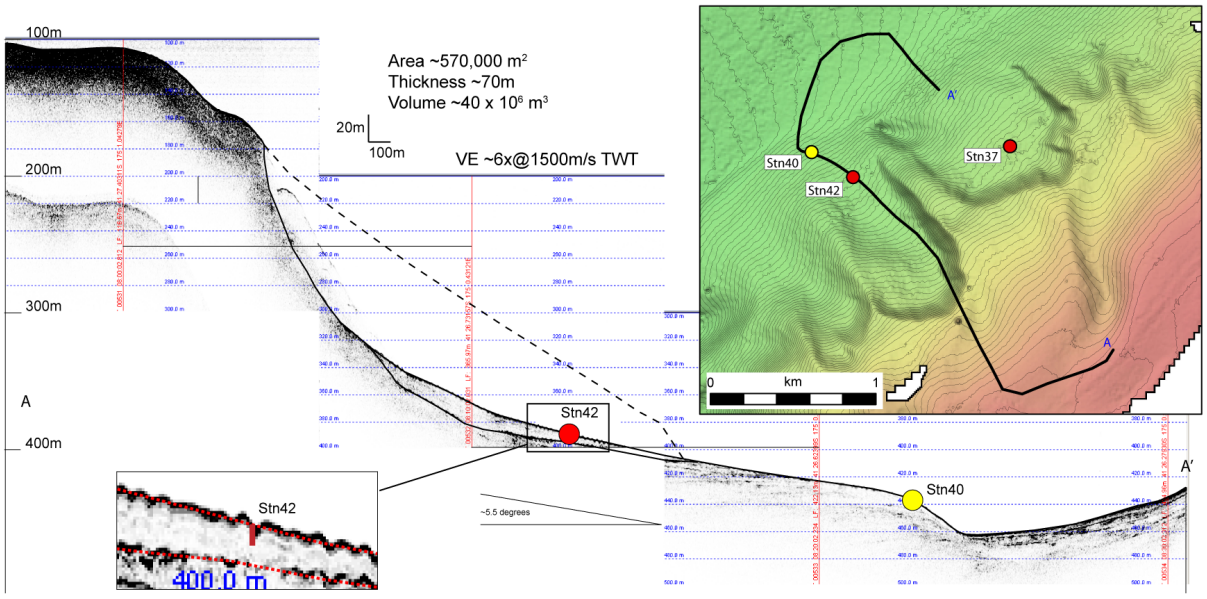

Figure 8. Example of date extrapolation through cover sequence to date landslide in 3.5 kHz seismic reflection. Dashed black line shows interpreted pre-failure geometry of slope. Inset detail shows cover sequence (red dash line) and penetration depth of core at Stn42.

The accumulation rate for this location in Table 2 is extrapolated to the full thickness of sediment overlying the landslide failure surface to determine the age of the scar (Table 2). Age uncertainty takes into account C14 dating error and measurement error in picking seismic horizons. Issues with this landslide age determination technique include inherited age in sediment (date is for older material transported from somewhere else), variation in sedimentation rates, the possibility of a polyphase landslide mechanism, and velocity variation in seismic depth conversion. In this case, the proximity of the adjacent much younger landslide (Stn37) with a very similar geomorphology suggest that the landslide illustrated in Figure 8 may be younger than the dating suggests. Regardless these age determinations indicate a range of post-glacial (20,000 BP) ages for the landslides in the canyon system.

4.4 Tsunami Modelling of canyon landslide in vertical cross-section

2D tsunami wave generation was modelled as described in Section 3 for the three cases of the baseline canyon, the open slope, and the vertical far wall, as shown in Figures 3, 4 and 5 respectively.

Results from these simulations are shown in Figures 9 and 10. Figure 9 shows the water surface at 100 second intervals following the landslide initiation. Figure 10 shows the water level time history above a point 4km from the canyon rim on the 'near' side (i.e. X=-4000 m, to the left of the canyon rim as it appears in Figures 3,4,5).

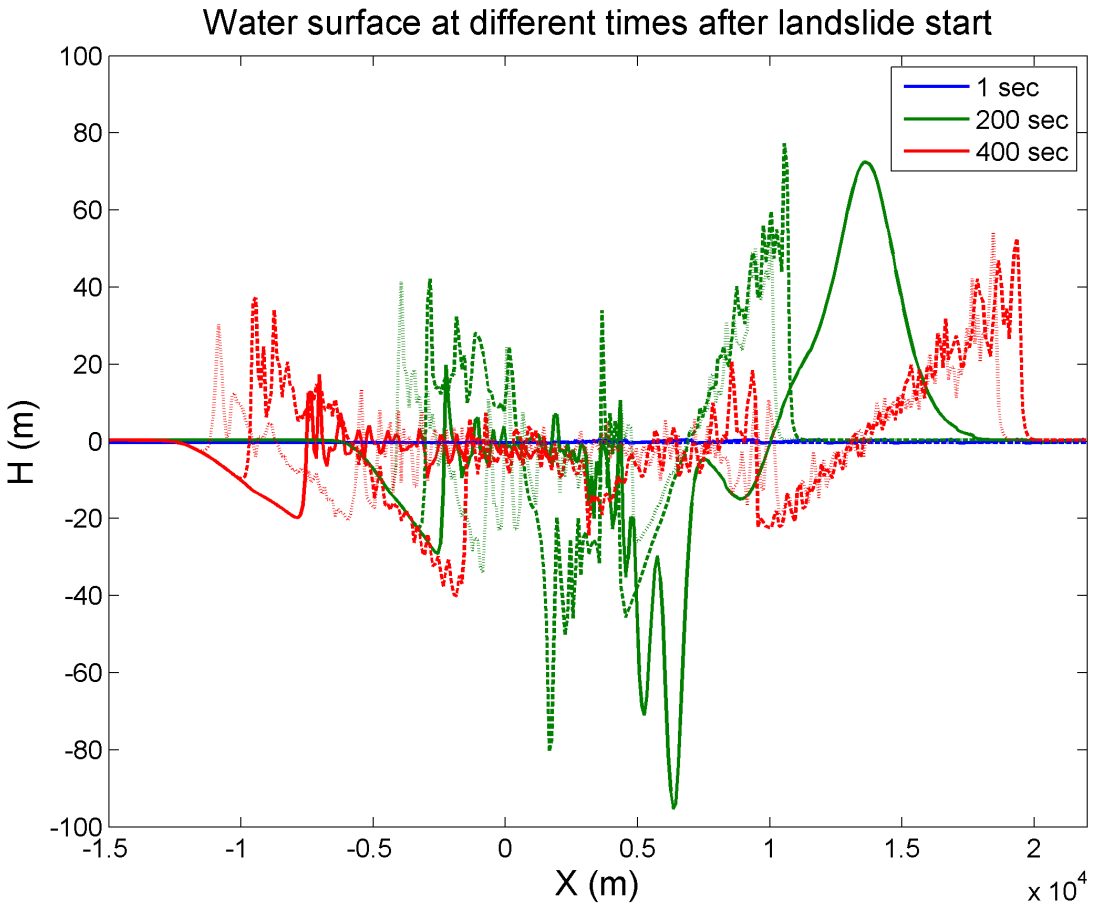

Figure 9. Water surface snapshots at 200 second intervals after landslide initiation, shown for the three geometric configurations described in the text: no-far wall (solid), the baseline canyon cross-section (dashed), and the very steep far-wall canyon (dotted). The no-far-wall case is not shown for +ve X at t=400 s; this is to avoid unrealistic effects caused by reflections from the edge of the simulation domain.

From Figure 9 we can see that the leading positive wave on the 'near' side of the canyon comes progressively earlier as we go from having a steep far wall to the baseline canyon to having no far wall. This suggests the timing of the first positive wave is related to the deceleration of the descending body. On the 'far' side of the canyon the leading wave, which is positive, travels faster in the absence of the far wall – which is to be expected given that tsunami wave speed is greater in water of greater depth.

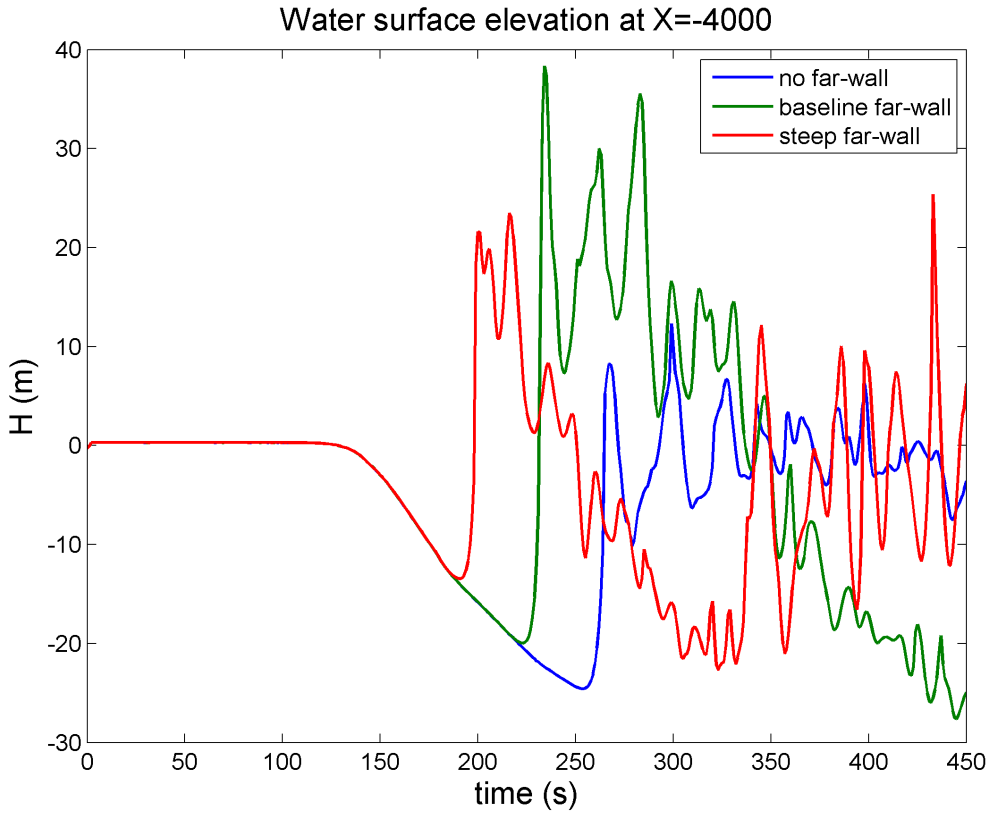

Figure 10: Water surface time histories at position X=-4000 m, shown for the three geometric configurations described in the text: no-far wall (blue), the baseline canyon cross-section (green), and the very steep far-wall canyon (red).

Analysing Figure 10 we see that the presence of the far canyon wall makes a big difference to the amplitude of the subsequent wave on the 'near' side of the canyon. In this example the elevation of the peak of the wave is about three times greater in the canyon geometry compared to the open slope case; this dramatically highlights the differences between tsunami generated by landslides in the two situations, and why it is important for hazard assessment not to model canyon landslide tsunami sources using procedures and approximations that assume an open slope. The role of landslide deceleration on tsunami generation has also been studied in laboratory experiments by Sue et al (2011).

4.6 Relationship between 2D and 3D models of canyon landslides

Two dimensional vertical slice (2D) modelling is significantly less demanding of computer time than fully three dimensional (3D) modelling. Hence it is useful to evaluate the differences in results for equivalent scenarios in these two cases. Results of such a comparison appear in Figure 11. Here the 2D wavefield along the axis of the cross-section is compared against the equivalent 3D model for

landslides of different width in the along-canyon direction. What we see is that the 2D model overestimates the wave heights compared to the 3D case, as would be expected due to the finite width of the landslide in the 3D case as energy is radiated in the off-axis directions. The degree of overestimation reduces as the landslide width (in the canyon axis) increases. Ultimately, for a theoretical infinitely wide landslide, the two results should converge.

Qualitatively the 2D and 3D solutions show the same basic features. The question of how a 3D profile may be generated from a 2D cross-sectional model has been studied by Watts et al. (2005), such a solution has the potential to save much computer time in situations where many scenarios need to be modelled.

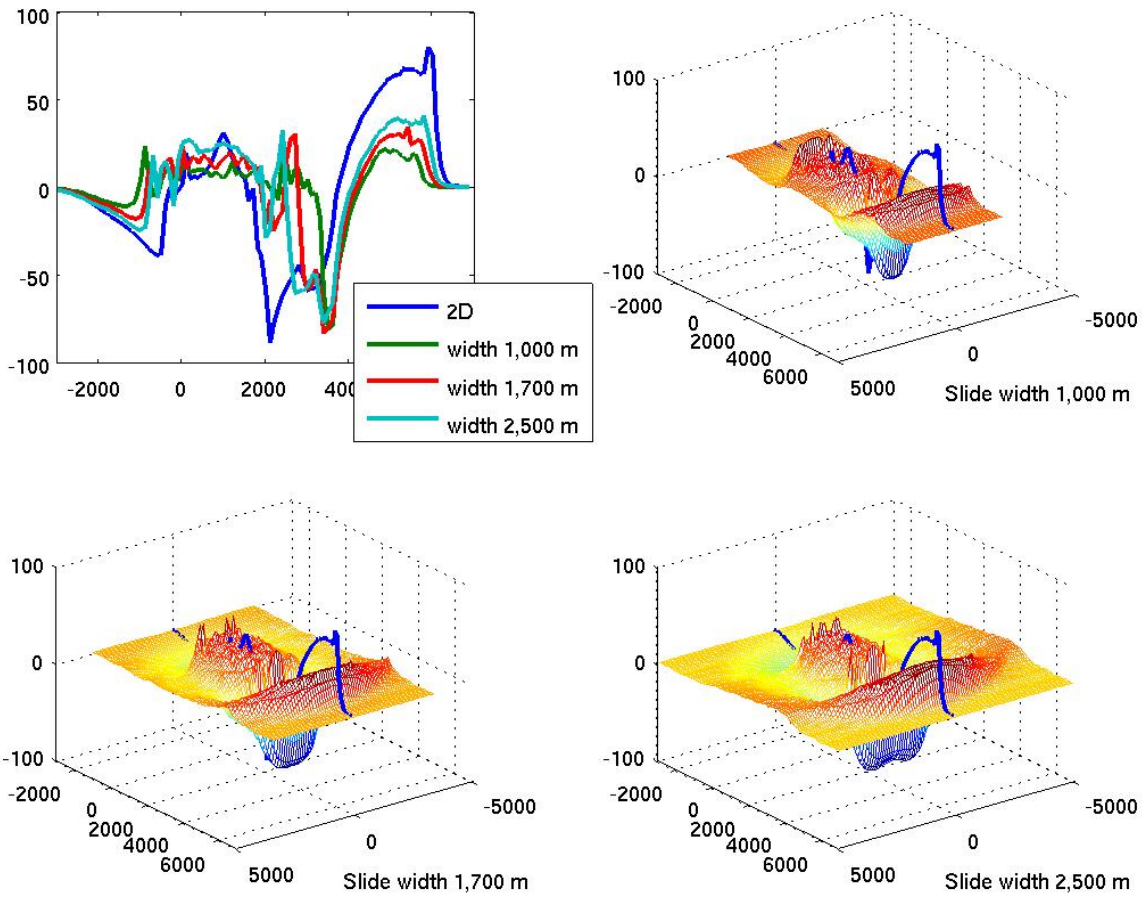

Figure 11: Comparing two-dimensional and three-dimensional modelling of tsunami generated by landslide in simplified bathymetry as given in Figure 7.2. All figures are taken at t = 100 s. Top left: vertical slices through y=0 for landslides with widths 1,000 m, 1,700 m and 2,500 m as well as two-dimensional vertical slice case. Top right: width = 1,000 m; bottom left: width = 1,700 m; bottom right: width = 2,500 m.

4.7 Cook Strait modelling scenario model

Maximum water levels produced from the Cook Strait tsunami propagation model initialised by the water level and velocity data produced from the 3D landslide model (see Section 3.4) are shown in Figure 12. We see that areas on the south coast of the North Island, close to the Wellington Harbour entrance, are estimated to experience tsunami waves with crests that approach or exceed 5m above the background water level in such a scenario.

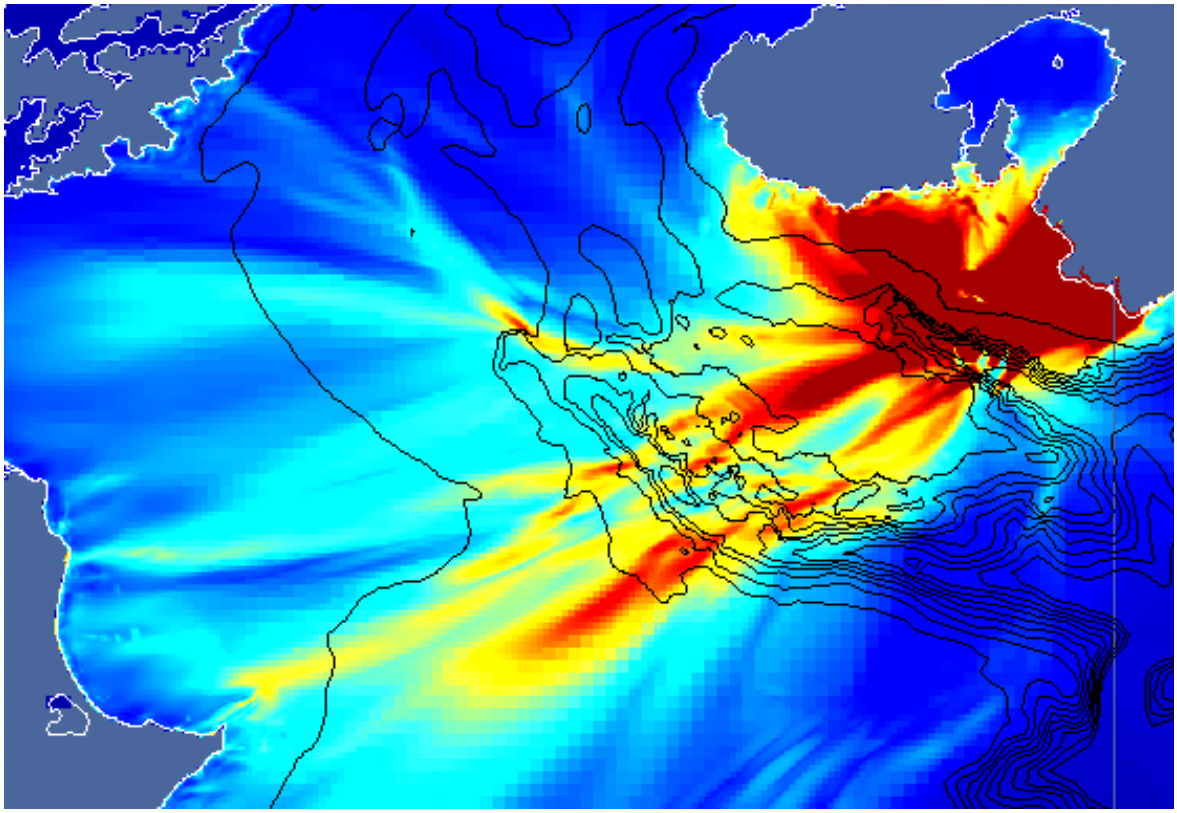

Figure 12. Maximum water levels (relative to background) in Cook Strait over the 3 hour period following the tsunami-initiating landslide in the Nicholson Canyon scenario. The colour scale ranges between 0 (dark blue) and 5 m (dark red).

These results demonstrate that there is a hazard to Wellington and the Cook Strait region in general from landslide-caused generated tsunami. While it is a long-term goal to incorporate landslide tsunami sources in a probabilistic hazard framework (See Section 5), it is useful at this time to place these events in context with other potential sources of tsunami in this region. Tsunamis of broadly similar size (~5m amplitude) may be caused by surface deformation alone during upper plate fault ruptures in the Cook Strait region, and larger tsunamis may be caused by earthquakes on the Hikurangi subduction interface, especially if such earthquakes rupture beneath Cook Strait (Cousins et al, 2007). Further, the modelled landslide was at the upper end of the volume distribution of observed

landslide scars, and was placed at the worst possible location. The infrequency with which such large landslides appear to occur, relative to the estimated frequency of earthquakes in this region (see e.g. Power, 2013), suggests that co-seismic deformation is probably the dominant contribution to tsunami hazard here.

5. DISCUSSION

5.1 Conceptual framework for building a landslide probability model

Any multi-source landslide-tsunami hazard model requires an underlying model of some form of magnitude frequency relationship defining when/how often landslides occur and their tsunami generating characteristics. A generalised magnitude frequency curve is shown in Figure 13. Landslides in submarine canyons likely occur from frequent very small events (sub resolution for ship-borne data collection) to infrequent events approaching cubic kilometre scale. The region of this curve that is of concern in terms of risk assessments however is limited to the central zone where landslides are large enough to generate hazardous tsunami, yet occur regularly enough to pose a risk. Defining the form of such a curve validated for a real world situation is a difficult task.

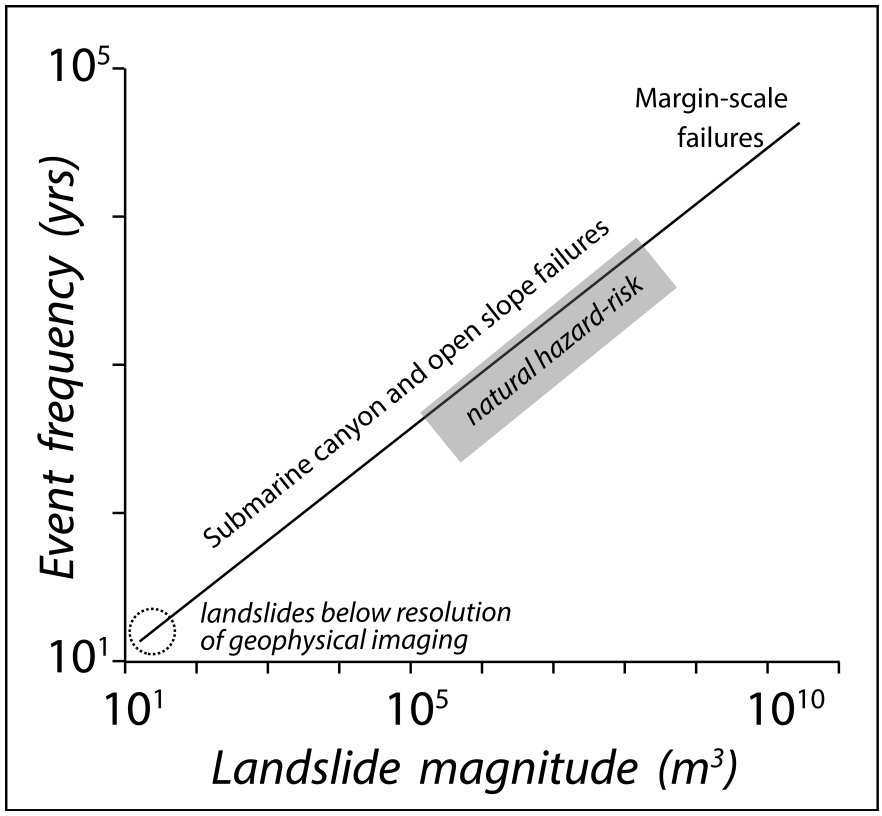

Figure 13: Conceptual magnitude frequency plot for landslide recurrence in continental margin settings.

We consider two approaches to defining magnitude frequency relationships for landslides in submarine canyon settings that could be used to underpin hazard and risk assessments.

5.2 Stability modelling approach – an assumption of earthquake triggering

In deep marine settings, and particularly those that also have an active tectonic setting, the majority of submarine landslides are inferred to be triggered by earthquakes (e.g. Sultan et al. 2004). While it is also acknowledged that many other processes influence slope stability, including: sediment loading, storm/wave loading, fluid/gas pressure/migration and slope erosion (Locat and Lee 2002). Many of these processes are factors that (pre) condition the slope for failure and do not necessarily trigger actual slope failure without additional external loading (e.g. a seismic load). The majority of submarine landslide studies, including those on passive and glaciated margins, invoke/infer earthquakes as the ultimate triggering mechanism in the absence of evidence for other specific mechanisms.

Based on this assumption it is possible to calculate the threshold level of earthquake shaking required to trigger failure and compare this against known return intervals for earthquake ground motion (e.g. Ten Brink et al 2009 Assessment of tsunami hazard to the U.S. East Coast Marine Geology 264A) (Strasser et al., 2007). This can be achieved via simple limit equilibrium calculations for slope stability, however the controlling parameters for such a model (e.g. mechanical strength, slip surface orientation) are not so easy to determine over large complex areas. Some approaches to this problem have been made, for example Ten Brink et al (2009) use a database of surface sediment samples correlated to mechanical parameters and infer vertical homogeneity. The authors acknowledge that this may not be applicable to areas such as submarine canyons where older consolidated rocks occur near or at the seafloor and exert a controlling influence on slope stability. In the submarine canyon case the problem is further complicated by the need to consider bedrock structure controls on slope failure, which is unlikely to be apparent from bathymetry alone.

In Cook Strait it is apparent that large landslides are controlled by bedrock orientation, in that they preferentially occur on bedding plane surfaces (Mountjoy et al., 2009). Given the lack of appropriate penetration and resolution subsurface imaging (multichannel seismic reflection data) it is very difficult to develop a regional model for failure orientation, bearing in mind that contrary to shallow rotational failures the seafloor gradient does not determine the failure plane gradient. As limit equilibrium models are very sensitive to failure plane gradient this is an important parameter. Based on the population of landslides it is possible to determine geometrical parameters for landslides (Figure 2), and these can be extrapolated to define the failure gradient over the extent of the study area given an appropriate population of landslides. Other key parameters such as failure depth may also be extrapolated from the landslide population.

The remaining key parameters that cannot be derived from the landslide population are the material properties. In all likelihood it will be necessary to infer properties based on studies of similar

rock and sediment from elsewhere. To accommodate the uncertainty inherent in this approach it is recommended that stability modelling is carried out via probabilistic (e.g. Monte Carlo) methods incorporating the appropriate range of values.

5.3 Landslide population approach – trigger independent

An alternative approach to this problem, that avoids the need to attain a thorough database of physical properties, is to develop an age model for observed landslides within a landscape. A regression of the landslide volume distribution presented in Figure 2 provides a magnitude distribution that determines the x-axis of the conceptual curve in Figure 12. While we do not have direct evidence for the age of more than four of these failures, the time period over which these landslides has occurred can be reasonably inferred. During sealevel lowstand periods the erosion and sediment deposition within most global canyon systems is enhanced, and this is expected to be the case for Cook Strait (Mountjoy et al., 2009). Thus we expect that the evidence for landslides observed in the canyons post-dates the start of sea-level rise, giving a maximum time period of 20,000 years. The dates presented in Table 2 do not contradict this. In fact it is possible that most landslides have occurred in the Holocene (post 10,000 years) and this may be a lower bound. This information can be used to develop a magnitude frequency curve of the form in Figure 12 that can be used to directly drive a landslide-tsunami hazard model. We do not present such a curve for Cook Strait as this study is meant as a general treatise on the generic issues associated with landslide-tsunami hazard assessments across submarine landslides rather than a specific case study. A magnitude frequency curve for submarine landslide occurrence may be used to directly control a probabilistic tsunami-hazard assessment. Alternatively it may be used to validate the results of a stability modelling based approach to assessing landslide recurrence.

Quantifying the likelihood of landslide occurrence in large submarine canyons is an inherently difficult problem. Although they are a first-order mechanism for the formation of the canyons, they are typically only identified by a scar in the canyon wall, with evidence for the deposit being removed. The concentration of currents and other erosion mechanisms means that the morphology of scars may be rapidly modified. Despite these difficulties, submarine canyons are one of the main mechanisms by which large and steep submarine slopes are able to come within close proximity of the land and human populations. This makes them very important in terms of natural hazards and demands that the issues and uncertainties associated with quantifying these hazards be overcome.

5.4 Effect of complex terrain on landslide-generated tsunami

A landslide into a canyon differs in the way it generates a tsunami compared to an equivalent landslide on an open slope. One difference is that the motion of the landslide body is suddenly decelerated, and rapidly brought to a halt or even reversed, by interaction with the slope of the

opposite canyon wall. Another difference is that tsunami waves generated by the landslide are themselves modified by the bathymetric features of the canyon – partial wave reflection may take place at the canyon walls, and the substantial differences in depth between the canyon floor and the surrounding continental shelf will affect the timing and refraction of the wave. Our results demonstrate that these influences can be significant, and that tsunami hazard assessments involving canyon systems will be more accurate if these effects are taken into consideration, rather than using methods that assume an open slope.

6. CONCLUSIONS

From the studies presented here we draw the following conclusions:

- Tsunami generation by submarine landslides in canyon systems is distinctly different to tsunami-generation by open coast landslides.
- Tsunami generation by submarine landslides in canyon systems is influenced by the sudden deceleration of the landslide at the bottom of the canyon, and this can lead to significantly larger waves in the opposite direction to the initial landslide motion.
- Tsunami-propagation within canyon systems is influenced by the bathymetry of the canyon which changes the wave speed, and hence causes refraction.
- The Cook Strait canyon system shows evidence for at least 130 landslides large enough to be mapped, and the majority of these are believed to have occurred in the Holocene (within the last 10,000 years).
- Landslides on the walls of the Cook Strait canyons predominantly occur in consolidated rock, rather than in accumulated sedimentary material as is typical of submarine landslides in depositional environments.
- Submarine landslides in the Cook Strait canyon system pose a risk to the city of Wellington in New Zealand, and it is likely that canyon systems elsewhere in the world pose similar risks to nearby coasts.

ACKNOWLEDGEMENTS

The authors would like to acknowledge helpful discussions with Christof Mueller and Phillip Barnes. This work was supported by the New Zealand Natural Hazards Platform (contract 2012-NIW-03-NHRP), and by GNS Science as part of its Government-funded, core research. This research was originally presented at the Tsunami Society 6th International Tsunami Symposium in Nicoya, Costa Rica.

REFERENCES

Argnani, A., Tinti, S., Zaniboni, F., Pagnoni, G., Armigliato, A., Panetta, D., and Tonini, R., 2011, The eastern slope of the southern Adriatic basin: a case study of submarine landslide characterization and tsunamigenic potential assessment: Marine Geophysical Research, v. 32, no. 1-2, p. 299-311.

Barnes, P. M., The southern end of the Wairarapa Fault and surrounding structures in Cook Strait, *in* Proceedings The 1855 Wairarapa Earthquake symposium, Wellington, 2005.

Berndt, C., Costa, S., Canals, M., Camerlenghi, A., de Mol, B., and Saunders, M., 2012, Repeated slope failure linked to fluid migration: The Ana submarine landslide complex, Eivissa Channel, Western Mediterranean Sea: Earth and Planetary Science Letters, v. 319, p. 65-74.

Bristeau, M.-O. and Coussin, B., 2001, Boundary conditions for the shallow water equations solved by kinetic schemes, Report RR-4282, INRIA Rocquencourt, Le Chesnay, France. Available online from http://www.inria.fr/rrrt/rr-4282.html.

Cousins, W. J., Power, W. L., Destegul, U. Z., & King, A. B., 2007, Combined Earthquake and Tsunami Losses for major earthquakes affecting the Wellington Region. GNS Science consultancy report, 280.

Dowrick, D. A., Strong ground shaking in the 1855 Wairarapa Earthquake, *in* Proceedings The 1855 Wairarapa Earthquake symposium, Wellington, 2005.

Fine, I. V., Rabinovich, A. B., Bornhold, B. D., Thomson, R. E., and Kulikov, E. A., 2005, The Grand Banks landslide-generated tsunami of November 18, 1929: preliminary analysis and numerical modeling: Marine Geology, v. 215, no. 1-2, p. 45-57.

Greene, H. G., Maher, N. M., and Paull, C. K., 2002, Physiography of the Monterey Bay National Marine Sanctuary and implications about continental margin development: Marine Geology, v. 181, no. 1-3, p. 55-82.

Grilli, S. T., Taylor, O. D. S., Baxter, C. D. P., and Maretzki, S., 2009, A probabilistic approach for determining submarine landslide tsunami hazard along the upper east coast of the United States: Marine Geology, v. 264, no. 1-2, p. 74-97.

Hampton, M. A., Lee, H. J., and Locat, J., 1996, Submarine Landslides: Reviews of Geophysics, v. 34, p. 33 - 59.

Iglesias, O., Lastras, G., Canals, M., Olabarrieta, M., Gonzalez, M., Aniel-Quiroga, I., Otero, L., Duran, R., Amblas, D., Casamor, J. L., Tahchi, E., Tinti, S., and De Mol, B., 2012, The BIG'95 Submarine Landslide-Generated Tsunami: A Numerical Simulation: Journal of Geology, v. 120, no. 1, p. 31-48.

Labbe, M., Donnadieu, C., Daubord, C., and Hebert, H., 2012, Refined numerical modeling of the 1979 tsunami in Nice (French Riviera): Comparison with coastal data: Journal of Geophysical Research-Earth Surface, v. 117.

Lastras, G., Canals, M., Urgeles, R., Amblas, D., Ivanov, M., Droz, L., Dennielou, B., Fabrés, J., Schoolmeester, T., Akhmetzhanov, A., Orange, D., and García-García, A., 2007, A walk down the Cap de Creus canyon, Northwestern Mediterranean Sea: Recent processes inferred from morphology and sediment bedforms: Marine Geology, v. 246, no. 2-4, p. 176-192.

Micallef, A., Mountjoy, J. J., Canals, M., and Lastras, G., 2012, Deep-Seated Bedrock Landslides and Submarine Canyon Evolution in an Active Tectonic Margin: Cook Strait, New Zealand, *in* Yamada, Y., Kawamura, K., Ikehara, K., Ogawa, Y., Urgeles, R., Mosher, D., Chaytor, J., and Strasser, M., eds., Submarine Mass Movements and Their Consequences, Volume 31, Springer Netherlands, p. 201-212.

Mountjoy, J. J., Barnes, P. M., and Pettinga, J. R., 2009, Morphostructure and evolution of submarine canyons across an active margin: Cook Strait sector of the Hikurangi Margin, New Zealand: Marine Geology, v. 260, no. 1-4, p. 45-68.

Mountjoy, J. J., Micallef, A., Stevens, C. L., and Stirling, M. W., 2013, Holocene sedimentary activity in a non-terrestrially coupled submarine canyon: Cook Strait Canyon system, New Zealand: Deep Sea Research Part II: Topical Studies in Oceanography, no. 0.

Pondard, N., and Barnes, P. M., 2010, Structure and paleoearthquake records of active submarine faults, Cook Strait, New Zealand: Implications for fault interactions, stress loading, and seismic hazard: Journal of Geophysical Research-Solid Earth, v. 115, p. B12320.

Popinet, S., 2003, Gerris: a tree-based adaptive solver for the incompressible Euler equations in complex geometries, J. Comput. Phys., 190, 572–600.

Power, W. L. (compiler), 2013, Review of Tsunami Hazard in New Zealand (2013 Update), GNS Science Consultancy Report 2013/131/ 222 p.

Rahiman, T. I. H., Pettinga, J. R., and Watts, P., 2007, The source mechanism and numerical modelling of the 1953 Suva tsunami, Fiji: Marine Geology, v. 237, no. 1-2, p. 55-70.

Stirling, M. W., McVerry, G., Gersenberger, M., Litchfield, N., Van Dissen, R., Berryman, K., Barnes, P. M., Wallace, L., Villamor, P., Langridge, R., Lamarche, G., Nodder, S., Reyners, M., Bradley, B., Rhoades, D., Smith, W., Nicol, A., Pettinga, J. R., Clark, K., and Jacobs, K., 2012, National seismic hazard model for New Zealand: 2010 update: Bulletin of the Seismological Society of America, v. 102, no. 4, p. 1514-1542.

Strasser, M., Stegmann, S., Bussmann, F., Anselmetti, F. S., Rick, B., and Kopf, A., 2007, Quantifying subaqueous slope stability during seismic shaking: Lake Lucerne as model for ocean margins: Marine Geology, v. 240, no. 1-4, p. 77-97.

Sue, L. P., Nokes, R. I., and Davidson, M. J., 2011, Tsunami generation by submarine landslides: comparison of physical and numerical models. Environmental fluid mechanics, 11(2), 133-165.

Tappin, D. R., Watts, P., and Grilli, S. T., 2008, The Papua New Guinea tsunami of 17 July 1998: anatomy of a catastrophic event: Natural Hazards and Earth System Sciences, v. 8, no. 2, p. 243-266.

Walters, R., Barnes, P., Lewis, K., and Goff, J. R., 2006, Locally generated tsunami along the Kaikoura coastal margin: Part 2. Submarine landslides: New Zealand journal of marine and freshwater research, v. 40, no. 1, p. 17-28.

Ward, S. N., 2001, Landslide tsunami: Journal of Geophysical Research-Solid Earth, v. 106, no. B6, p. 11201-11215.

Watts, P., Grilli, S. T., Kirby, J. T., Fryer, G. J., and Tappin, D. R., 1999, Landslide tsunami case studies using a Boussinesq model and a fully nonlinear tsunami generation model: Nat. Hazards Earth Syst. Sci., v. 3, no. 5, p. 391-402.

Watts, P., Grilli, S. T., Tappin, D. R. & Fryer, G. J., 2005, Tsunami generation by submarine mass failure. II: Predictive equations and case studies: Journal of Waterway, Port, Coastal and Ocean Engineering, v. 131, no. 6**,** p. 298-310.

ISSN 8755-6839

SCIENCE OF **TSUNAMI HAZARDS**

Journal of Tsunami Society International

Volume 35 **Number 3** **2016**

FEATURES AND PROBLEMS WITH HISTORICAL GREAT EARTHQUAKES AND TSUNAMIS IN THE MEDITERRANEAN SEA

[1] Lobkovsky L., [2] Mazova R., [2] Tyuntyaev S.,[2] Remizov I..

[1]P.P. Shirshov Institute of Oceanology, Russian Academy of Sciences, Moscow, Russia
[2]R.E.Alekseev Nizhny Novgorod State Technical University, Nizhny Novgorod, Russia

E-mail address:
llobkovsky@ocean.ru; raissamazova@yandex.ru; ser.tyuntyaev@gmail.com *i.v.remizov@yandex.ru*

ABSTRACT

The present study examines the historical earthquakes and tsunamis of 21 July 365 and of 9 February 1948 in the Eastern Mediterranean Sea. Numerical simulations were performed for the tsunamis generated by underwater seismic sources in frames of the keyboard model, as well as for their propagation in the Mediterranean Sea basin. Similarly examined were three different types of seismic sources at the same localization near the Island of Crete for the earthquake of 21 July 365, and of two different types of seismic sources for the earthquake of 9 February 1948 near the Island of Karpathos. For each scenario, the tsunami wave field characteristics from the earthquake source to coastal zones in Mediterranean Sea's basin were obtained and histograms were constructed showing the distribution of maximum tsunami wave heights, along a 5-m isobath. Comparison of tsunami wave characteristics for all the above mentioned scenarios, demonstrates that underwater earthquakes with magnitude M > 7 in the Eastern Mediterranean Sea basin, can generate waves with coastal runup up to 9 m.

KEYWORDS: Mediterranean Region, Great Historical Tsunamigenic Earthquakes, Seismic Source, Tsunami Generation, Tsunami Propagation, And Numerical Simulation

1. INTRODUCTION

The Mediterranean Sea region is characterized by high seismicity. The historical record indicates that potentially destructive tsunamis are possible and need to be further studied. The Eastern Mediterranean basin is particularly the most active (Pararas-Carayanis, 2001; Tinti et al, 2005; Papadopoulos et al., 2010). The eastern basin has significant sediment layers, which can reach up to 5-8 km in thickness (Papadopoulos et al., 2010)). Also, it has seismic arcs which are characteristic of transform zones – such as the Ionian Island Arc and the western and southern Crete Arc which extends to the Island of Rhodes, as well as deep sea trenches, such as the Hellenic deep sea trench with a depth of up to 5 km. The Hellenic Seismic Arc is one of the best known geological features of the Eastern Mediterranean and includes a deep-sea trench (Fig.1, red line) in its convex side (Hellenic trench), and an arc of underwater sediments, as well as a volcanic arc and a marginal sea (the Aegean Sea) in its concave side (Pararas-Carayanis, 2001; 2005; Papadopoulos et al., 2010).

Figure 1. Scheme of faults (red lines) in Mediterranean region.
The yellow arrows indicate direction of continental plate motion ((see, (EC, 2016)).

The seismic activity is high at shallow and moderate depths, and earthquakes that can reach magnitude of the order of M ~ 8 are possible. The motions of the continental plates (Fig.1) lead to an increase of stress in fault regions. Such interactions increase the potential of high tsunamicity, which gradually increases from the west to the east within the Mediterranean basin, particularly in the vicinity of Greece and the surrounding regions (Papazachos, B. C. 1996; Pararas-Carayanis, 2001; Papadopoulos et al., 2010; Pararas-Carayannis, Mader, 2011, EC, 2016).

Several significant earthquakes have occurred in regions of the Eastern Mediterranean Sea which generated local or regional destructive tsunamis in the past. Based on numerous historical documents, a great earthquake on 21 July 365 A.D. generated a devastating tsunami - now considered as the most catastrophic event in the Mediterranean Sea (Pararas-Carayanis, 2001; Tinti et al, 2005; Salamon et al., 2007; Shaw et al., 2008; Papadopoulos et al., 2010; Yolsal-Çevikbilen, Taymaz, 2012. Then, in February of 1948, another destructive tsunami struck the coasts of Karpathos Island. The main cause of such tsunamigenic earthquakes, results from the partial breaking of the African plate and its collision with the Eurasian plate (see Fig.1).

2. STATEMENT OF THE PROBLEM

2.1. Formation of tsunami source

Great earthquakes occur in zones of great faults in the Mediterranean basin, as shown in Fig.1. Many of the great underwater shallow earthquakes generate destructive tsunami. The tsunami generation mechanisms, the initial velocity and propagation of the waves and the terminal characteristics of inundation at a given coast (particularly in near-field zone) depend directly on the dynamic processes at the earthquake source (Lobkovsky, 1988; Lobkovsky et al., 2006). The present study describes the seismic processes of the earthquake source and the keyboard modelling of tsunamigenic earthquakes, where the vertical displacement of crustal blocks, is applied to determine the above listed parameters. (Lobkovsky, 1988)). The initial stress distribution in the seismic source essentially determines the character of crustal motions that generate a tsunami. The selection of a model for the seismic source is first of all determined by the spatial and temporal scales of corresponding wave motions in the basin (Lobkovsky, 1988; Lobkovsky et al., 2006). The present study addresses the numerical simulation of two historic catastrophic earthquakes in the Eastern Mediterranean: the earthquake of 21 July 365 A.D with possible magnitude M = 8.2 near the western the Island of Karpathos in the Aegean Sea.

Since the mechanisms of the seismic sources of both earthquakes are unknown, then, by taking the source mechanism from tectonic relationships (Lobkovsky et al., 2006)) and by using empirical formulas correlating earthquake magnitudes and displacement values along faults (Wells, Coppersmith, 1994), it is possible to compute approximately the size of the seismic source and the vertical components of seafloor displacement at the source. The estimate for the 365 A.D earthquake with a magnitude 8.2, had a source of 190 km in length and a width of nearly 40 km, while maximum displacement value is 9 m. For the 1948 tsunamigenic earthquake with magnitude M = 7.5, the source is 26 km in length, 26 km in width and with the crustal displacement estimated at 5 m.

For the 365 A.D. earthquake, three possible scenarios of were considered of crustal motions at the seismic source along the fault zone near the western region of the Island of Crete. (Figs. 2-4), (cf. with (Pararas-Carayanis, Mader, 2011))

SCENARIO 1: The seismic source being a single block, which can be moved up and down for given value with different velocities – the location of seismic source for this scenario is illustrated in Fig. 2 a,b.

SCENARIO 2: A two-block source divided along its length in two equal-in-width blocks, one of which is oriented to the Island of Crete (block 1) moving down, and a block 2 which begins to move up after the first block motion stops; the location of the seismic source for scenario 2 is illustrated in Fig. 3a, b.

SCENARIO 3: For the third scenario, the kinematic model of three-block keyboard source is considered, in which the source blocks move successively to different distance up and down at different times. The location of the seismic source for scenario 3 is presented in Fig.4 a,b.

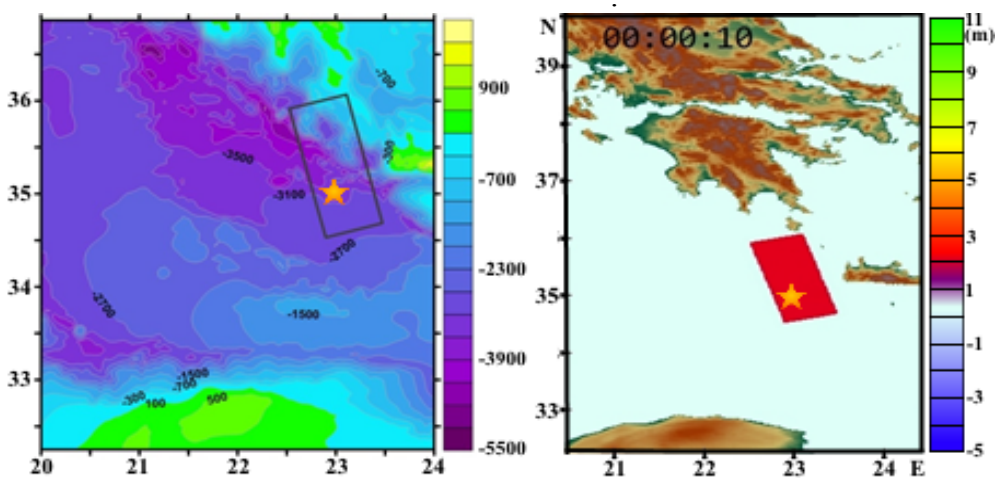

а) б)

Figure 2. Location of seismic source at earthquake of 365, SCENARIO 1
a) bathymetric map; b) topographic map.

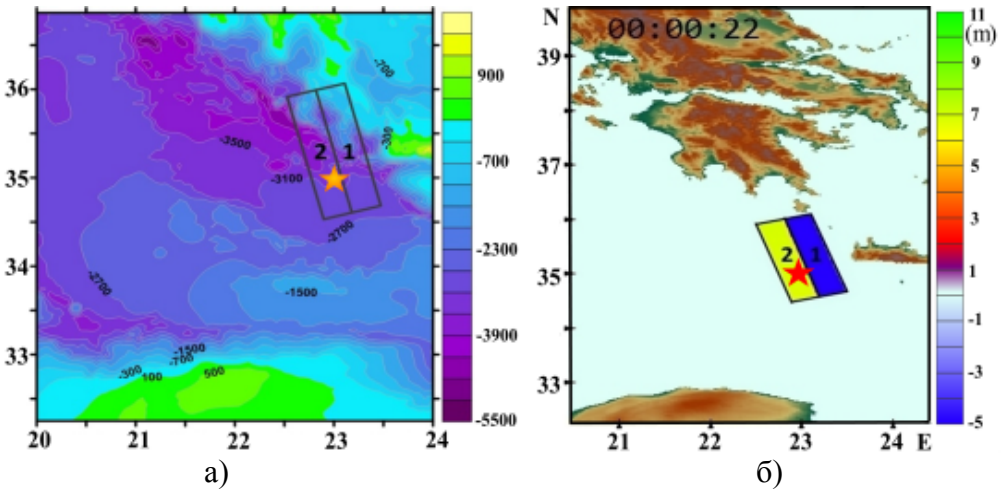

а) б)

Figure 3. Location of seismic source at earthquake of 365, SCENARIO 2
a) bathymetric map; b) topographic map.

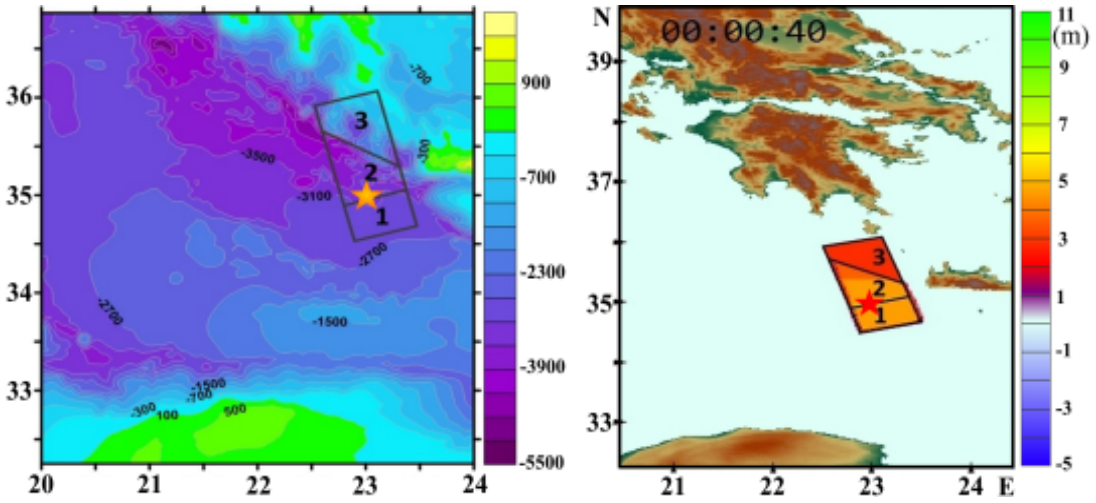

Figure 4. Location of seismic source at earthquake of 365, SCENARIO 3
a) bathymetric map; b) topographic map.

For the second tsunamigenic earthquake of 9 February 1948, two possible scenarios of earthquake source were examined: (see Fig.5, and Fig.6)

SCENARIO 4: The seismic source being a single block which can move up and down to given values with different velocities; The block motion of this source is presented in Table 1 and the location of the seismic source is represented by Fig. 5a, b.

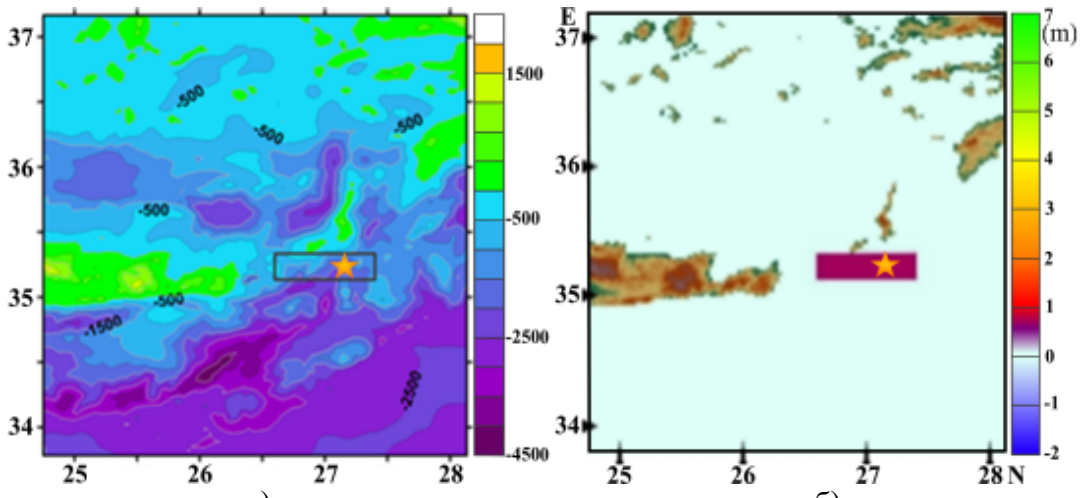

Figure 5. Location of seismic source at earthquake of 365, SCENARIO 3
a) bathymetric map; b) topographic map.

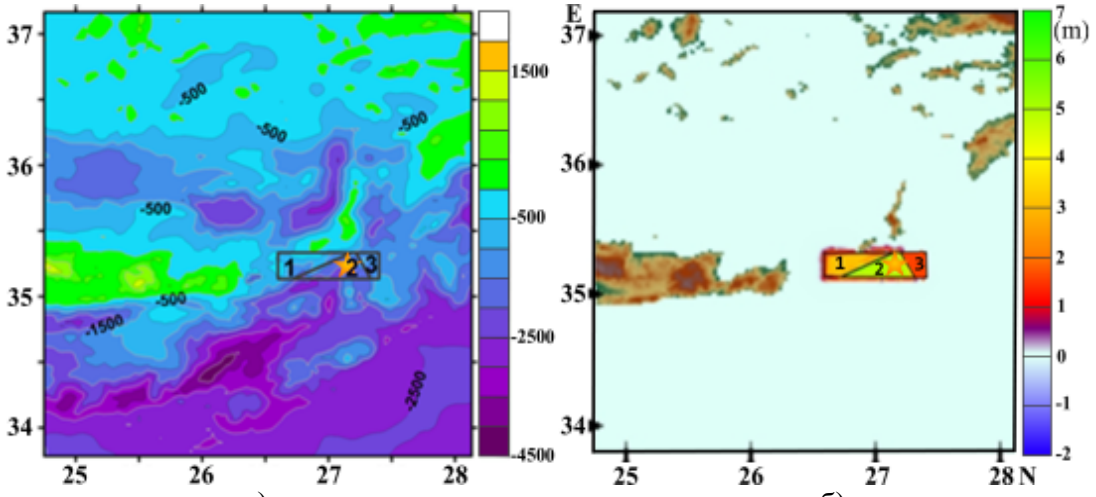

а) б)

Figure 6. Location of seismic source at earthquake of 365, SCENARIO 3
a) Bathymetric map; b) topographic map.

SCENARIO 5: For the fifth scenario the kinematics of a three-block keyboard model are considered, and the model blocks are being moved successively to different distance up and down for different length of time. The location of the seismic source for scenario 5 is presented in Fig.6a,b.

2.2. Mathematical statement of the problem

To describe the process of generation and propagation of tsunami waves in correspondence with above-mentioned assumptions, the nonlinear system of shallow water equations was used (Voltsinger et al., 1989; Lobkovsky et al., 2006)).

$$\begin{cases} \dfrac{\partial u}{\partial t} + u\dfrac{\partial u}{\partial x} + v\dfrac{\partial u}{\partial y} + g\dfrac{\partial \eta}{\partial x} = f_1 \\ \dfrac{\partial v}{\partial t} + u\dfrac{\partial v}{\partial x} + v\dfrac{\partial v}{\partial y} + g\dfrac{\partial \eta}{\partial y} = f_2 \\ \dfrac{\partial \eta}{\partial t} + \dfrac{\partial}{\partial x}[(\eta + H - \phi)u] + \dfrac{\partial}{\partial y}[(\eta + H - \phi)v] = \dfrac{\partial \phi}{\partial t} \end{cases}$$

where x, y are the spatial coordinates along Ox and Oy axes, respectively, t is the time, $u(x, y, t)$, $v(x, y, t)$ are the velocity components along Ox and Oy axes, $\eta(x,y,t)$ is the disturbance of free surface relative to its initial level, H is the depth of the basin, $\phi(x, y, t)$ is the function which describes bottom motion.

3. NUMERICAL SIMULATION OF HISTORICAL TSUNAMIS

3.1. Numerical simulation of the tsunami of 21 July 365

In this section - presented as examples – are the results of implementation of SCENARIO 1 . Fig. 4, illustrates the results of numerical simulation for tsunami wave front propagation for six (6) time moments. Fig.7.1, shows that the initial tsunami wave front already has reached points on Falaserna and Palaiochora at the west coast of the Island of Crete and the nearby islands. At 23 minutes travel time the initial wave front reaches the south side of the coast of Glyfada, on Attica , Greece(Fig.7.2).

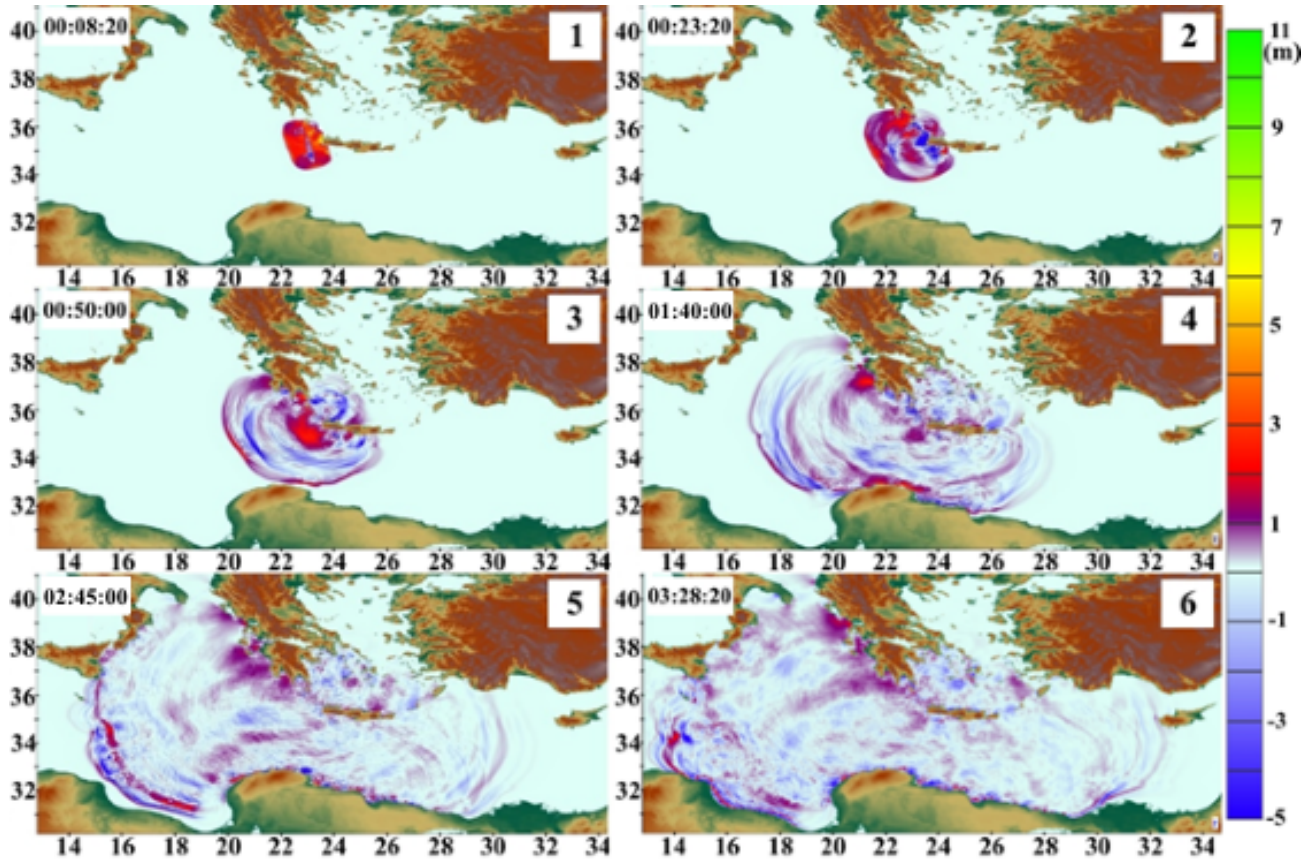

Figure 7. Propagation of the tsunami wave for scenario 1 for six time increments: 1 - 8 min 20 s; 2 - 23 min 20 s; 3 - 50 min; 4 - 1h 40 min; 5 - 2 h 45 min; 6 - 4h 30 min.

At the 50th minutes the first tsunami wave front reaches the African continent in the region of Point Derna of the coast of Libya (Fig.7.3). Further propagation of the tsunami wave front (for 1 h 40 min), strikes another Libyan coastal region of Benghazi and Turku cities, as well as the region of Katakola and Kalamata cities on the coast of Greece (Fig.7.4). After 2 h 45 min (Fig.7.5) the forefront of tsunami has already struck all three continents as well as the coast of Catania on the Island of Sicily (Fig.7.6).

Shown in Fig.8 are the computed distributions of maximum tsunami wave heights in the Eastern Mediterranen basin. As seen, the maximum wave heights occurred along the Greek coasts (maximum heights near the Island of Crete), the coasts of Italy, and near the northern and north-western coast of the African continent.

In more detail, the distribution of maximum wave heights along the coasts can be seen at the 3D-histograms of maximum wave heights, at the 5-m isobath (Fig.9). It can be seen that the coasts of Italy and the Island of Crete the wave heights reached 5-8 m. At the Island of Cyprus the mean wave heights were 2 m with 5 m peaks at some segments.

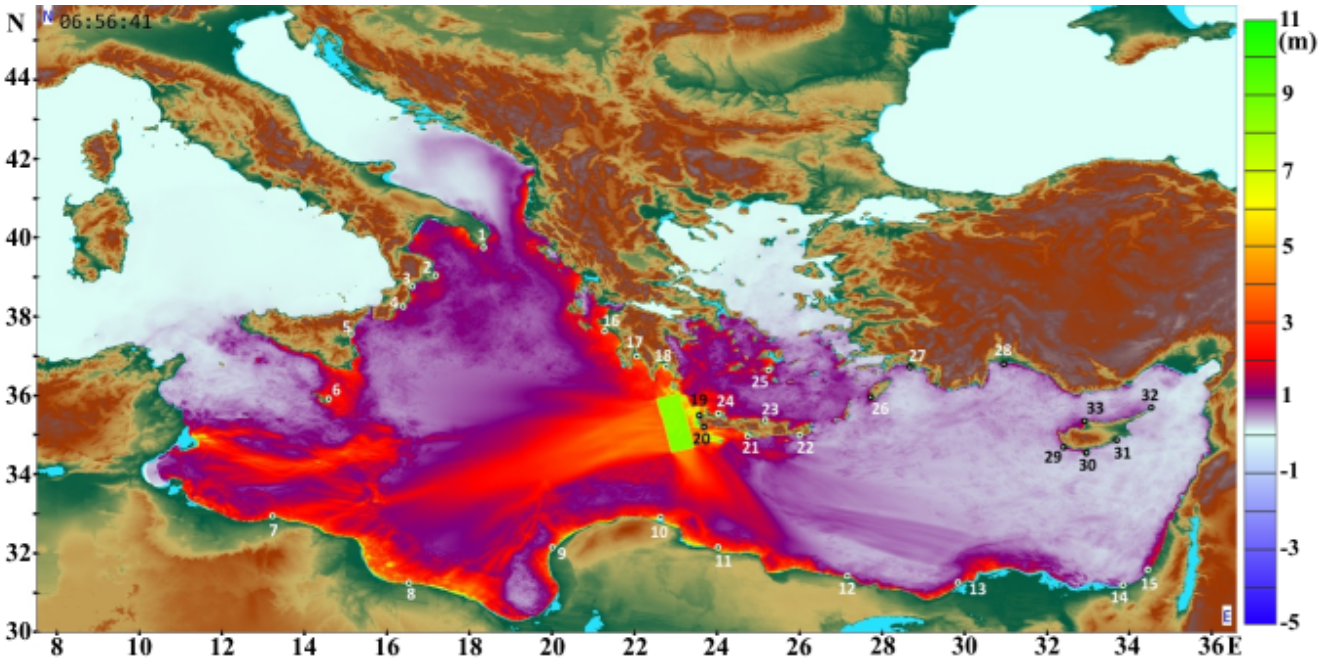

Figure 8. Distribution of maximum wave heights over the basin with implementation of scenario 1.

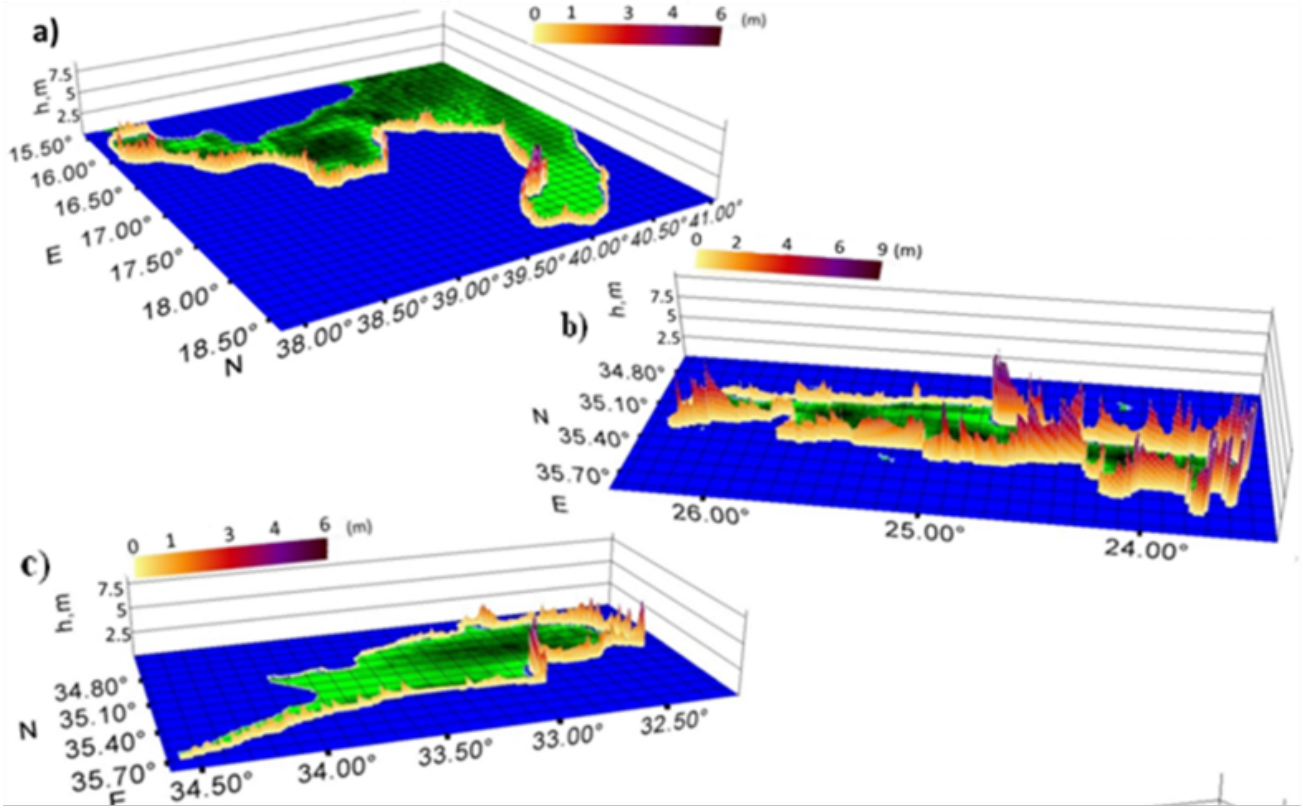

Figure.9. 3D-histograms for maximum wave heights at the 5-m isobath: a) Italy; b) Island of Crete; c) Island of Cyprus.

3.2. Results of the numerical simulation for scenario 3

For the realization of scenario 3 the keyboard model of seismic source is the same as for scenario 1 (Fig.4). Fig.10 illustrates tsunami wave generation for three (3) time increments and the location of the tsunami wave front for five (5) time icrements. The first 3 figures (Fig.10 (1-3)) illustrate this after tsunami generation.

Fig.10 (5) shows that the elevation of the wave coming to the Island of Crete and its directivity towards southern Greece. Figure 10 (6) shows the northern front striking the southern coast of Greece and heading for the City of Katakolo. The 50th minute wave has struck one half of the Island of Crete and other parts of Greece while the southern front of the wave is coming to Derna City. Subsequently the tsuanmi wave front is seen to propagate towards the coasts of the African continent. In three (3) hours the wave front is seen to have reached Sirt City in Libya, while the north-west front of the tsunami reaches the eastern coast of Italy, the north-east front begins to reach the coast of Turkey and finally the southern-eastern front of the wave begins to strike the City of Alexandria.

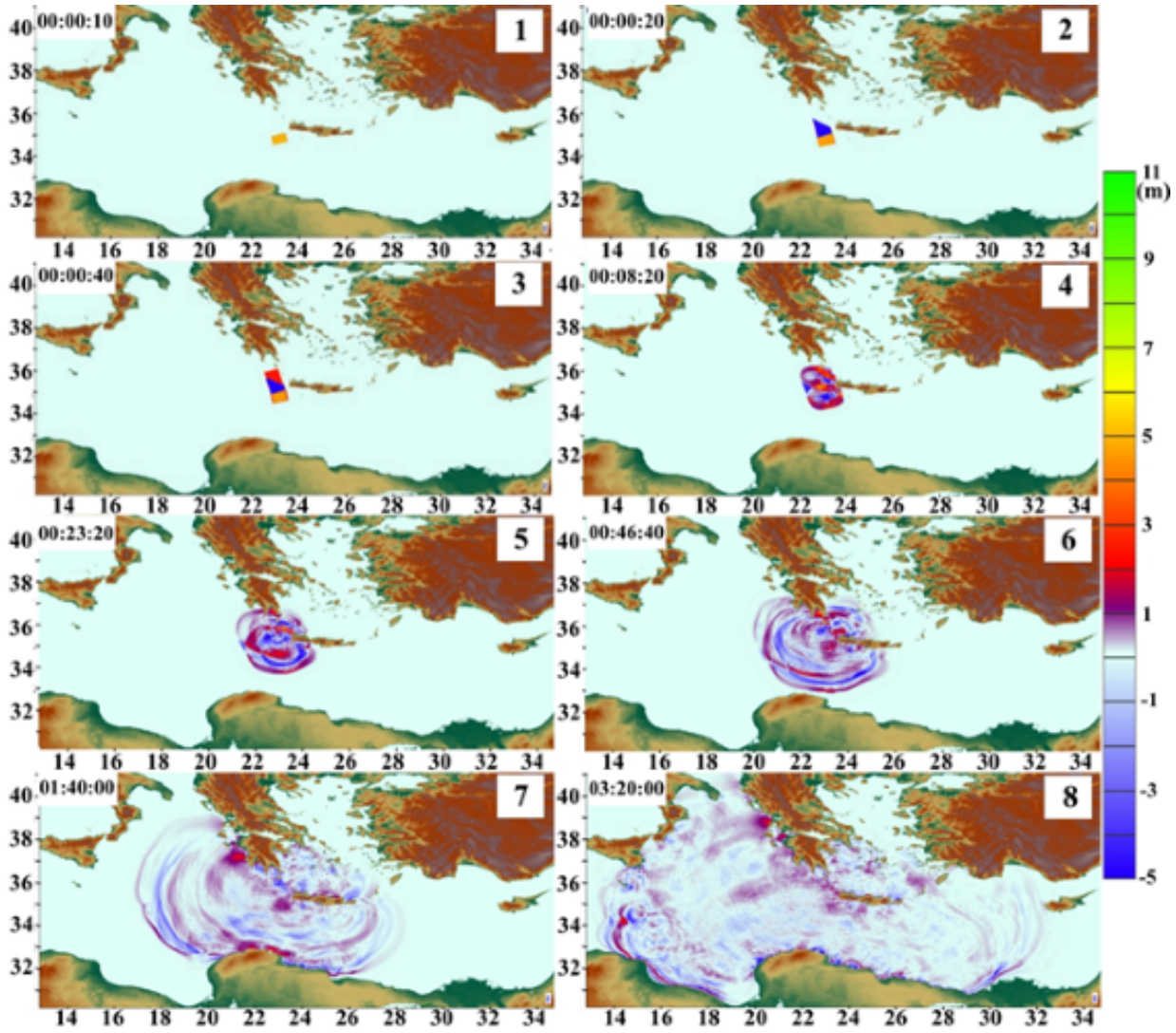

Figure 10. Numerical simulation of scenario 3: a) generation of tsunami source: 1) 10 sec, 2) 20 sec, 3) 40 sec; b) wave front localization: 4) 8 min 20 sec; 5) 23 min 20 sec; 6) 46 min 40 sec; 7) 1 hour 40 min; 8) 3 hours 20 min;

Fig.11 illustrates the computed distributions of maximum wave heights within the Eastern Mediteranean basin for the given scenarios. As seen the wave heights' distribution is close to the wave heights of the first and second scenarios but differently-oriented motion of blocks at the source significantly decreases wave height at the coast of Sicily coast and increases the height of waves at the coasts of Turkey. The more dangerous sections of tsunami wave heights concentrates mainly along the remains to be the coasts of Tunisia, Libya, Italy, Greece, Turkey, Egypt, Crete and Malta.

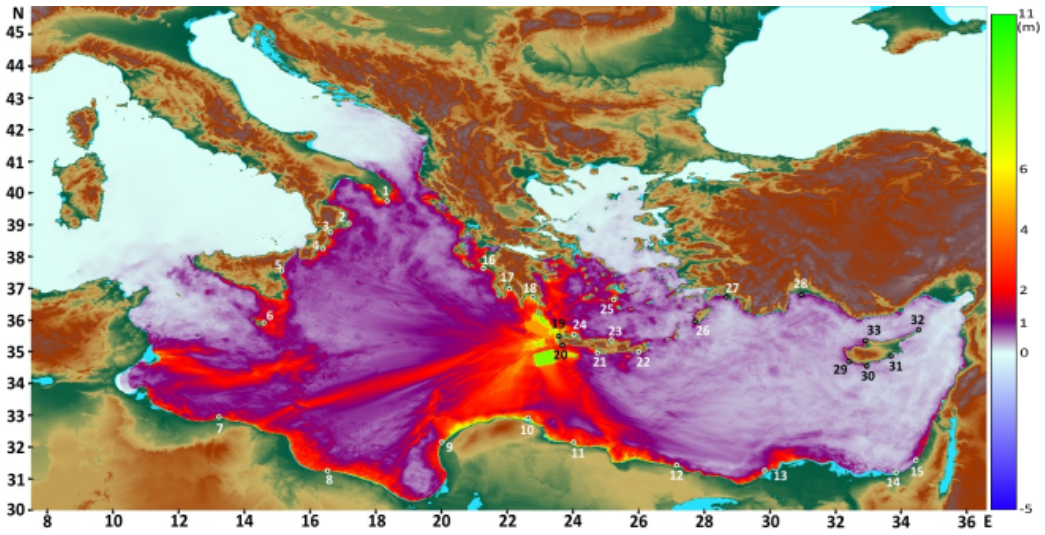

Figure 11. Maximum tsunami wave heights in Eastern Mediterranean basin for scenario 3.

Presented in Fig.12 are 3D histograms for the coasts of Libya, Tunisia and the eastern coasts of Mediterranean Sea: Israel, Lebanon, Syria. Apparently the wave height at eastern coast of Mediterranean Sea reached 4 m, and the at coasts of Libya and Tunisia up to 7m.

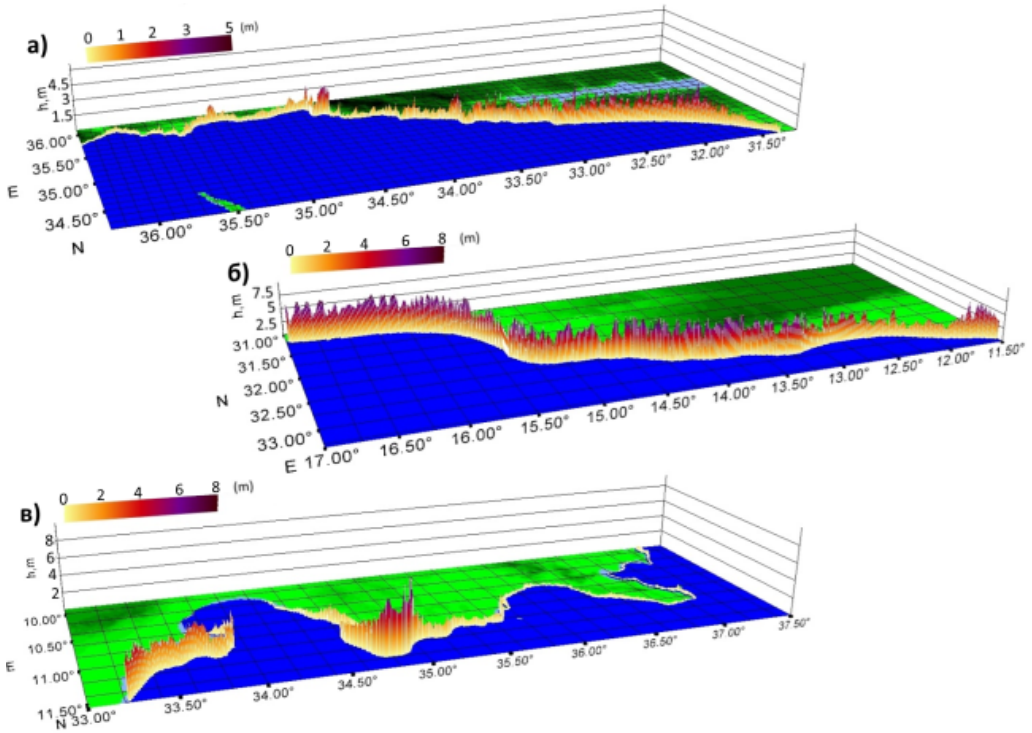

Figure 12. 3D histogram for maximum tsunami wave at 5 m isobath: a) eastern coast; b) Libya; c) Tunisia.

3.3. Numerical simulation of the tsunami of 9 February 1948

The results of implementation of SCENARIO 5 are presented in this section. It is well known that processes occurring at a seismic source (uplift or downfall), can be ultimately recalculated to estimates of vertical displacements. Presented in Fig.13 is an illustration of tsunami generation by displacements along a three-block seismic source. The process of formation of tsunami source can be seen with the uplift of the first crustal block on the seafloor, then at the downward motion of a second block and then by the subsequent uplift of a third block to the same height as the first.

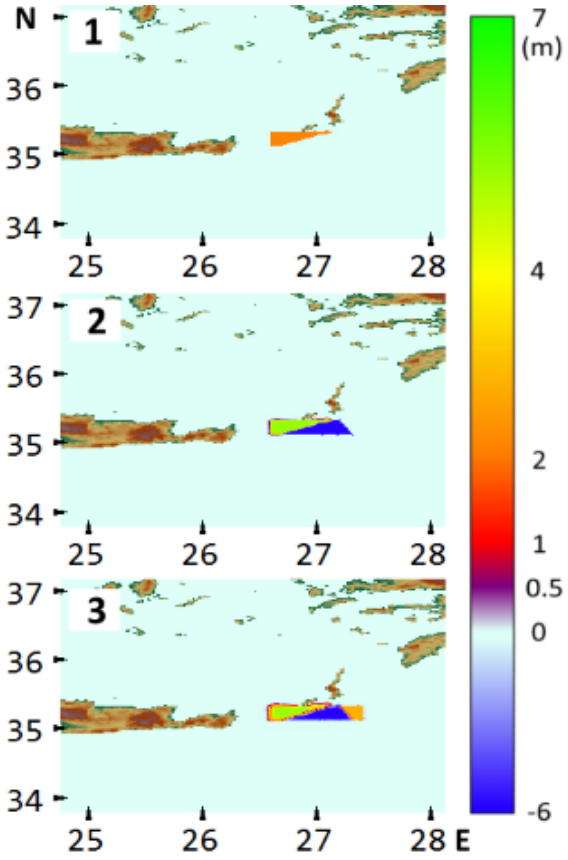

Figure 13. Generation of tsunami source with the realization of scenario 5: 1) 5 s; 2) 14 s; 3) 25 s.

Illustrated by Fig.14, is the propagation of tsunami waves on the basin for six (6) time icrements. In the first time increment (Fig.14 (1), the wave is seen to strike the Island of Karpathos as well as the western coast of the Island of Crete. Subsequently, in 21 min (Fig.14 (2)), the leading tsunami wave reaches the Greek Island of Rhodes. At further propagation (55 min, middle panel, Fig.14 (3)) the wave's north-eastern front has already reached the Island of Rhodes and stikes the south-eastern cities of Dalyan and Marmaris inTurkey.

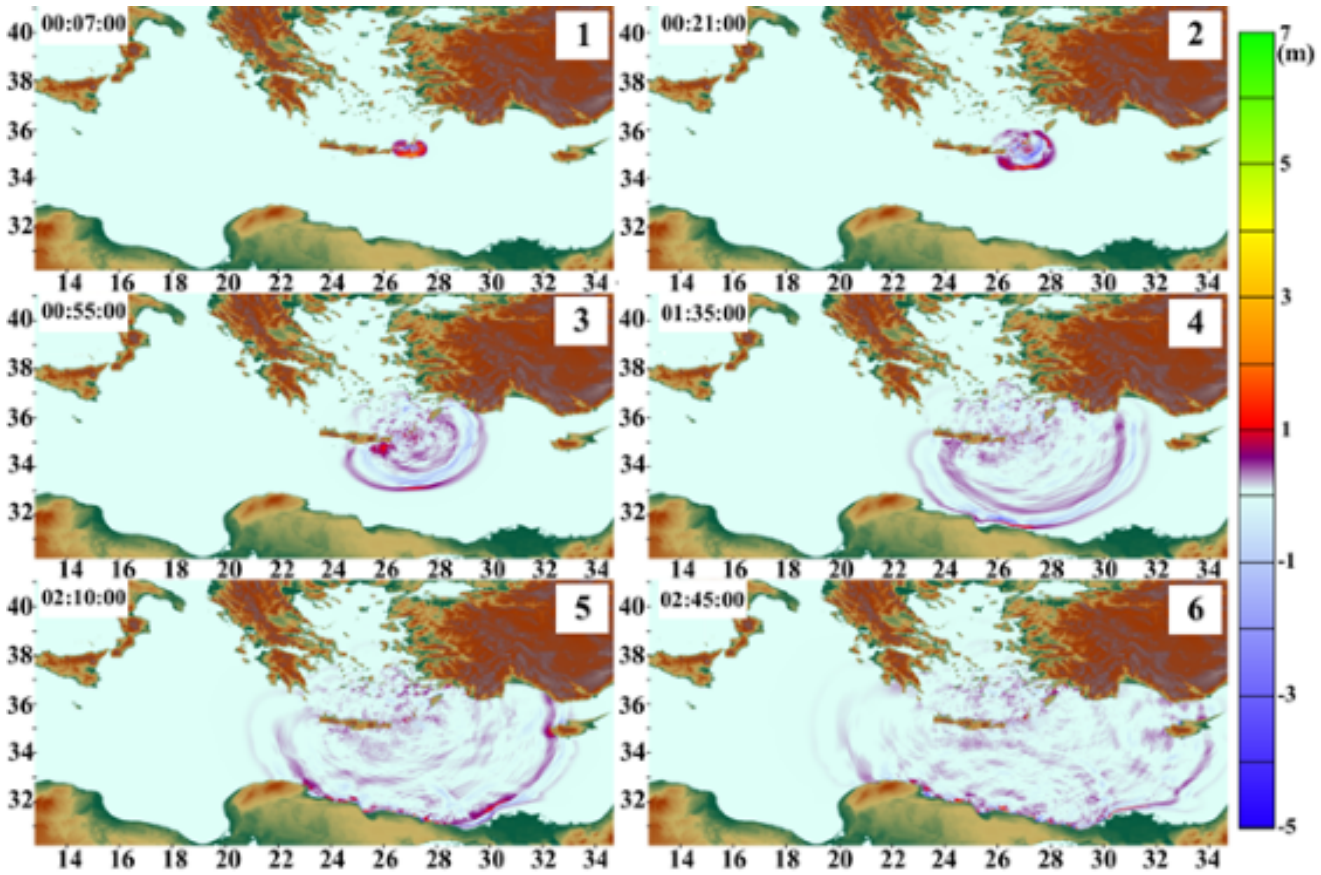

Figure 14. Numerical simulation of scenario 4: a) generation of tsunami source: 1) 7 sec, 2) 21 sec, 3) 55 min, 4) 1 hour 35 min, 5) 2 hour 10 min, 6) 2 hour 45 min.

In 1 hour and 35 min (middle panel, Fig.14 (4)), the wave has already reached the Island of Crete, its southern front has already reached the coast of Mersa-Matruh and begins to arrive at the east of Libya. In 2 hour and 10 min (lower panel, Fig.14 (5)) the eastern front actively strikes part of the Island of Crete and the southern coast of Turkey in the region of Alanya City. At the lower panel, (2 hour 45 min, Fig.14 (6)) the southern front has already reached a large part of the coast of Egypt, while the north-western front has reached the south coasts of Greece.

Presented in Fig.15, is the distribution of maximum wave heights in the entire basin of the Eastern Mediterranean Sea. From the distribution of maximum wave heights for the fifth scenario it is well seen that most affected are the near-field segments of the coasts of Libya, Egypt, Turkey, and of the Islands of Crete and Cyprus.

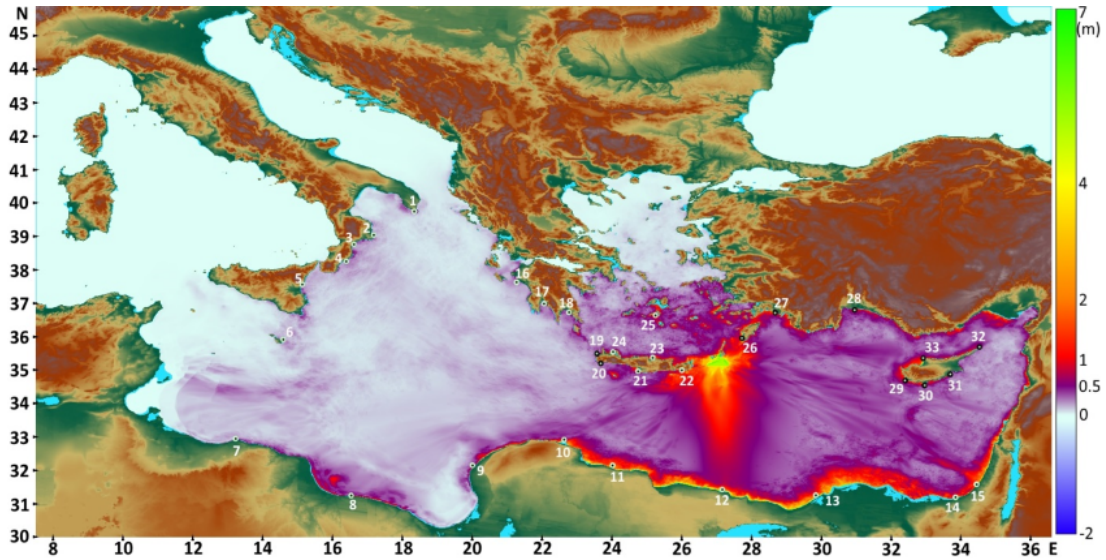

Figure 15. Maximum tsunami wave heights on the Eastern Mediterranean basin at the realization of scenario 5.

Fig.16 shows the 3D-histograms for maximal wave heights at 5-m isobath for the coasts of Turkey, the Island of Crete, and Israel, Lebanon and Syria.

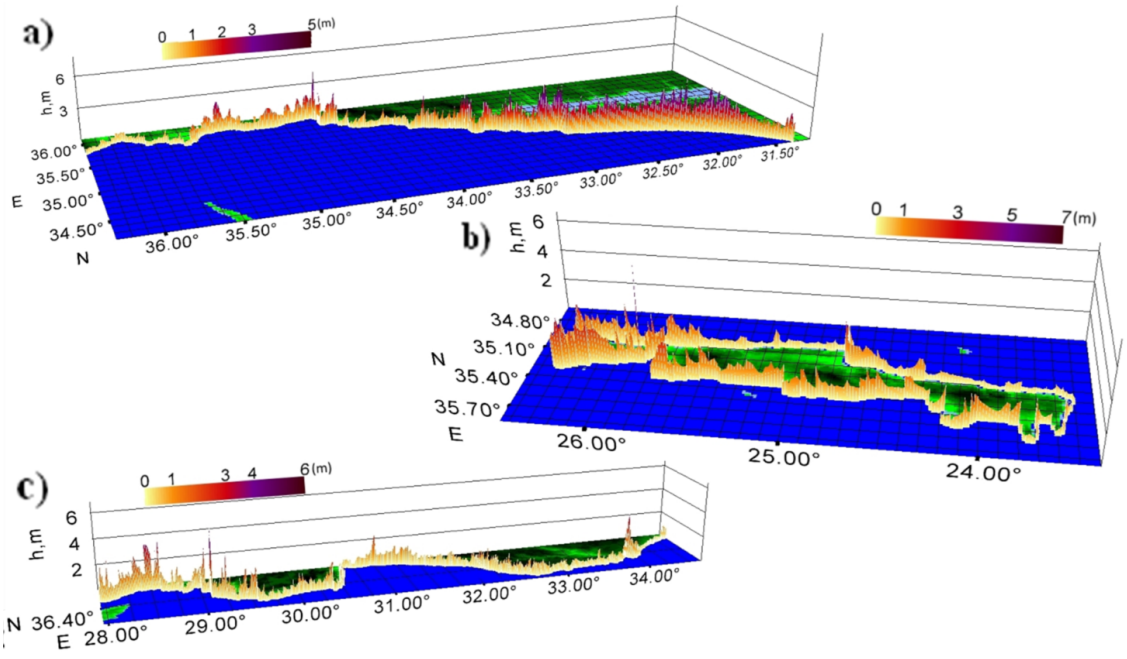

Figure 16. 3D-histograms for maximum wave heights at 5-m isobath for the coasts of: a) theeast coast of Mediterranean Sea; b) Crete island; c) Turkey.

4. COMPARISON OF MAXIMUM WAVE HEIGHTS FOR EARTHQUAKE AND TSUNAMI OF 21 JULY 365 AND 9 FEBRUARY 1948

4.1. Comparison of maximum wave heights for earthquake and tsunami of 21 July 365

Fig.17 shows histograms of maximum wave heights for the coast of the Island of Crete. As it can be seen, at the west of the southern coast, the maximum wave height of 7.6 m is reached with the first and second (single block and two-block source, respectively) scenarios. For the third scenario (three-

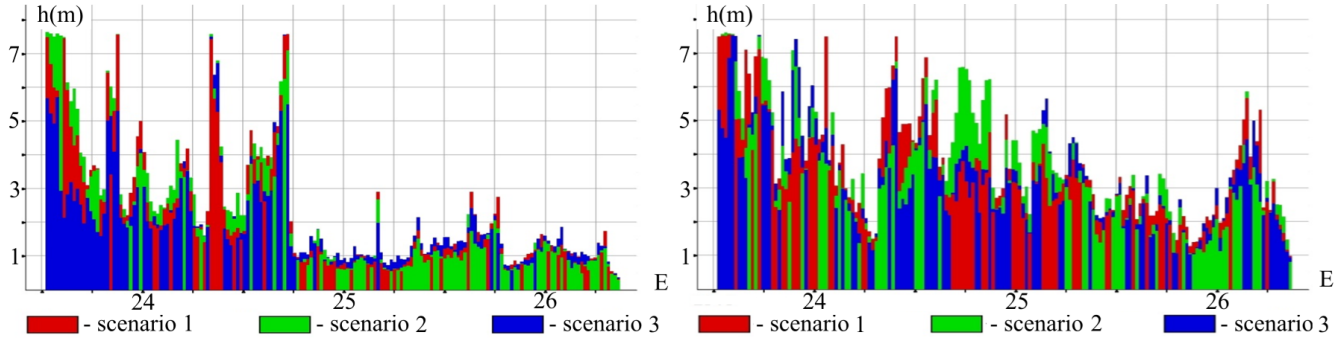

Figure 17. Histograms of maximum tsunami wave heights for the Island of Crete: a) southern coast; b) eastern coast.

block source) the maximum wave height is 6.5 m, while mean values of the tsunami wave height are near 2.8 m. Fig.18 illustrates histograms for the coast of Sicily. It can be seen that maximum tsunami wave heights to 5.5 m are reached with the realization of scenario 2. However, at the eastern coast of the Island of Sicily, the maximum wave height to 6.5 m is reached with the realization of scenario 3.

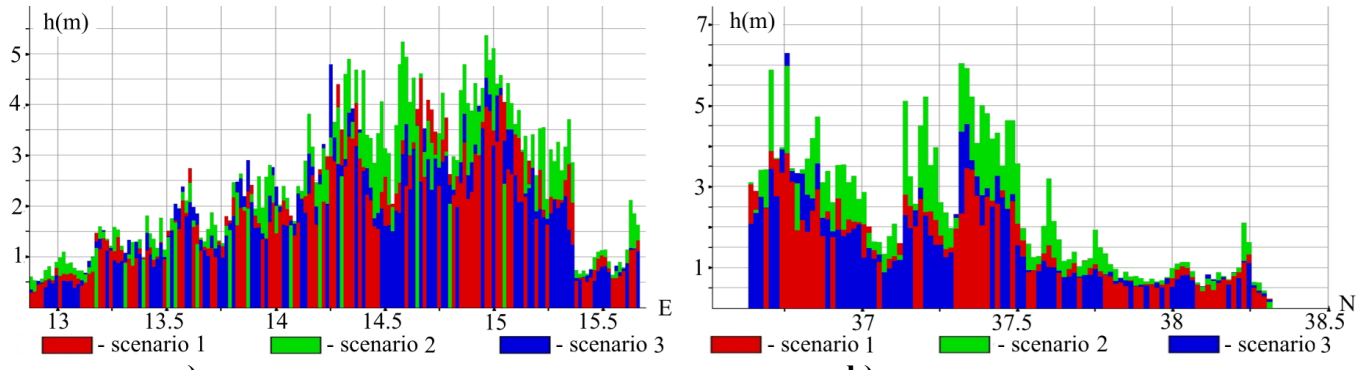

Figure 18. Histograms of maximum tsunami wave heights for the Island of Sicily: a) south-eastern coast; b) eastern coast.

Fig.19a shows a histogram of maximum wave heights for the Turkish coast. It is well seen that with the realization of all scenarios, the maximum wave heights in the the west reaches 2,75 m but at eastern side the maximum wave heights are reached with the realization of scenario 1.

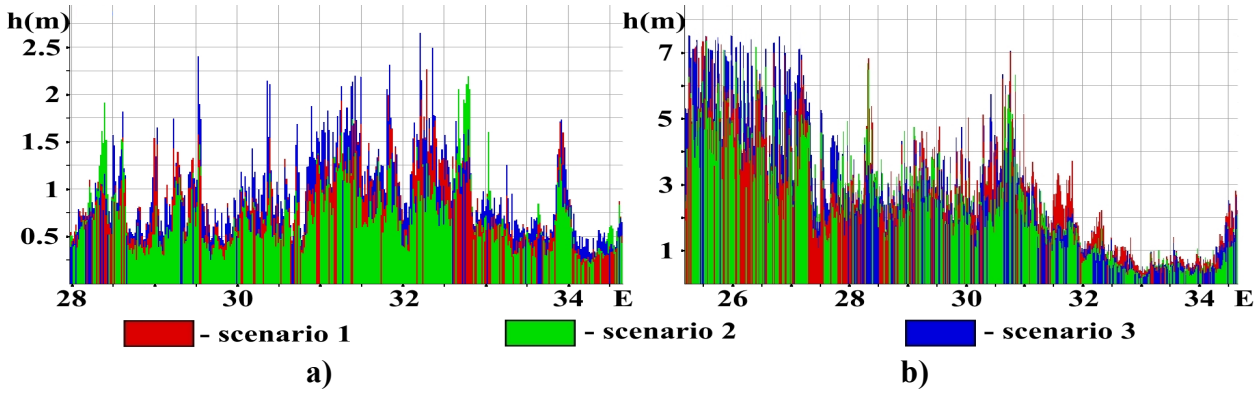

Figure 19. Histograms of maximum tsunami wave heights for the Turkish coast (a) and for the coast of Egypt (b).

Fig.19b ahows the histograms of maximum wave heights on the coast of Egypt. It can be seen that the maximum wave height of 7.2 m is reached with the realization of scenario 3.Table 5 shows the data from virtual tide gauges, namely maximum wave height, as well a depression of water level and time of arrival for scenarios 1-3.

4.2. Comparison of maximum wave heights for earthquake and tsunami 9 February 1948

Fig. 20 shows the histograms of maximum tsunami wave heights for the coast of Italy for cases when seismic source is a single block (scenario 4) and for a three-block keyboard source (scenario 5). Maximum wave heights for both scenarios are reached to 0.6 m.

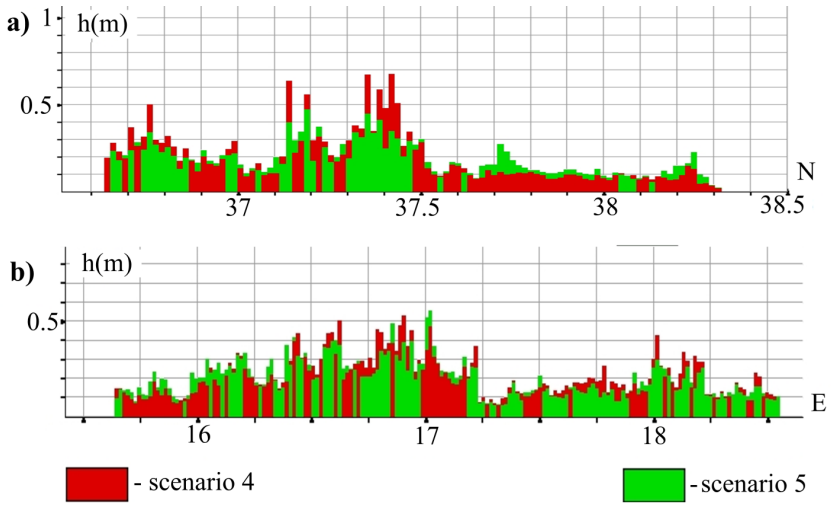

Figure 20. Histograms of maximum tsunami wave heights for the coast of Italy coast: a) eastern coast; b) southern coast.

Fig. 21 shows the histograms of maximum tsunami wave heights for the coast of the Island of Crete. A maximum wave height of 4 m is reached with the realization of scenario 4. For scenario 5 the maximum wave height id 3.5 m.

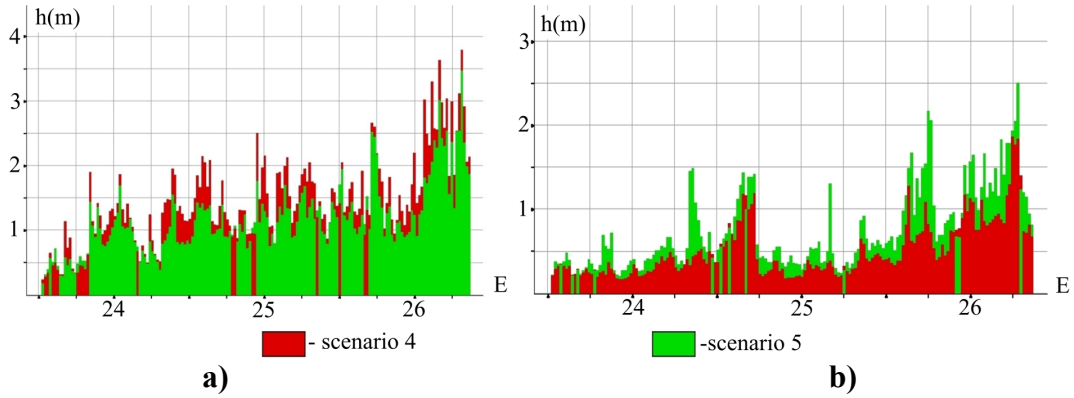

Figure 21. Histograms of maximum tsunami wave heights for the Island of Crete: a) southern coast; b) eastern coast.

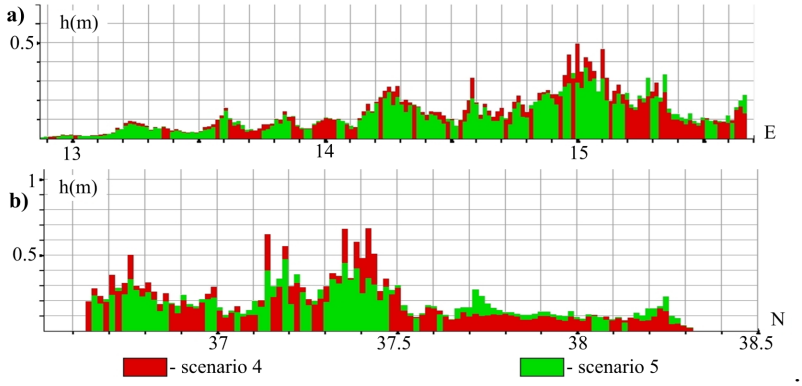

Figure 22. Histograms of maximum tsunami wave heights for the Island of Sicily: a) southern coast; b) eastern coast.

Fig. 22a shows the histograms of maximum wave heights for the southern coast of the Island of Sicily for two scenarios. Maximum wave height for both scenarios reaches 0.5 m. Fig. 22b shows histograms of maximum wave heights for the eastern coast of Sicily. A maximum wave height of 0.7 m is reached with the realization of scenario 4. However, the mean wave height near the coast for both scenarios is not essentially different.

Fig. 23a shows histograms of maximum wave heights for the coast of Turkey. Maximum wave height reaches 3.8 m, however, the mean values along the coast do not exceed 1.5 m. Fig. 23b is a histogram of maximum tsunami wave height for the coast of Egypt. It is well seen that with the realization of scenario 4 the wave heights reach 10 m while for scenario 5 their heights range between 5 and 8 m. With the realization of scenario 4, the mean wave height is essentially larger than with the realization of scenario 5.

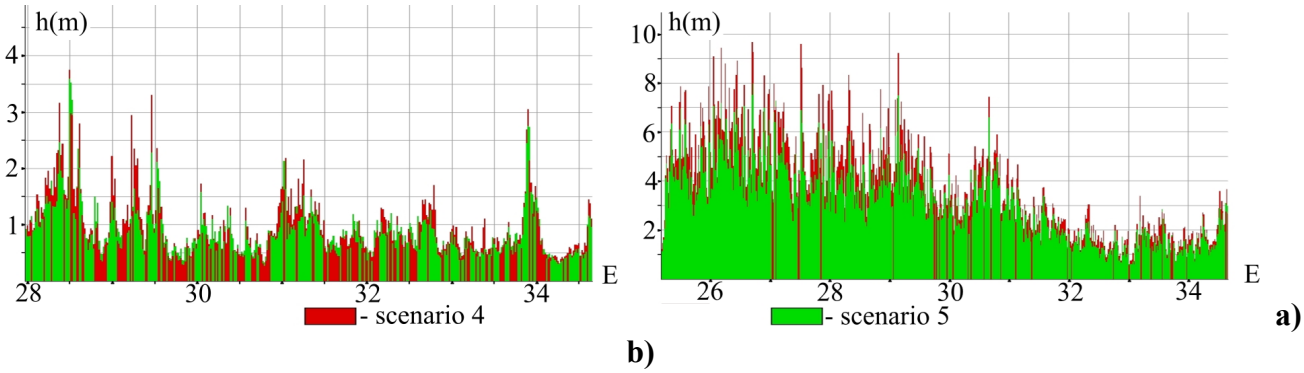

Figure 23. Histograms of maximum tsunami wave heights for the Turkish coast (a) and for the coast of Egypt (b).

The numerical simulation and analysis of maximum wave heights of the historical tsunamis of 345A.D. and 1948 A.D. for selected 33 points of the Eastern Mediterranean basin, with the given earthquake magnitude but with different realization of initial conditions (see Tables 1 and 2), gives far-field values independently of the dynamics of the seismic source. But for the near-field zones the values essentially depend on the crustal displacement processes at the source of the earthquake.

Table 1. shows the data of maximum high and low values of 33 virtual tide gauges (see Figures 8,11,15) at the 5-meter isobath, for SCENARIOS 1-5.

Table 1

№	Settlement/inhabited locality	Maximum ampltitudes at the 5-meter isobath (m)					The largest decrease in the water level of 5-meter isobath (m)				
		Scenario №									
		1	2	3	4	5	1	2	3	4	5
1	c. Leuca	3,79	3,67	2,57	0,18	0,19	3,55	3,52	3,01	0,11	0,11
2	c. Crotone	3,33	3,90	2,40	0,15	0,14	3,21	3,85	2,59	0,18	0,15
3	c.Catandzaro	2,21	2,19	1,59	0,09	0,11	1,90	1,85	1,44	0,12	0,11
4	c.RoccellaIonica	3,27	4,29	2,74	0,88	0,48	4,09	4,17	3,15	0,69	0,58
5	c. Catania	2,32	4,62	1,87	0,34	0,29	3,50	4,10	3,12	0,20	0,26
6	c. Valletta	3,46	4,13	2,22	0,11	0,11	3,05	3,97	2,72	0,14	0,13
7	c. Tripoli	3,26	4,95	3,18	0,13	0,09	4,30	5,59	3,92	0,14	0,13
8	c. Sirt	4,27	4,62	4,82	0,27	0,25	3,75	6,77	3,28	0,26	0,21
9	c. Benghazi	3,64	5,19	2,71	1,19	1,06	3,17	3,45	2,78	1,16	0,92
10	c. Derna	4,32	5,10	4,04	0,65	0,69	5,09	5,71	3,98	0,65	0,51
11	c. Tobruk	5,07	3,21	4,56	1,44	1,29	3,69	3,07	3,47	1,72	1,55
12	s. MersaMatruh	3,02	3,93	3,27	5,77	5,25	2,66	2,93	2,78	3,69	3,62
13	c. Alexandria	2,43	2,27	1,92	1,97	1,90	2,82	2,82	2,44	1,80	1,74
14	c. Al-Arish	0,72	0,58	0,73	0,79	0,88	0,70	0,46	0,62	1,08	0,93

15	**c. Gaza**	**1,27**	**1,23**	**1,18**	**1,11**	**1,00**	**1,06**	**1,15**	**0,98**	**1,15**	**0,83**
16	**c. Katakolo**	**3,62**	**3,45**	**3,76**	**0,33**	**0,30**	**4,02**	**3,75**	**3,59**	**0,41**	**0,30**
17	**c. Kalamata**	**6,49**	**5,68**	**3,96**	**0,66**	**0,36**	**6,93**	**4,98**	**5,27**	**0,73**	**0,57**
18	**c. Glyfada**	**6,85**	**6,38**	**6,82**	**0,46**	**0,42**	**6,52**	**6,82**	**8,49**	**0,54**	**0,47**
19	**c. Phalasarna**	**6,94**	**6,09**	**6,99**	**0,29**	**0,28**	**6,98**	**7,96**	**6,56**	**0,31**	**0,29**
20	**c. Palaiochora**	**6,98**	**6,69**	**6,74**	**0,61**	**0,50**	**5,84**	**6,23**	**5,90**	**0,49**	**0,42**
21	**v. Matala**	**5,62**	**5,06**	**6,98**	**1,21**	**1,35**	**6,17**	**5,38**	**5,40**	**1,52**	**1,54**
22	**c. MakryGialos**	**6,66**	**6,40**	**7,08**	**1,80**	**1,57**	**3,94**	**5,15**	**3,23**	**1,58**	**1,34**
23	**c. Heraklion**	**3,58**	**3,07**	**2,82**	**0,82**	**0,81**	**2,29**	**3,15**	**2,15**	**0,81**	**0,74**
24	**c. Chania**	**4,32**	**4,08**	**3,62**	**1,12**	**0,73**	**4,52**	**9,42**	**4,07**	**1,33**	**1,01**
25	**i. Ios**	**2,61**	**2,67**	**2,58**	**0,81**	**0,65**	**2,79**	**2,85**	**3,09**	**0,80**	**0,58**
26	**c. Prasonisi**	**3,16**	**2,81**	**2,34**	**3,16**	**2,87**	**3,01**	**3,52**	**1,92**	**2,71**	**2,59**
27	**b.Iztuzu**	**2,75**	**3,61**	**3,09**	**2,00**	**1,82**	**3,73**	**4,34**	**4,69**	**2,74**	**2,53**
28	**c. Belek**	**2,02**	**3,78**	**3,80**	**2,64**	**2,09**	**2,70**	**3,47**	**5,50**	**2,47**	**2,07**
29	**c.Paphos**	**2,53**	**1,46**	**2,08**	**1,30**	**1,09**	**2,36**	**2,07**	**2,01**	**1,14**	**1,17**
30	**b. Akrotiri**	**2,47**	**1,91**	**2,70**	**1,89**	**1,62**	**1,38**	**2,25**	**2,18**	**1,56**	**1,22**
31	**c. Larnaca**	**0,65**	**0,38**	**0,54**	**0,35**	**0,33**	**0,62**	**0,41**	**0,48**	**0,35**	**0,34**
32	**p.Karpass**	**0,37**	**0,29**	**0,32**	**0,21**	**0,23**	**0,52**	**0,39**	**0,45**	**0,24**	**0,18**
33	**v. Livera**	**2,21**	**2,90**	**1,91**	**2,10**	**1,49**	**1,94**	**4,03**	**1,92**	**2,31**	**1,37**

5. DISCUSSION AND CONCLUSION

The above obtained results for potential tsunami waves generated by great earthquakes in the Mediterranean Sea, demonstrate that detailed tsunami characteristics can be essentially determined by location of seismic source and analyzing the complexity of crustal displacement processes. Use of the key-board model for such tsunamigenic earthquakes permits to take into account such complexities. The present data on generation and propagation of tsunami waves at realization of the three listed scenarios are consistent with the results of numerical simulation of the 365 A.D. event with another model of the seismic source (Pararas-Carayannis, Mader, 2011). So, as it follows from both models the western part of Mediterranean Sea is not affected (Pelinovsky et al., 2002)) while in the Eastern Mediterranean larger tsunamis can be expected. The somewhat higher wave heights in the deeper sea region in the model by Pararas-Carayannis and Mader (2011) can be the result of higher initial vertical displacement at the seismic source (~ 50m) as compared with the gradual value of our computation. Fig. 24a, shows a histogram of results of computation of maximum wave heights using the key-board model for the great tsunamigenic earthquake of 21 July 365 A.D.. Though the general character of the histogram is consistent with that computed for the standard model of seismic source (Fig. 24b), the distribution of tsunami wave heights is somewhat different. In addition, from Fig. 24a it is well seen that maximum wave heights can exceed 5 m, while wave heights in histogram from work [11] are somewhat less.

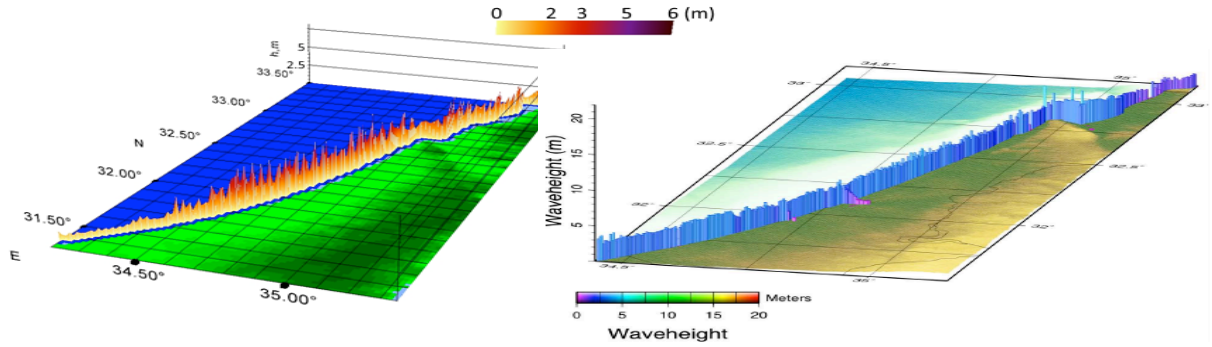

a) **b)**

Figure 24. Comparison of histograms of distribution of maximum wave heights for great earthquake of 21 July 1948 A.D. at the east coast of the Mediterranean Sea: a) present results; b) data from work [11].

So, numerical simulation performed to model historic tsunami in Mediterranean Sea, generated by great earthquakes occurred in 21 July 365 and 9 February 1948, demonstrates that for large and great earthquake, tsunami wave heights in some points of Mediterranean Sea's coast can reach 9 m. Such result relates mainly to near-field tsunami. It is necessary to note that depending on geodynamics of earthquake source, scatter of maximum heights at the coast under the same earthquake magnitude can differ in to 1.5-2 times. For far-field tsunami maximum wave heights can exceed 5 m.

ACKNOWLEDGEMENTS

This work was supported by the Russian Science Foundation, project no. 14-50-00095.

REFERENCES

EC (Earthquakes on Crete), 2016: http://www.sfakia-crete.com/sfakia-crete/earthquake.html

Lobkovsky L.I., 1988. Geodynamics of zones of spreading, subduction and two-level plate tectonics (Nauka Press, Moscow, USSR, 1988).

Lobkovsky L.I., Mazova R.Kh., Kataeva L.Yu., Baranov B.V., 2006. Generation and propagation of catastrophic tsunami in the basin of Sea of Okhotsk. Possible scenarios", Doklady 410, 528-531.

Mazova R., Tyuntyaev S., 2016. Tsunami at Sicilian coast from numerical simulation of two historical Mediterranean earthquakes, Abst.Book of 15th Plinius Conf. on Mediterranean Risks, 17.

Papadopoulos P., Daskalaki E., Fokaefs A., Giraleas N., 2010. Tsunami hazard in the Eastern Mediterranean Sea: Strong earthquakes and tsunamis in the west Hellenic arc and trench system, J. of Earthq. and Tsunami 4, 145-151.

Papazachos, B. C. 1996. Large seismic faults in the Hellenic arc. Ann. Geofis. 39, 891–903.

Pararas-Carayannis, G., 2001. The Potential for Tsunami Generation in the Eastern Mediterranean Basin and in the Aegean and Ionian Seas in Greece.
http://www.drgeorgepc.com/TsunamiPotentialGreece.html

Pararas-Carayannis, G., 2006. The Earthquake of January 8, 2006 in Southern Greece.
http://www.drgeorgepc.com/Earthquake2006Greece.html

Pararas-Carayannis G., Mader C.L., 2011. The Earthquake and Tsunami of 365 A.D. in the Eastern Mediterranean, Sci. of Tsunami Hazards, 30 (4), 1-10.

Pelinovsky E., Kharif C., Riabov I., Francius M. 2002. Modelling of Tsunami Propagation in the Vicinity of the French Coast of the Mediterranean, Natural Hazards 25, 135–159.

Salamon A., Rockwell T., Ward S.N., Guidoboni E., Comastri A., 2007. Tsunami Hazard Evaluation of the Eastern Mediterranean: Historical Analysis and Selected Modeling, Bull.Seism.Soc.Am., 97, 1–20. doi: 10.1785/0120060147.

Shaw B., Ambraseys N.N., England P.C., Floyd M.A., Gorman G.J., Higham T.F.G., Jackson J.A., Nocquet J.-M., Pain C.C., Piggott M.D., 2008. Eastern Mediterranean tectonics and tsunami hazard inferred from the AD 365 earthquake, Nature Geosci. 1, 268-276.

Sielecki A., Wurtele M., 1970. The numerical integration of the non-linear shallow-water equations with sloping boundaries, J.of Comp. Phys., 6, 219-236.

Thio H.K., 2009. Tsunami hazard in Israel, in: Report of URS Corp, Pasadena, USA, 2009, 72.

Tinti S., Armigliato A., Pagnoni G., and Zaniboni F., 2005**.** Scenarios of giant tsunamis of tectonic origin in the Mediterranean, ISET J. of Earthq. Techn., 42, 171-188.

Voltsinger N.E., Klevanny K.A., Pelinovsky E.N., 1989. Long-Wave Dynamics of Coastal Zone, (Gidrometeoizdat, Leningrad, USSR, 1989).

Wells D.L., Coppersmith K.J., 1994. New empirical relationships among magnitude, rupture length, rupture width, rupture area, and surface displacement, Bull.of Seism.Soc.of Am., 84. 974-1002.

Yolsal-Çevikbilen S., Taymaz T., 2012. Earthquake source parameters along the Hellenic subduction zone and numerical simulations of historical tsunamis in the Eastern Mediterranean, Tectonophysics,. 536–537, 61-63.

ISSN 8755-6839

SCIENCE OF **TSUNAMI HAZARDS**

Journal of Tsunami Society International

Volume 35 **Number 3** **2016**

ENHANCED VERTICAL EVACUATION APPLICATION WITH GEOMATIC TOOLS FOR TSUNAMIS IN SALINAS, ECUADOR

Andres Sebastian Matheus Medina, Mario Cruz D´Howitt, Oswaldo Padilla Almeida, Theofilos Toulkeridis* and Ana Gabriela Haro

Universidad de las Fuerzas Armadas ESPE, Sangolquí, Ecuador

*** Corresponding author:** ttoulkeridis@espe.edu.ec **or** theousfq@yahoo.com

ABSTRACT

Tsunami hazards are more than evident in the Pacific coast of Ecuador, but especially on its westernmost Peninsula called Salinas. As the potential impact time is relatively short for the public to reach natural high ground or at least leave the tsunami inundation area, a different approach to rescue lives has been applied with geomatic tools. The buildings inside the tsunami hazard zone have been first evaluated for their seismic resistance. Those buildings, which have been proven to withstand a seismic event, have been chosen to serve as elevated safe zones for a subsequent vertical tsunami evacuation. The used geographic tools allowed reducing time spans between initial evacuation points towards safe zones inside the tsunami inundation areas. The results of this study demonstrate the efficiency of vertical tsunami evacuation in a highly populated and visited touristic area in coastal Ecuador, as in Salinas appears a relatively high percentage of the population to far from shelters or elevated safe zones during a short-time impact of a tsunami.

Key words: *Tsunami, Seismic resistant buildings, Numerical modeling, Vertical Evacuation, Ecuador*

Vol. 35, No. 3, Page 189, (2016)

1. INTRODUCTION

Among earthquakes and floods, tsunamis are one of the most destructive and deadliest natural hazards (Raschky, 2008; Daniell et al., 2010). In recent years many studies have been performed to demonstrate and evaluate the vulnerability of coastal cities of short-warning impacts of potentially devastating tsunamis (Walters, and Goff, 2003; Dominey-Howes, and Papathoma, 2007; Taubenböck et al., 2009; Steinmetz et al., 2010). Therefore, the implementation of evacuation signs and routes for the survival of coastal areas vulnerable of the probable impact of tsunamis is a fundamental aspect of risk assessment (Johnston et al., 2005; Yeh et al., 2005; Jonientz-Trisler et al., 2005; Dengler, 2005). However, even when evacuation routes are assigned, still people who try to escape towards higher ground or outside the flooding zones, may do not reach such safe areas prior the impact of a tsunami or due to short warning times (Xie et al., 2012; Park et al., 2012). For such circumstances, it is recommended to apply vertical evacuation of in-situ-shelters, which themselves are resistant to the seismic event and the incoming tsunami (Reese et al., 2007; FEMA, 2008; Fraser et al., 2012; Muhari et al., 2012; Mas et al., 2013; Velotti et al., 2013; Wood et al., 2014).

The main aim of this research has been to demonstrate the efficiency of vertical tsunami evacuation in a highly populated and visited touristic area in coastal Ecuador, as in Salinas appears a relatively high percentage of the population to far from shelters or elevated safe zones during a short-time impact of a tsunami. The geographic tools used shall allow to reduce time spans between evacuation points towards safe zones outside the tsunami inundation areas and where applicable towards higher seismic resistant elevations within the hazard zones.

2. GEODYNAMIC SETTING

The Ecuadorian active continental platform is a frequent target of tsunamis due to the subduction of the oceanic Nazca Plate with the continental South American and Caribbean Plates, both separated by the Guayaquil-Caracas Mega Shear (Kellogg and Vega, 1995; Gutscher et al., 1999; Gusiakov, 2005; Egbue and Kellog, 2010; Pararas-Carayannis, 2012). Furthermore, in the same area tsunamis are generated not only from the mentioned tectonic origin but also due to enormous mass failures generating submarine landslides (Shepperd and Moberly, 1981; Pontoise and Monfret, 2004; Ratzov et al, 2007; 2010; Ioualalen et al., 2011; Pararas-Carayannis, 2012). A further origin of tsunamis has been credited to the Galápagos volcanism (Toulkeridis, 2011).

The Ecuadorian shoreline has witnessed a dozen times impacts of tsunamis (Fig. 1; 2) by mainly local origins in the last two centuries with various intensities one being of up to 8.8 Mw in 1906 (Rudolph and Szirtes, 1911; Kelleher, 1972; Beck and Ruff, 1984; Kanamori and McNally, 1982; Swenson and Beck, 1996; Pararas-Carayannis, 2012; Toulkeridis et al., 2016a; Rodriguez et al., 2016), while evidences of paleo-tsunami deposits are scarce (Chunga and Toulkeridis, 2014). Other prominent examples of tsunamis along the Ecuador–Colombia subduction zone include tsunamis in 1942 (Mw=7.8), 1958 (Mw=7.7), 1979 (Mw=8.2) and 2016 (Mw=7.8) within the 600-km long rupture area of the great 1906 event (Collot et al., 2004; Toulkeridis et al., 2016a; b). While the 1906 event caused

the death of up to 1500 persons in Ecuador and Colombia, the 1979 tsunami killed in Colombia at least 807 persons (Pararas-Carayannis, 1980). The evaluation of the last marine quakes, which generated tsunamis, suggests that the probability of a major or great earthquake in this margin region is enormous, especially as there must be substantial strain accumulation (Pararas-Carayannis, 2012).

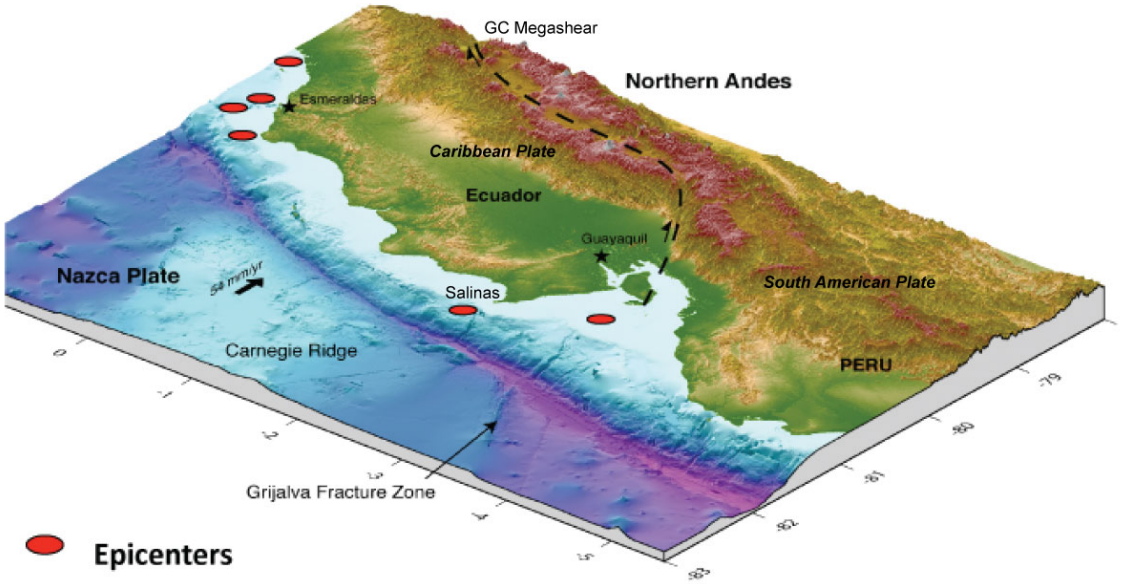

Fig. 1: Panoramic view of the morphology of western Ecuador and location of seismic epicenters, which generated tsunamis in the last 110 years. Adapted and modified from Collot et al., 2004.

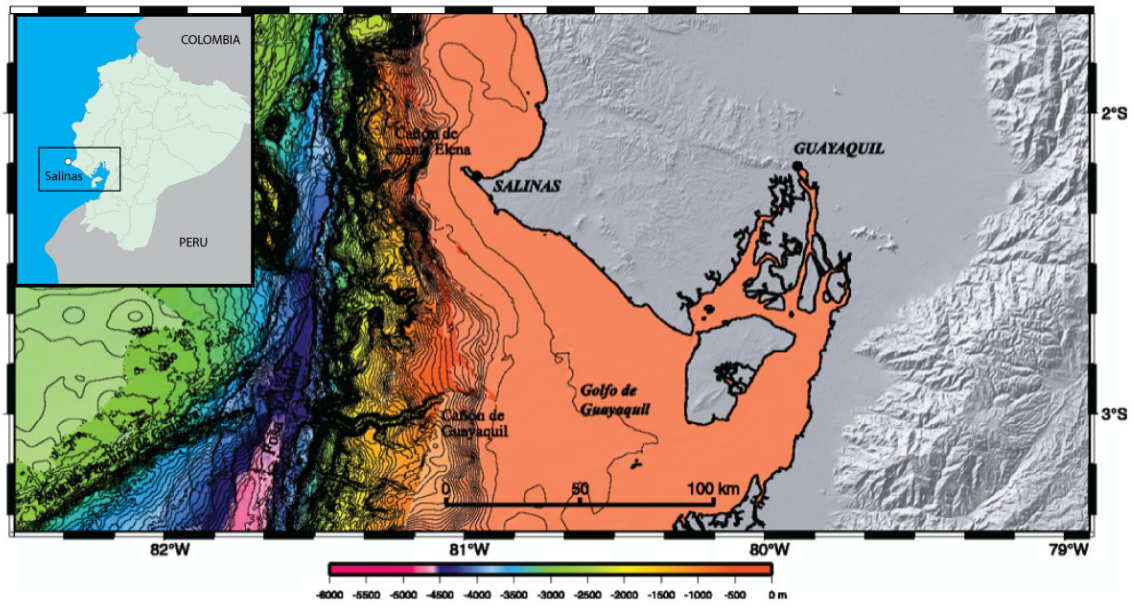

Fig. 2: Bathymetric map and location of Salinas. Adapted and modified from Collot et al., 2004.

3. TSUNAMI HAZARD IN SALINAS

The city of Salinas is part of the Santa Elena peninsular and is the most visited touristic area for its beaches and hotel infrastructure in Ecuador (Fig. 2; 3). Based on the last census of 2010, the population of the peninsula reaches some 281,467 persons and receives some 200,000 visitors at high seasons, which means that the area reaches a usual density of some 1082,22 persons per km^2 (27,07 km^2) in the urban area and up to 2,164,47 persons per km^2 at high seasons. Salinas will suffer serious damages when a tsunami will occur because the city is situated practically at sea level, except for the "Loma Lighthouse" where a military zone has been established being at some 80 m.a.s.l. The second elevated safe zone being relatively accessible for the neighborhoods around the Hotel Barceló Miramar is "Petropolis", an oil field located between Salinas and Santa Rosa. That mans, that the calculated flood area cover almost the entire city of Salinas, including the hotel and commercial infrastructure as well as great part of the military zone (Fig. 4a).

Fig. 3: Aerial view of the beach, hotel and commercial area of Salinas.

The Peninsula is exclusively composed by quaternary sediments of the so-called Tablazo formation above some minor outcrops of Cretaceous ophiolites of the Cayo Formation (Olsson, 1931; Senn, 1940) and it is situated along the Ecuador–Colombia subduction zone, at alatitude of 2.10ºS (Fig. 2, 4, 5). As the Santa Elena Peninsula is the westernmost continental spot of Ecuador, a tsunami that may be triggered in this active tectonic zone will reach Salinas in just a few minutes (Padilla et al., 2009).

therefore this sector becomes a critical and highly vulnerable area (Fig. 5 a b). Due to these circumstances, an alternative form of potential survival for the public may be the vertical evacuation in buildings, which themselves are considered seismic-resistant.

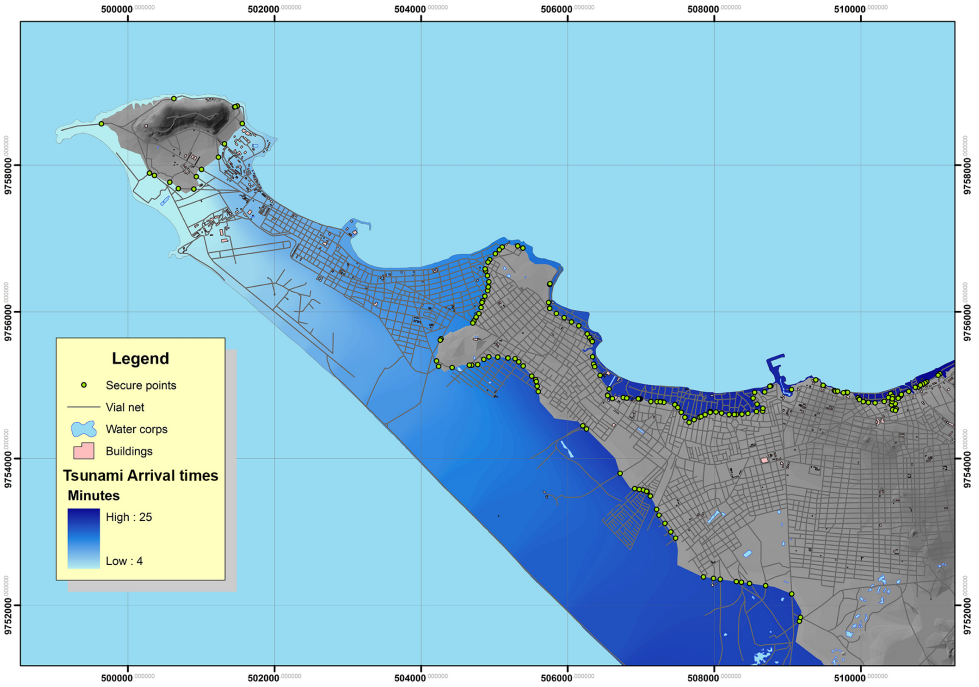

Fig. 4: Tsunami arrival times of Salinas.

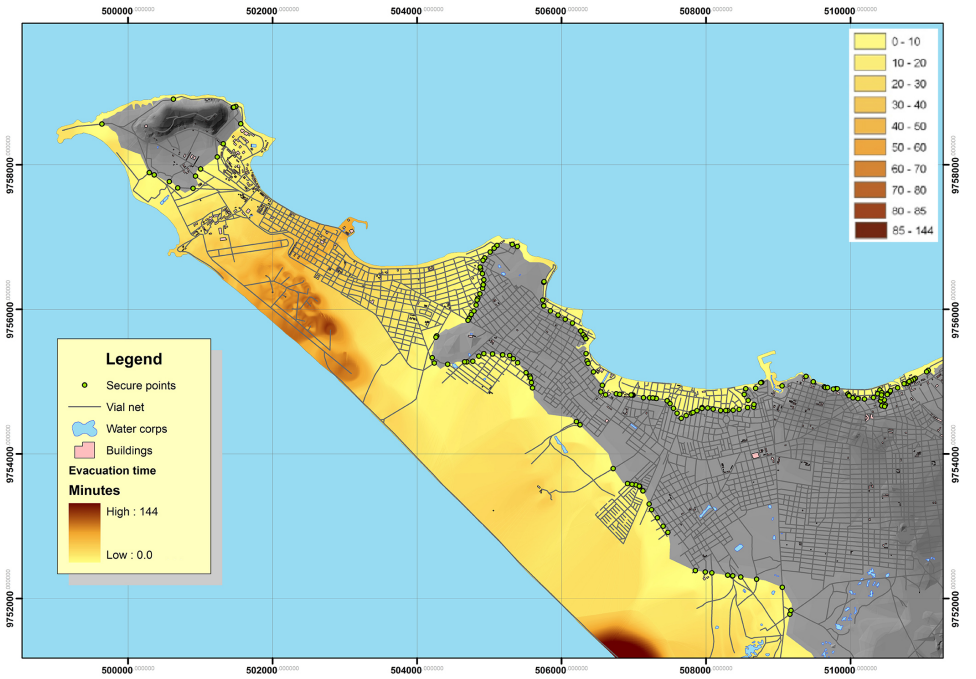

Fig. 4: Tsunami Evacuation times in Salinas.

4. METHODOLOGY

4.1 Seismic resistance

Vertical evacuation refuges from tsunamis are valuable risk-reduction facilities for highly populated regions where higher ground zones are not accessible or where arrival times of tsunami waves are short (Wood et al. 2014). A previously conducted study concluded that the first tsunami wave would strike Salinas in 8 to 12 minutes being around six meters high (Padilla et al., 2009; Matheus, 2012). Therefore, Salinas is an ideal place where vertical evacuation needs to be considered due to its location and geomorphological conditions. In this respect to withstand tsunami forces, and elevate evacuees above the maximum expected tsunami wave height (FEMA 2008), a tsunami vertical evacuation shelter is a building or earthen mound designed and constructed to withstand tsunami forces, and elevate evacuees above the maximum expected tsunami wave height (FEMA 2008).

Building a structure for a vertical evacuation shelter may cost up to 20% more than a building without tsunami preventive construction techniques. Instead, existing heavy constructions such as reinforced concrete buildings may be considered as potential tsunami shelters once detailed structural analyses are conducted to establish if the structures are capable of withstanding ground motions and forces associated with tsunamis waves (FEMA 2012). A tsunami vertical evacuation shelter must be designed to resist the generating earthquake plus eight different types of tsunami forces: (1) hydrostatic forces; (2) buoyant forces; (3) hydrodynamic forces; (4) impulsive forces; (5) debris impact forces; (6) debris damming forces; (7) uplift forces; and, (8) additional gravity loads from retained water on elevated floors (FEMA, 2008).

Regarding the structure, ductile and redundant systems that remain functional after an earthquake are required. Additionally, open systems that offer minimum resistance to water flow, and strong and deep foundations play an important role when choosing an appropriate structural configuration for a vertical evacuation facility. Reinforced concrete moment resisting frame buildings and structural wall systems with their walls parallel to the predicted wave flow accomplish these conditions. Accessibility for individuals with physical disabilities should also be considered when selecting on a vertical evacuation facility.

Our study has been conducted to identify possible vertical evacuation buildings / shelters in Salinas. The survey included a total of 61 buildings inspected. Considering most of the criteria described above and a minimum number of stories equal to five, only seven buildings in Salinas were selected as potential vertical evacuation shelters (Fig. 6). Once these buildings have been selected, a second phase of the study would consist of performing detailed structural evaluations to verify if the buildings are certainly capable of withstanding strong ground shakings according to the Ecuadorian Construction Standards NEC-15 and the described forces originated from a tsunami (NEC-15, 2015).

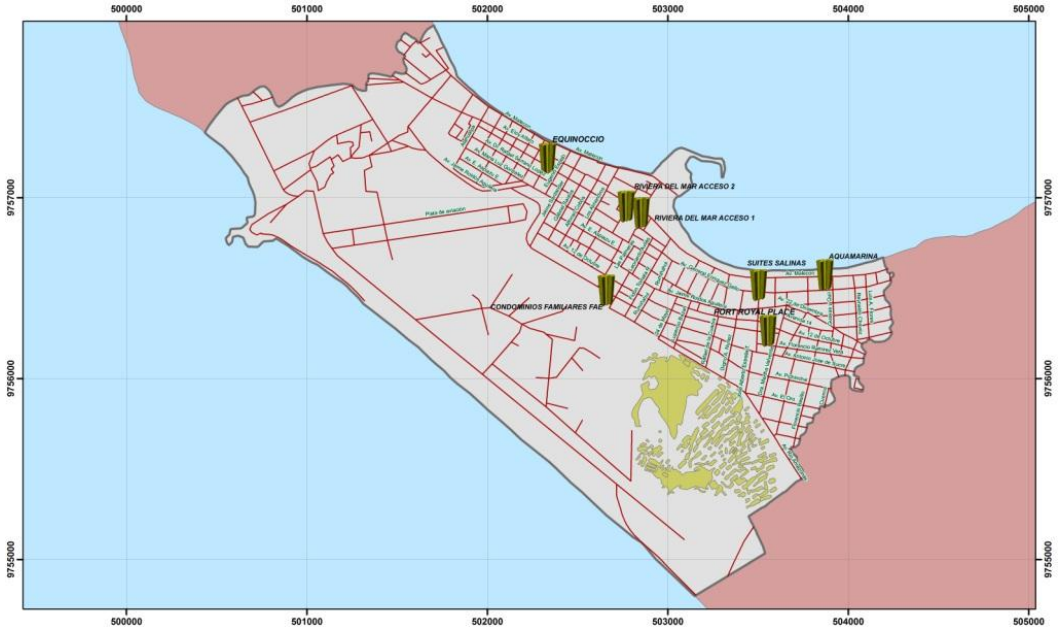

Figure 6: Potential vertical evacuation shelters on seismic resistant buildings in Salinas.

Such vertical evacuation shelters in addition to be earthquake resistant features, they have wide access, which will allow the rise of the evacuees safely and relatively quickly. The streets and avenues that can reach each security checkpoints are in good condition, are spacious and have no congestion by automotive traffic, which would provide a good value access to areas near these points.

4.2 Modelling the vertical evacuation accessibility

Based on the mentioned consideration about limited evacuation times and accesses, we have considered to evaluate and apply vertical evacuation as a plausible alternative towards the potential tsunami hazard. Once we have identified which buildings are considered to be safe, the next step has been the creation of scenarios for different evacuation times, for the subsequent determination of the coverage areas of each building. Within such we need to identify the accessibility values, times of mobilization and determine the optimal evacuation routes.

4.2a Methodology to determine evacuation scenarios

Time is always crucial when different scenarios are generated. In case of using an immediate evacuation, the time factor determines the amount of people who may be able to be saved from the tsunami hazard. In a representative building with 10 floors, we took the time a person needs to access the uppest terrace starting from the opposite sidewalk. In order to have unbiased information of such race, we have chosen four persons with different characteristics of gender, age and health status (Table 1).

Table 1: Times of ascent. Awareness is the addition of one minute to the taken time for the ascent. The 2´38´´is the average time of the first three persons

	Gender	Age	Physical condition	Time	Awareness
Person 1	Female	23 years	good	1´40´´	2´38´´
Person 2	Male	26 years	good	1´20´´	
Person 3	Male	50 years	good	1´54´´	
Person 4	Male	55 years	bad	2´40´´	3´40´´

As indicated in Table 1, the times obtained by the first three people determined a difference of about 34 seconds between them, while the fourth person obtained a very remote time related to the others. Therefore, it has been decided to average the first three times and have a second time value obtained by the fourth person of the ascent towards the security areas. These are, at least the fifth floor of the buildings that function as security points. To the obtained times we added one extra minute which would be the time range calculated for a person to react about the psychological impact caused by the earthquake and or activation of a tsunami warning (Table 1). The values obtained were subtracted from the times of the arrival of the first tsunami wave and thus the different scenarios of times in order to reach safe areas (Table 2). These and other data and parameters were used to obtain evacuation maps as illustrated methodology of in Fig. 7**.**

Table 2: Impact time and corresponding scenarios for the city of Salinas

	Arrival of tsunami (T)	Arrival in safe zone (T)	Total (T)
Scenario 1	11´	2´38´´	8´22´´
Scenario 2	11´	3´40´´	7´20´´

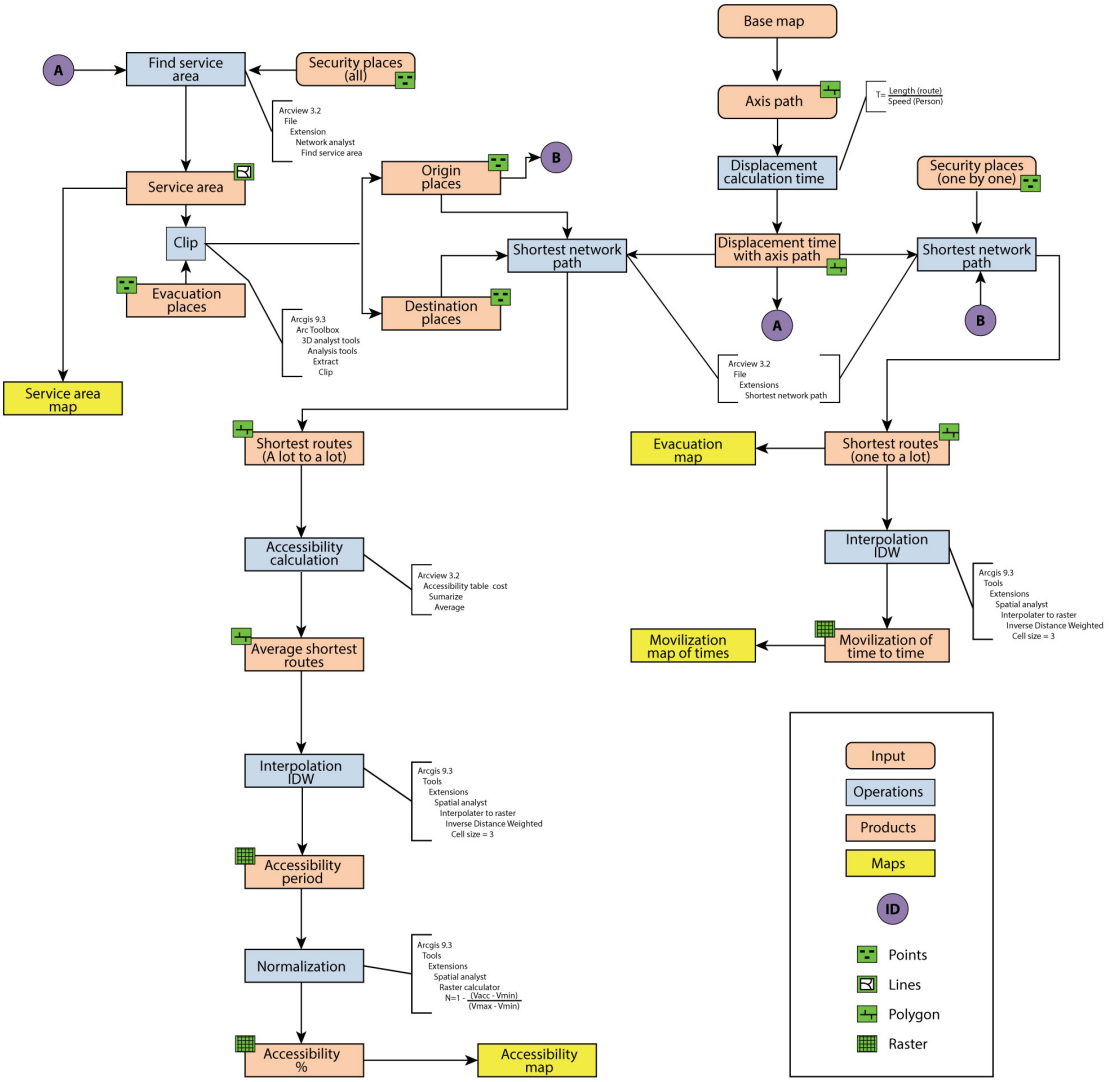

Fig. 7: Methodology to obtain maps due to a vertical evacuation model

4.2b Determination evacuation coverage areas (ECA)

In order to obtain the coverage areas of each safe area or site, the road network with a field showing all times impedance of each track segment were needed. These were elaborated with basic tools of Arcgis^{TM}, and the application Clip^{TM}. With these applications we proceeded to recalculate the mobilization times for each road segment, for which two new fields were created in the attribute table of coverage of roads, called: RECALC_MIN and speed. In the second field the velocity data were entered with the given parameter of which people move on foot in an emergency being equivalent to 150m / minute (FEMA, 2008).

The field "RECALC MIN" I was assigned for values through the Field Calculator tool, using the following formula:

Where,

Length: Distance in meters of each road segment.
Speed: Speed, expressed in meters per minute at which people move walking.
Impedance: Value of penalty that is given to each track according to obstacles or facilities being provided while using it.

With such calculation we obtained the mobilization times of the main road or path axes. For the following process we loaded the coverages of the safe areas and sites and the recently modified road network. Network analysis was performed using the tool allowing us to determine the coverage area for each evacuation safe area. While the tool has been deployed we proceeded to enter the safe area points and values of the scenarios, of which we seeked to obtain the coverage areas of each point. We further proceeded to resolve the function and coverage area for each safe area site, expressed as a polygon. With the obtained coverage polygons, we used editing tools in order to delimit the polygons avoiding any overlap of their areas to each other. The criteria we have used for the delimitation has been capacity of reception of each safe site.

4.2c Shortest ways

Only the evacuation points (input), that were situated within each coverage area using the Clip™ tool were extracted. With the layer of the evacuation points of each coverage area a new network analysis through GIS has been realized. With that we were able to determine the shortest route between two points coverages, with the time expressed in minutes being a determining factor. In order to obtain the mobilization times, we entered the coverage evacuation points and they were compared versus the safety point of each coverage area. After performing this process a new linear coverage of the most optimal routes was obtained with a corresponding table attribute.

The same procedure was performed to obtain accessibility times, with the difference that this time we entered and compared the coverage evacuation points versus the coverage destination points, which, for purposes of understanding represent the identical points. Consequently the routes coverage were obtained with their table attributes. With this linear coverage of the shortest routes, we elaborated the different evacuation route maps for each coverage area. From this point on, different procedures were determined to obtain the models of mobilization times and accessibility, pending on the methodology used.

4.2d Mobilization time model

With the tool Join™ we related the data in the table with the mobilization times with the attribute table coverage evacuation points (input) by the common field EVT_ID. By obtaining the mobilization timesheets corresponding to a coverage point, we proceeded to perform an interpolation using the

Inverse Distance Weighting method. The parameters for the tool to perform the process were entered, and the mobilization time model has been obtained.

4.2e Accessibility model

For an accessibility model, the average time of accessibility obtained before has been obtained by applying the equation:

$$Accesibility = \frac{Times\ of\ mobility\ (from\ each\ initial\ evacuation\ point\ until\ safe\ site)}{Number\ of\ evacuation\ point}$$

The table data were related with the average times of accessibility, with the attribute table coverage evacuation points (input) by the common EVT_LABEL, while using Join™. By receiving the timesheets accessibility corresponding to a coverage point, we proceeded to perform an interpolation using the Inverse Distance Weighting method. The parameters for the tool to perform the process were entered, and the mobilization time model has been obtained.
Unlike the model of mobilization times, accessibility values were expressed as a percentage, for which we proceeded to normalize the values of coverage using the Raster Calculator tool, applying the following equation:

$$Accesibility = 1 - \frac{total\ access - \min access}{Max\ access - \min access}$$

Where,
Acce.total: Raster of averaged times
Acce.min.: Minimum value of Acce.total
Acce.max.: Maximum value of Acce.total.

Whereupon we obtained the model in percentage values for each area of coverage.

5. RESULTS AND DISCUSSION

5.1 Evacuation coverage areas (ECA)

The evacuation coverage areas (ECA) represent the area of influence of buildings or security points, based on mobilization times expressed by a polygon on the ground. These coverage areas were obtained based on the times of each of the previously determined scenarios. The value of the existing population within each evacuation coverage area, has been obtained based on the index of population density through the last census in 2010 and the information given by the municipality of Salinas (INEC, 2010). During the vacation period the population increases by some 100%, which is also expressed and calculated in the second index of population density (Table 3).

Table 3: Population density of Salinas.

Public	Amount (Persons)	Urban area (Km^2)	Population density (Persons/Km^2)
Residents	29.294	27,07	1082,22
Tourists	58.588	27,07	2164,47

Based on the the two scenarios with the delimited times of 7 minutes and 20 seconds and 8 minutes an 22 segundos, respectively, we determined some seven evacuation coverage areas each, one for each safety point (Fig. 8). Based on the polygons obtained, which represent evacuation coverage areas and by the rate of population density, the number of existing population has been calculated within each of these areas, both at the time of low and high population density (high season, weekends and holidays; Table 3, 4).

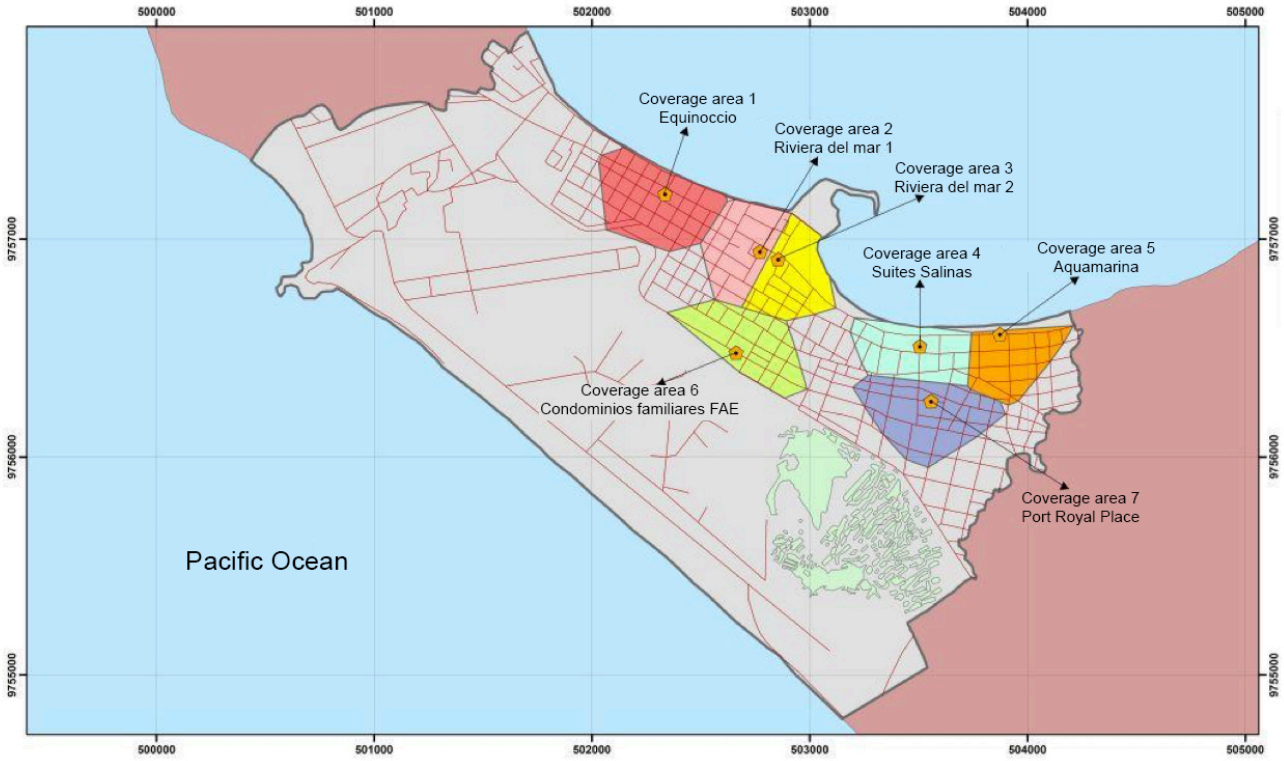

Fig. 8: The seven evacuation coverage areas (ECA), for the first scenario of Salinas.

Table 4 ECA attributes (first scenario) of Salinas.

Coverage area	Population (low season)	Population (high season)	Locations
ECA 1 - Equinoccio Building	196	392	Adapted
ECA 2 - Riviera del Mar 2	134	268	Adapted
ECA 3 - Riviera del Mar 1	132	264	Adapted
ECA 4 - Suites Salinas	141	281	Adapted
ACE 5 - Aquamarina Building	123	247	Adapted
ECA 6 - Condominios FAE	157	314	Adapted
ECA 7 - Port Royal Place	193	385	Insufficient (high season)

Table 5: ECA attributes obtained for the second scenario of Salinas.

As

Coverage area	Population (low season)	Population (high season)	Locations
ECA 1 - Equinoccio Building	237	474	Adapted
ECA 2 - Riviera del Mar 2	145	290	Adapted
ECA 3 - Riviera del Mar 1	147	294	Adapted
ECA 4 - Suites Salinas	179	359	Adapted
ACE 5 - Aquamarina Building	123	247	Adapted
ECA 6 - Condominios FAE	187	374	Adapted
ECA 7 - Port Royal Place	214	429	Insufficient (high season)

As the value of the population density has been calculated based on the urban area, a polygon within the study area defined as vertical evacuation area for the city of Salinas has been taken into account (Fig. 9).

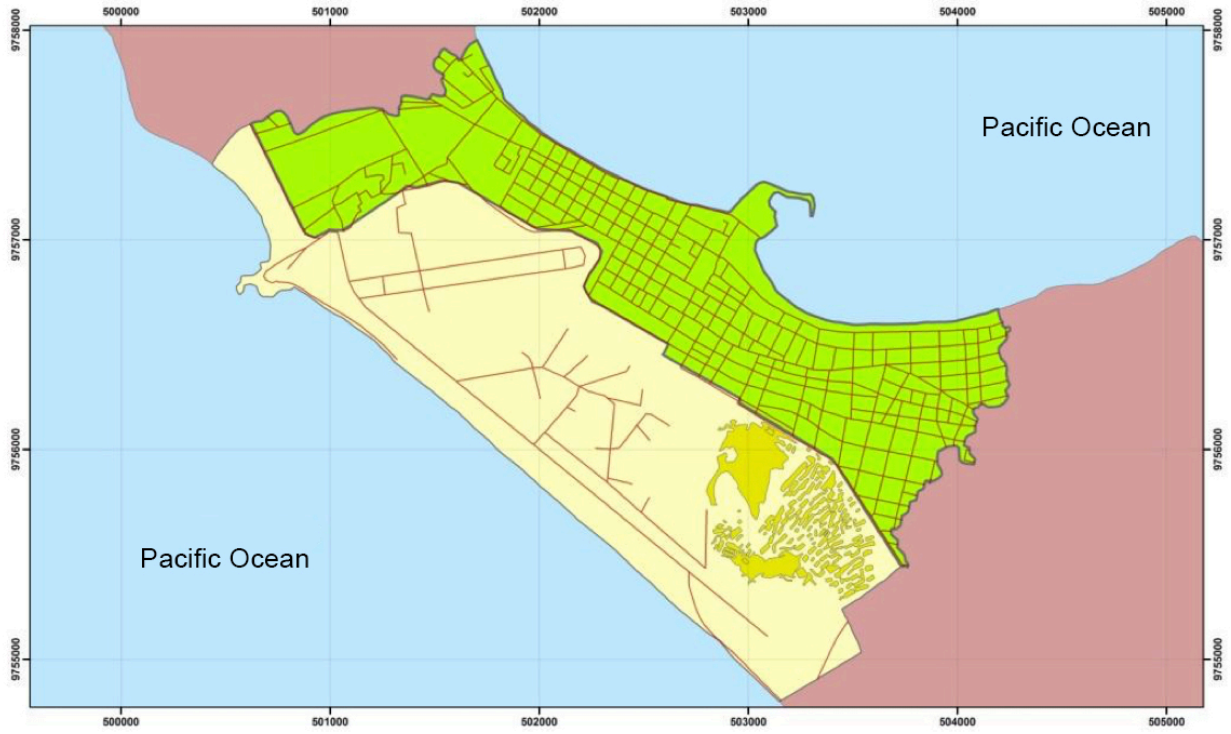

Fig. 9: Urban area (green) within the vertical evacuation zone of Salinas.

The urban area within the vertical evacuation zone covers a total of 2,241Km^2. The corresponding existing population value has been calculated within this zone and compared with the population which would be able to reach a safe area before it will affected by the first tsunami wave (Table 6).

Table 6: Calculated final amounts within the evacuation of Salinas.

Season	Indicadors	Scenario 7´20´´	Scenario 8´22´´
Low	Total population	2425	2425
	Evacuated persons	1076	1261
	Human loss	**1350**	**1164**
High	Total population	4851	4851
	Evacuated persons	2151	2522
	Human loss	**2699**	**2329**

Seven different models of accessibility for each specific scenario for the city of Salinas were obtained. To describe the results of accessibility three of the seven corresponding models are presented to each time scenario (Fig. 10; Table 7, 8).

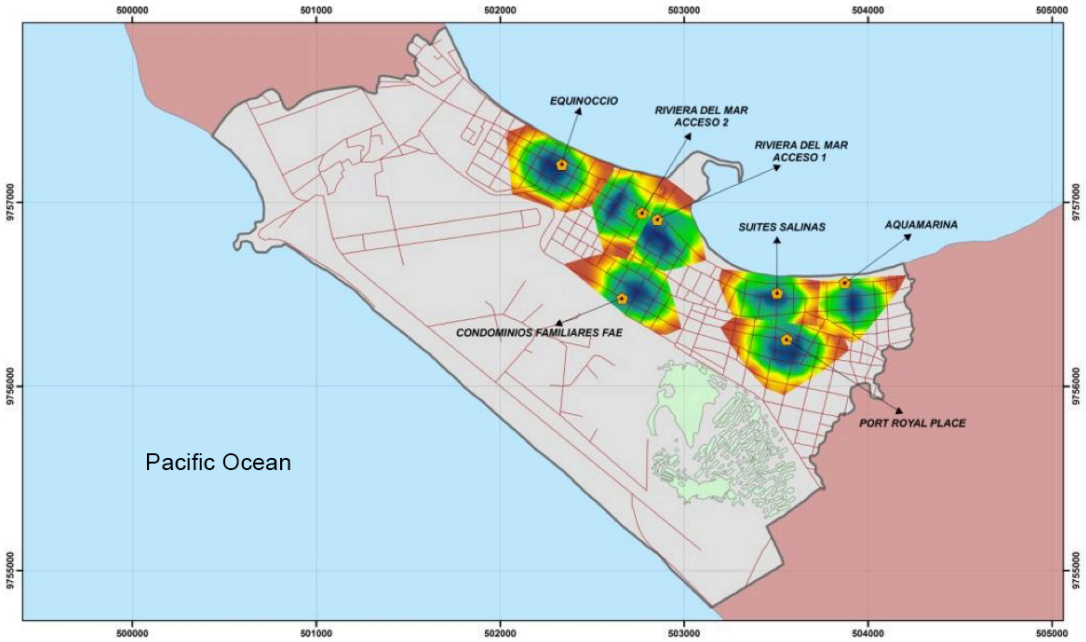

Fig. 10: Accessibility models for the first scenario of Salinas

Table 7: Description of the Accessibility Model for the first stage (scenario) of Salinas.

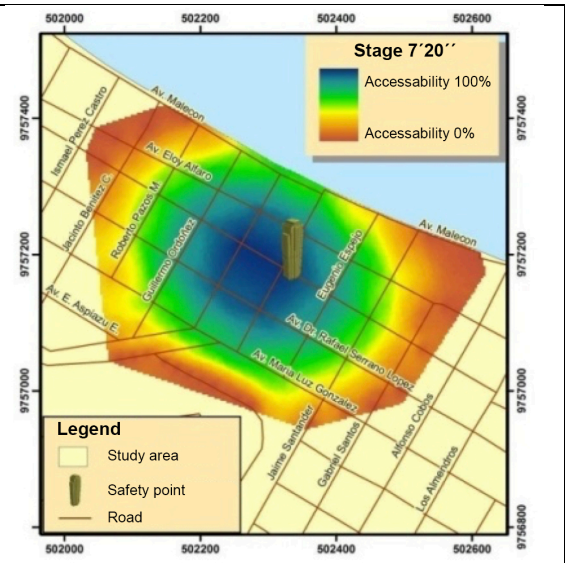	**EQUINOCCIO BUILDING** High values of accessibility reaching between 80% and 100% towards the center of the coverage area, specifically between the streets Guillermo Ordoñez and Eugenio Espejo. Low percentages between 0% and 20% were obtained in the extreme west, east and south of the coverage area.

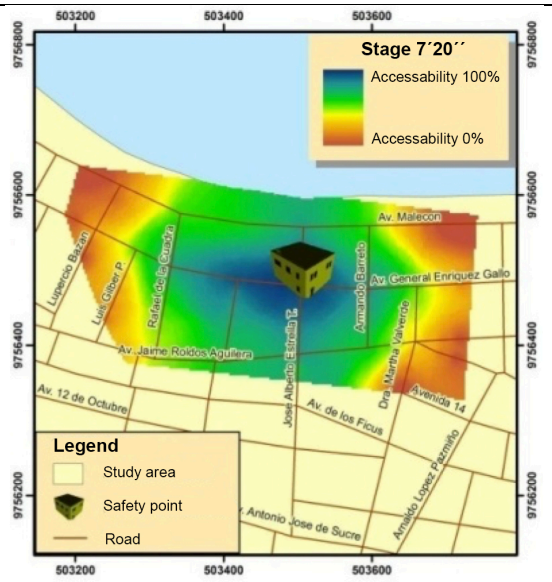	**SUITES SALINAS** High values of accessibility were obtained being of up to 80% to 100% towards the center of the coverage area, specifically between te streets Rafael de la Cuadra and Armando Barreto. Low percentages between 0% and 20% were obtained in the extreme west and east of the coverage area.
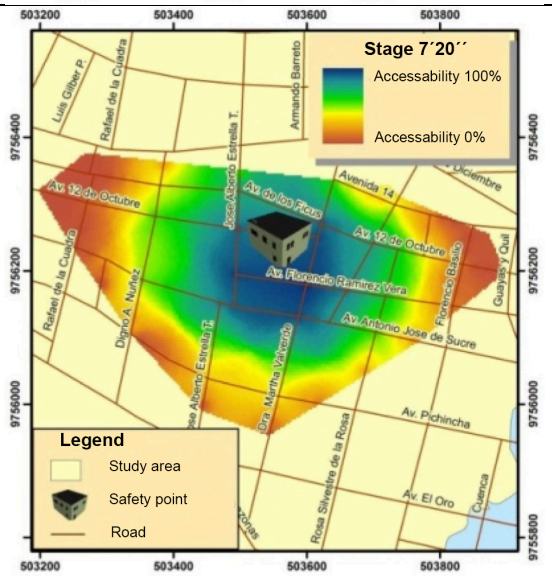	**PORT ROYAL PLACE** High values of accessibility were obtained being of up to 80% to 100% towards the center of the coverage area, specifically between te streets José Alberto Estrella and Dra. Martha Valverde. Low percentages between 0% and 20% were obtained in the extreme west and east of the coverage area.

The models obtained from the second scenario (stage) corresponding to 8 minutes 22 seconds has been very similar, with the difference that the coverage areas are extended ranging between 50 and 60 meters more, each.

5.2 Mobilization times

The mobilization is represented by the value of time it takes for a person to move from one initial point of evacuation to the nearest safety point, through the existing road network. Seven models of mobilization times for each of the two scenarios were determined for the City of Salinas, of which we have chosen to present three of them.

Table 8: Description of the mobilization model for the first stage (scenario) of Salinas.

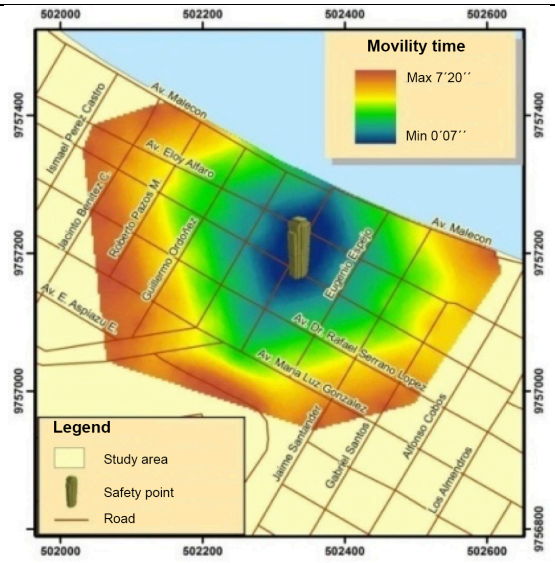	**EQUINOCCIO BUILDING** The lowest mobilization times were between 0'07" and 2'30" and are obviously within the area between the streets Pedro Jose Rodriguez and Eugenio Espejo. Consequently the highest times are in the remote areas related to the safety points.
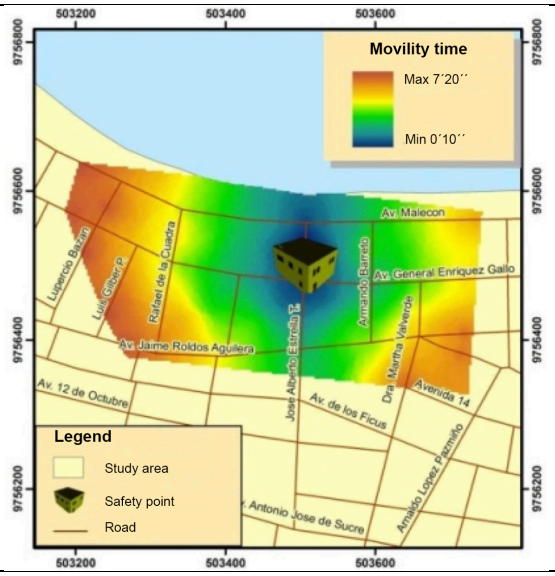	**SUITES SALINAS** The lowest mobilization times were between 0'07" and 2'30" and are obviously within the area between the avenues Malecón and General Enríquez Gallo. Therefore, the highest times are in the remote areas related to the safety points.

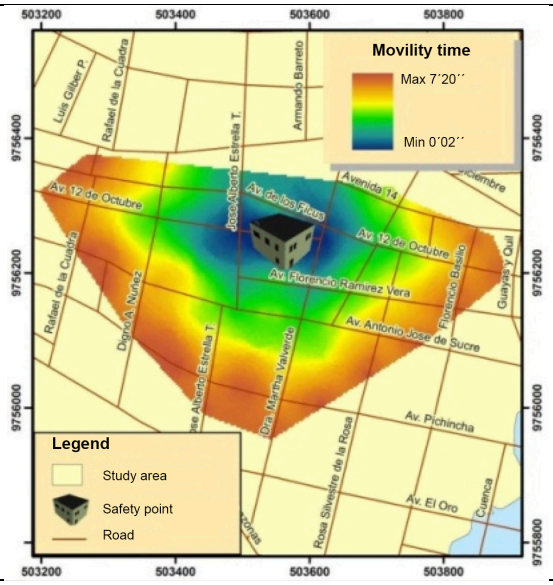

PORT ROYAL PLACE

The lowest mobilization times were between 0'07" and 2'30" and are obviously within the area between the streets de los Ficus and Florencio Ramírez. The highest times are in the remote areas related to the safety points.

According to the coverage areas of the second stage (scenario) corresponding to 8 minutes and 22 seconds, the obtained models are very similar, with the approximate addition of 1 further minute for every 60 meters on the road network.

5.3 Evacuation routes

The optimal evacuation routes are not necessarily the shortest, were obtained from the linear coverage mobilization times. With this coverage we determined the route with their respective mobilization time from any initial evacuation point to the safety point. We obtained seven models of evacuation routes for the most critical scenario (7'20") of the city of Salinas, of which we have chosen to present three representative examples.

Table 9: Description of the evacuation route model for the first stage (scenario) of Salinas.

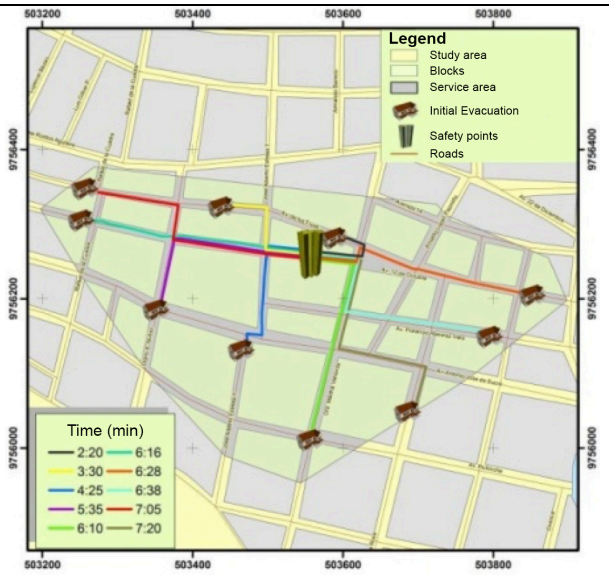	**EDIFICIO EQUINOCCIO** With a maximum time span for an evacuation of 7'20" the amount of evacuation points is considerable. However, road access and proper building entrances allow suitable conditions to facilitate the evacuation.
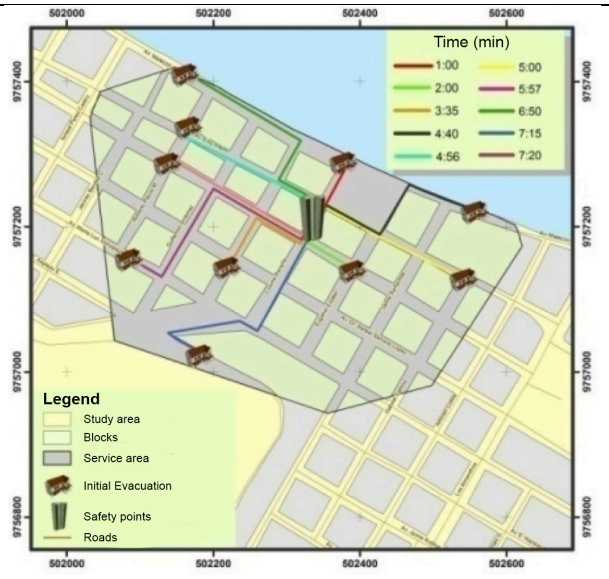	**SUITES SALINAS** With a maximum time span for an evacuation of 7'20" the amount of evacuation points is also in this example considerable. The road access and proper building entrances allow suitable conditions to facilitate the evacuation.

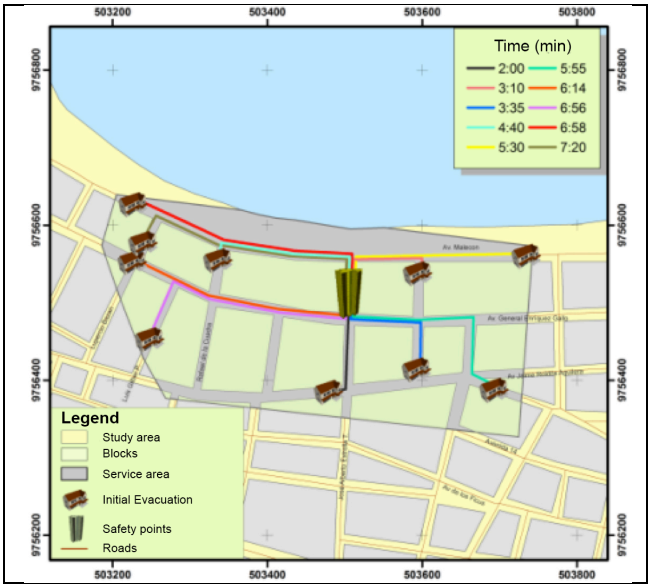

PORT ROYAL PLACE

Identical conditions like in the first two examples. Nonetheless, being an unfinished building, still in construction, its lower access and sites may be modified, so that evacuation allows to be optimal.

In the case of the second scenario (8'22") determined for the city of Salinas, in the same way we are able to determine the optimal route from any initial evacuation point to the safety point of each evacuation coverage area.

6. CONCLUSIONS

For the purposes of this research, the worst case scenario has been taken into consideration, in which we incorporated variables that include the most unfavorable conditions that may arise, in order to calculate and determine a greater safety margin that allows to save a high amount of human lives possible. To narrow vertical evacuation areas, the calculated tsunami arrival times for Salinas were used based on previous studies.

The potential areas of vertical evacuation of Salinas, have a high density of buildings with heights over four floors, but unfortunately a very low percentage of them are constructed under the existing norms and standards of earthquake resistance. In addition, due to the proximity of these buildings, in case of of an earthquake occurrence, these circumstances raise the degree of damage between them.
Las áreas de cobertura de evacuación (ECA), de cada punto de seguridad, conjuntamente con el índice de densidad poblacional, nos permiten conocer el número de personas que podrían ser evacuadas a cada edificio.

The ECA of each safety point, together with the population density index, allow us to know the amount of people who will be able to be evacuated to each building. However, in some cases, the buildings have unfortunately insufficient space to accommodate all evacuated persons.
According to the accessibility maps and mobilization times obtained, those living in the areas closest to elevated safe areas are more likely to reach them considering the factors of time, impedance and accessibility but being pendent on street network conditions.

With models and coverage areas obtained we were able to determine the paths and optimal times from anywhere within the ECA towards the safety points.

ACKNOWLEDGMENTS

We thank the Municipality of Salinas and the Universidad de las Fuerzas Armadas ESPE for logistic and financial support.

REFERENCES

Beck, S.L. and Ruff, L.J., 1984: The rupture process of the great 1979 Colombia earthquake: evidence for the asperity model. J.Geophys. Res.89: 9281–9291

Chunga, K. and Toulkeridis, T. (2014). First evidence of paleo-tsunami deposits of a major historic event in Ecuador. J. Tsunami Soc. Int, 33: 55-69.

Collot, J.Y., Marcaillou, B., Sage, F., Michaud, F., Agudelo, W., Charvis, P., Graindorge, D., Gutscher, M.A. and Spence, G., 2004. Are rupture zone limits of great subduction earthquakes controlled by upper plate structures? Evidence from multichannel seismic reflection data acquired across the northern Ecuador–southwest Colombia margin. Journal of Geophysical Research: Solid Earth, 109(B11).

Daniell, J.E., F. Wenzel, and B. Khazai. 2010. The Cost of Historical Earthquakes Today – Economic Analysis since 1900 through the use of CATDAT. Paper presented at the Australian Earthquake Engineering Society 2010 Conference, Perth, Western Australia: 15 pp.

Dengler, L., 2005. The role of education in the national tsunami hazard mitigation program. In Developing Tsunami-Resilient Communities (pp. 141-153). Springer Netherlands.

Dominey-Howes, D. and Papathoma, M., 2007. Validating a tsunami vulnerability assessment model (the PTVA Model) using field data from the 2004 Indian Ocean tsunami. Natural Hazards, 40(1): 113-136.

Egbue, O. and Kellogg, J., 2010: Pleistocene to Present North Andean “escape”. Tectonophysics 489: 248-257.

FEMA 2008. Guidelines for Design of Structures for Vertical Evacuation from Tsunamis. Washington, D.C., Federal Emergency Management Agency.

FEMA, 2012. Tsunami Vertical evacuation FEMA P646, Available at: https://www.youtube.com/watch?v=_h26_DUKMzA.

Fraser, S., Leonard, G.S., Murakami, H. and Matsuo, I., 2012. Tsunami Vertical Evacuation Buildings–Lessons for International Preparedness Following the 2011 Great East Japan Tsunami. Journal of Disaster Research, 7: 446-457.

Gusiakov, V.K., 2005: Tsunami generation potential of different tsunamigenic regions in the Pacific. Marine Geology, 215, 1-2: 3-9.

Gutscher, M.A., Malavieille, J.S.L. and Collot, J.-Y., 1999: Tectonic segmentation of the North Andean margin: impact of the Carnegie ridge collision. Earth Planet. Sci. Lett. 168: 255–270.

INEC, 2010: Censo Nacional de Población y Vivienda. Quito: Instituto Ecuatoriano de Estadística y Censos.

Ioualalen, M., Ratzov, G., Collot, J. Y. and Sanclemente, E. (2011). The tsunami signature on a submerged promontory: the case study of the Atacames Promontory, Ecuador. Geophysical Journal International, 184(2), 680-688.

Johnston, D., Paton, D., Crawford, G.L., Ronan, K., Houghton, B. and Bürgelt, P., 2005. Measuring tsunami preparedness in coastal Washington, United States. In Developing Tsunami-Resilient Communities (pp. 173-184). Springer Netherlands.

Jonientz-Trisler, C., Simmons, R.S., Yanagi, B.S., Crawford, G.L., Darienzo, M., Eisner, R.K., Petty, E. and Priest, G.R., 2005. Planning for tsunami-resilient communities. Natural Hazards, 35(1), pp.121-139.

Kanamori, H. and McNally, K.C., 1982: Variable rupture mode of the subduction zone along the Ecuador–Colombia coast. Bull. Seismol. Soc. Am.72 (4): 1241–1253.

Kelleher, J.A., 1972: Ruptures zones of large South American earthquakes and some predictions. Journal of Geophysical Research, 77, 11: 2087-2103.

Kellogg, J.N. and Vega, V., 1995: Tectonic development of Panama, Costa Rica and the Colombian Andes: Constraints from Global Positioning System geodetic studies and gravity. Geol. Soc. Am. Special Paper 295, 75–90.

Mas, E., Adriano, B. and Koshimura, S., 2013. An integrated simulation of tsunami hazard and human evacuation in La Punta, Peru. Journal of Disaster Research, 8(2), pp.285-295.

Matheus, A., 2012. Modelo de evacuación vertical y horizontal en caso de ocurrencia de tsunami para las ciudades de Salinas y Bahía de Caráquez. Universidad de las Fuerzas Armadas ESPE. Unpublished Thesis, 195pp

Muhari, A., Koshimura, S. and Imamura, F., 2012. Performance evaluation of pedestrian bridge as vertical evacuation site during the 2011 tsunami in Japan. Journal of Natural Disaster Science, 34(1): 79-90.

NEC-15, 2015: Norma Ecuatoriana de la Construcción, SE-DS, Cargas Sísmicas. Diseño Sismo Resistente. Quito, Ecuador: 138pp.

Olsson, A.A., 1931. Contributions to the Tertiary paleontology of northern Peru: Part 4. The Peruvian Oligocene. Bull. Am. Pal., 17 (63): 100-264.

Padilla, O., Cruz D'Howitt, M. and Alvear Brito, J., 2009. Elaboración De Un Mapa De Accesibilidad Y Modelo De Evacuación Ante Una Eventual Ocurrencia De Tsunami En Las Ciudades De Salinas Y Bahía De Caráquez , Mediante Herramientas Geoinformáticas. Revista Geoespacial, 5: 1–15.

Pararas-Carayannis, G. 1980: The Earthquake and Tsunami of December 12, 1979, in Colombia. Intern. Tsunami Information Center Report, Abstracted article in Tsunami Newsletter, Vol. XIII, No. 1.

Pararas-Carayannis, G., 2012: Potential of tsunami generation along the Colombia/Ecuador subduction margin and the Dolores-Guayaquil Mega-Thrust. Science of Tsunami Hazards, 31, 3: 209-230.

Park, S., Van de Lindt, J.W., Gupta, R. and Cox, D., 2012. Method to determine the locations of tsunami vertical evacuation shelters. Natural hazards, 63(2), pp.891-908.

Pontoise, B. and Monfret, T. (2004). Shallow seismogenic zone detected from an offshore‐onshore temporary seismic network in the Esmeraldas area (northern Ecuador). Geochemistry, Geophysics, Geosystems, 5(2).

Raschky, P.A. 2008. Institutions and the losses from natural disasters. Natural Hazards and Earth System Science 8: 627-634.

Ratzov, G., Collot, J. Y., Sosson, M. and Migeon, S. (2010). Mass-transport deposits in the northern Ecuador subduction trench: Result of frontal erosion over multiple seismic cycles. Earth and Planetary Science Letters, 296(1), 89-102.

Ratzov, G., Sosson, M., Collot, J. Y., Migeon, S., Michaud, F., Lopez, E. and Le Gonidec, Y. (2007). Submarine landslides along the North Ecuador–South Colombia convergent margin: possible tectonic control. In Submarine Mass Movements and Their Consequences. Springer Netherlands: 47-55

Reese, S., Cousins, W. J., Power,W. L., Palmer, N. G., Tejakusuma, I. G., and Nugrahadi, S., 2007: Tsunami vulnerability of buildings and people in South Java field observations after the July 2006 Java tsunami, Nat. Hazards Earth Syst. Sci., 7, 573–589.

Rodriguez, F., DHowitt, M.C., Toulkeridis, T., Salazar, R., Romero, G.E.R., Moya, V.A.R. and Padilla, O., 2016. Journal of Tsunami Society International. Journal of Tsunami Society International, 35(1).

Rudolph E. and Szirtes S., 1911: Das kolumbianische Erdbeben am 31 Januar 1906, Gerlands Beitr. z. Geophysik , 2: 132- 275.

Senn, A., 1940. Paleogene of Barbados and its bearing on history and structure of Antillean-Caribbean region. AAPG bulletin, 24(9), pp.1548-1610.

Shepperd, G.L. and Moberly, R., 1981: Coastal structure of the continental margin, northwest Peru and southwest Ecuador. Geological Society of America Memoirs, 154: 351-392,

Steinmetz, T., Raape, U., Teßmann, S., Strobl, C., Friedemann, M., Kukofka, T., Riedlinger, T., Mikusch, E. and Dech, S., 2010. Tsunami early warning and decision support. Natural Hazards and Earth System Sciences, 10(9), pp.1839-1850.

Swenson, J.L. and Beck, S.L., 1996: Historical 1942 Ecuador and 1942 Peru subduction earthquakes, and earthquake cycles along Colombia–Ecuador and Peru subduc-tion segments. Pure Appl. Geophys.146 (1): 67–101.

Taubenböck, H., Goseberg, N., Setiadi, N., Lämmel, G., Moder, F., Oczipka, M., Klüpfel, H., Wahl, R., Schlurmann, T., Strunz, G. and Birkmann, J., 2009. " Last-Mile" preparation for a potential disaster–Interdisciplinary approach towards tsunami early warning and an evacuation information system for the coastal city of Padang, Indonesia. Natural hazards and earth system sciences, 9(4), pp.1509-1528.

Toulkeridis et al., 2016a: Real-Time Radioactive Precursor of the April 16, 2016 Mw 7.8 Earthquake in Ecuador. Submitted

Toulkeridis et al., 2016b: The 7.8 Mw Earthquake and Tsunami of the 16th April 2016 in Ecuador - A seismic evaluation and geological field survey. Submitted

Toulkeridis, 2011: Volcanic Galápagos Volcánico. Ediecuatorial, Quito, Ecuador: 364 pp

Velotti, L., Trainor, J.E., Engel, K., Torres, M. and Myamoto, T., 2013. Beyond vertical evacuation—research considerations for a comprehensive vertical protection strategy. International Journal of Mass Emergencies and Disasters, 31(1), pp.60-77.

Walters, R.A. and Goff, J., 2003. Assessing tsunami hazard along the New Zealand coast. Science of Tsunami Hazards, 21(3), pp.137-153.

Wood, N., Jones, J., Schelling, J. and Schmidtlein, M., 2014. Tsunami vertical-evacuation planning in the US Pacific Northwest as a geospatial, multi-criteria decision problem. International journal of disaster risk reduction, 9, pp.68-83.

Xie, J., Nistor, I. and Murty, T., 2012. Tsunami risk for Western Canada and numerical modelling of the Cascadia fault tsunami. Natural hazards, 60(1), pp.149-159.

Yeh, H.H.J., Robertson, I. and Preuss, J., 2005. Development of design guidelines for structures that serve as tsunami vertical evacuation sites (Vol. 4). Washington State Department of Natural Resources, Division of Geology and Earth Resources.

ISSN 8755-6839

SCIENCE OF **TSUNAMI HAZARDS**

Journal of Tsunami Society International

Volume 35 **Number 3** **2016**

BATHYMETRIC SOUNDING by REMOTE SENSING

Using ELECTROMAGNETIC RADIATION

Frank C Lin[1,*], George Pararas-Carayannis [1], Piyarat Silapasuphakornwong[2]

[1]Tsunami Society International, Honolulu, Hawaii 96815, USA
[2]Human Media Research Center, Kanagawa Institute of Technology, Kanagawa 243-0292, Japan

ABSTRACT

We describe a novel *modus operandi* to survey the ocean floor. We utilize the eruption of submarine volcanoes as a light source. The electromagnetic radiation emitted by such eruptions illuminate the ocean floor and thus provides information about the barythmetric topology, and a geostationary satellite can monitor this. Since the wavelength of the electromagnetic radiation is many orders of magnitude shorter than that of the acoustic wave, finer details of the bathymetric features can be obtained. We show that a topographical representation of the seabed can be derived from the Signal Diagram by a simple transformation (a mirror reflection). In this case the radiation is emitted by water molecules stimulated by the heat of the volcanic eruption, in contradistinction to the case of tsunami radiation, where the water molecules are stimulated by mutual collisions at high speed. We give two examples: Illapel, Chile and Chichi-shima, Japan. We have also shown that water molecules in the ocean, when stimulated by the heat of submarine volcanic eruption, will emit infrared radiation

Keywords: *Tsunami Radiation, Signal Diagram, Remote Sensing, Infrared Topography, Illapel, Chile, Chichi-Shima, Japan.*

**Corresponding author: linbfrank@gmail.com Tel/Fax: 662 612 4705*

1. INTRODUCTION

The deepest part of the ocean is to a large extent still *terra incognita*. Ocean relief originates from tectonic, erosional, depositional and volcanic processes. We can identify four major divisions on the ocean floor—(a) the continental shelf, (b) the continental slope, (c) the continental rise, (d) the abyssal plain. Besides these, there are many associated features—ridges, hills, seamounts, guyots, trenches, canyons, sleeps, fracture zones, island arcs, atolls, coral reefs, submerged volcanoes and sea-scarps. A knowledge of the ocean topography is of economic interest; for example, for fisheries, mineral extraction and potential source of oil. There is DNA evidence that life on earth began at hot ocean vents at the bottom of the ocean. Along the eastern and western rims of the Pacific a deep trench demarcates the subduction of tectonic plates. The morphology of oceans influences navigation, fishing, mining, climate, exploration and other important activities of man.

At present, bathymetric sounding is mainly performed by using sonic pulses. There are two types of sonars, active or passive. In active sonars, the transducer emits an acoustic signal, which bounces off an object, and this echo when received will determine the range of the object. This principle is the same as radar using radio waves. Passive sonars do not emit signals; they only receive noise from submerged sources such as submarines, whales and ships. The frequencies of the sonar signals can be as high as 1Mhz to provide higher resolution, or as low as 50kHz - which has a low resolution but is able to travel further distances.

In this paper we propose a novel methodology to sound the ocean depth, utilizing the fact that electromagnetic radiation, mostly in the infrared part of the spectrum, emitted by erupting submerged volcanoes or vents, will illuminate the ocean floor much as a flashlight will illuminate a dark room. This radiation is captured by a geostationary satellite, the analysis of which will yield topographical information, which is not available otherwise. The use of electromagnetic waves has the advantage, *vis-à-vis* sonic waves: it travels at the speed of light, its wavelength is many orders of magnitude shorter, and it is far more energetic. It can propagate in water, in atmosphere, and in vacuum. The record of such events is permanently stored and retrievable in satellite image archives. Although such events are limited to periodic eruptions, this is not a serious drawback since portions of the ocean floor where such events do not occur are static.

1. THE 16 SEPTEMBER 2015, ILLAPEL, CHILE EARTHQUAKE AND TSUNAMI

The Peru-Chile Trench is the active boundary of collision of the Nazca Plate with the South American Plate. Subduction of the Nazca plate beneath the South America continent is not homogeneous. As a result, asperities and structural complications have caused segmentation along the entire margin, resulting in zones with different rates of slip, seismic activity, volcanism, uplift, terracing and orogenic processes (Pararas-Carayannis, 2010). The northern upper end of the central seismic zone from 33º-30ºS is delineated by the oblique subduction of the leading edge of the Juan Fernández ridge with the Peru-Chile Trench near Valparaiso and the appearance of volcanism at the

southern end (Fig. 1) Five tsunamigenic earthquakes have occurred in this area in historic times: November 19, 1811; November 19, 1822; October 16, 1868; August 17, 1906 and March 3, 1985 (Pararas-Carayannis, 2010).

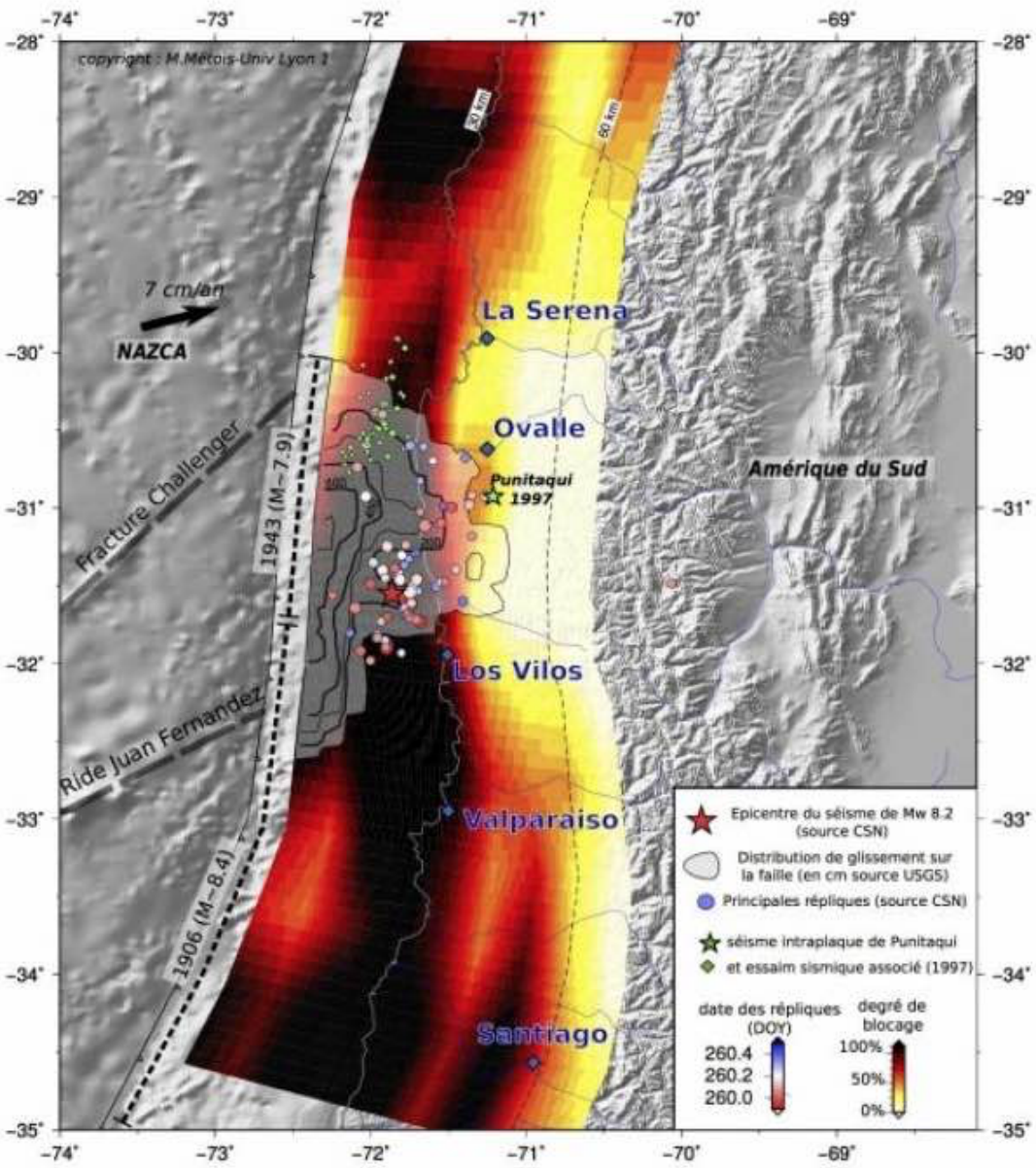

Fig. 1. Slip model of the earthquake and the aftershocks. The black areas are very locked areas or areas accumulating stress and capable of generating massive earthquakes (image via @cppgeophysics) http://earthquake-report.com/wp-content/uploads/2015/09/Screen-Shot-2015-09-19-at-11.59.55.jpg

On September 16, 2015 at a distance of 46 km from Illapel, Chile, and at 22:54:33 hours UTC, an earthquake with a moment magnitude of 8.3 occurred along the northern central zone bounded by the Juan Fernandez Ridge to the south and the Challenger Fracture to the north (Fig. 1). The initial quake lasted three minutes, and was followed by several aftershocks greater than magnitude six. The earthquake occurred on thrust faults along the boundary of the Nazca and South American plates. [1] The depth of the epicenter, located at 31.57˚ S and 71.65˚ W, was 22.4 km. At the latitude of this event, the Nazca plate is moving towards east-northeast at a velocity of 74 mm/yr. with respect to South America, and begins its subduction beneath the continent at the Peru-Chile Trench, 85 km to the west of the September 16 Earthquake (see Figs. 1 and 2). The size, location, depth and mechanism of this event are all consistent with its occurrence on the megathrust interface in this region. The length times the width of the event is about 230x100 km, or more concisely, an area of 23,000 sq. km. By comparison, the distance from Illapel to Santiago is approximately 230 km. [Lin et al 2016].

In order to compare the functionality of the electromagnetic sounding paradigm and other methods such as multibeam echo sounding or satellite radar deep-sea topography, we present in the following three figures to visually illustrate the pros and cons of our method *vis-à-vis* the conventional approach. We emphasize that there is a fundamental distinction since the conventional approach and our method are measuring different physical quantities. In the former case it is the actual seafloor being measured, and in the latter case the heat intensity being reflected into space.

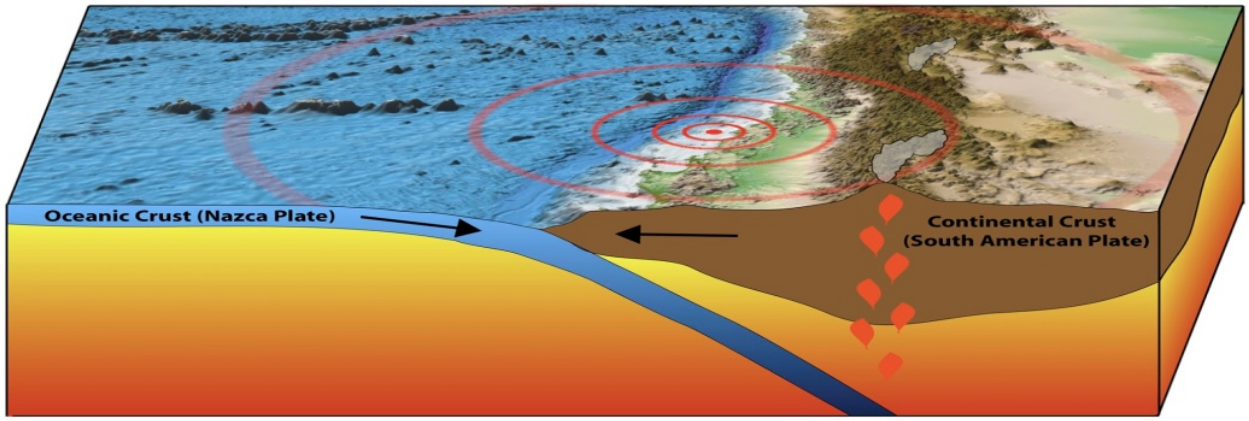

Fig. 2: Illapel Seaquake and the Peru-Chile Trench

In Fig. 2 we show an artist's version of the event, where the concentric circles radiate outward from the epic center. In the drawing we are able to discern the relative locations of the Pacific Ocean, the Peru-Chile Trench, the coastline of the South American continent, and the Andes mountain [3].

Figure 3, below shows the topographic features of the Chile Trench [4]:

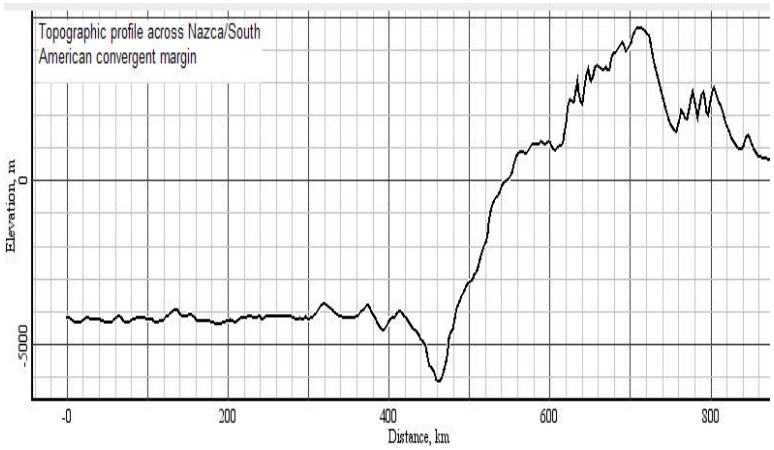

Fig. 3: Topographic profile across the Nazca-South American Plates

Here we recognize the same locations as in the artist's version, but this is a topographic representation of the seafloor relief. It shows that the seafloor steadily rises towards the South American continent and culminates in the peak of the Andes Mountain.

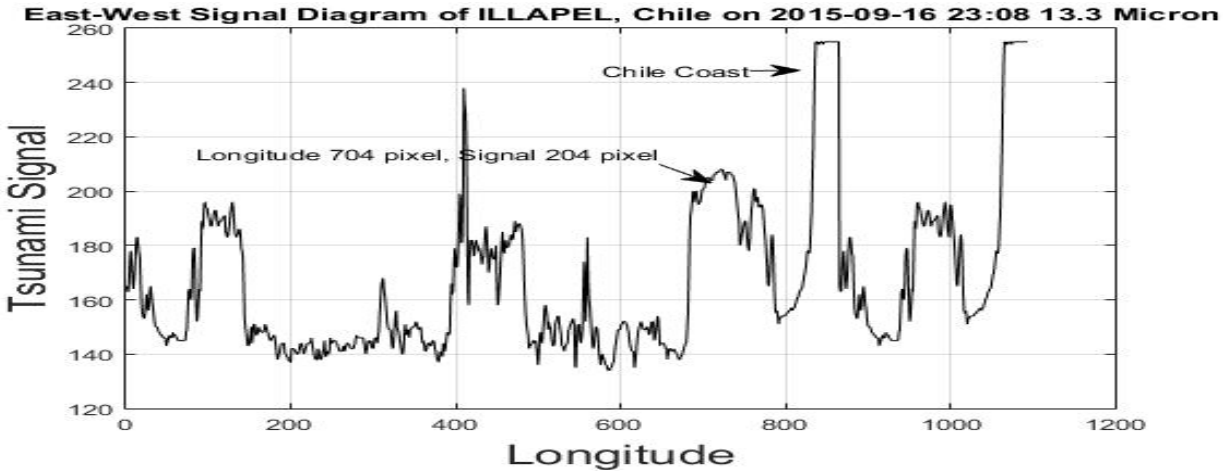

Fig. 4: Latitudinal Signal Diagram on 2015-09-16 at 23:08 UTC for 13.3 μm

In Fig. 4 we show a Signal Diagram [Lin et al, 2016], which represents a slice across the satellite image along the latitude of the seaquake event. Referring to the x-axis of Fig. 4, we note that the Tsunami Signal (which is the pixel brightness of the satellite image) at longitude 704 pixels is very broad, extending approximately 25 pixels in width (corresponding to a terrestrial distance of about 100 km); In this figure the Chilean coastline is clearly delineated, as pointed to by an arrow. We can also observe the enhanced radiation on the subduction zone from pixel 400 up to pixel 700 (i.e. the Continental Shelf) as compared with the Pacific Ocean for pixels less than 400. A very strong

peak at longitude 400 pixels demarcates the Peru- Chilean trench.

In comparison to the topographic relief map of Fig. 3., we are able to discern many 'fine structures', which indicate the existence of 'hot spots' such as erupting volcanoes, seamount vents, and fractures in the seabed. The sharp spike at 400 pixels indicates that a vast amount of heat has evolved due to the subduction of the Nazca plate below the South American plate. The seaquake itself, located at approximately 700 pixels, is remarkably extensive in size as compared to other submarine seismic events. A minor fracture appeared at about 550 pixels, and there appear to exist another hot spot in the Pacific Ocean at about 100 pixels. This interpretation is confirmed by the Signal Diagrams at the other frequencies that we have considered (3.9 μm, 6.5 μm and 10.7 μm) [Lin et al, 2016].

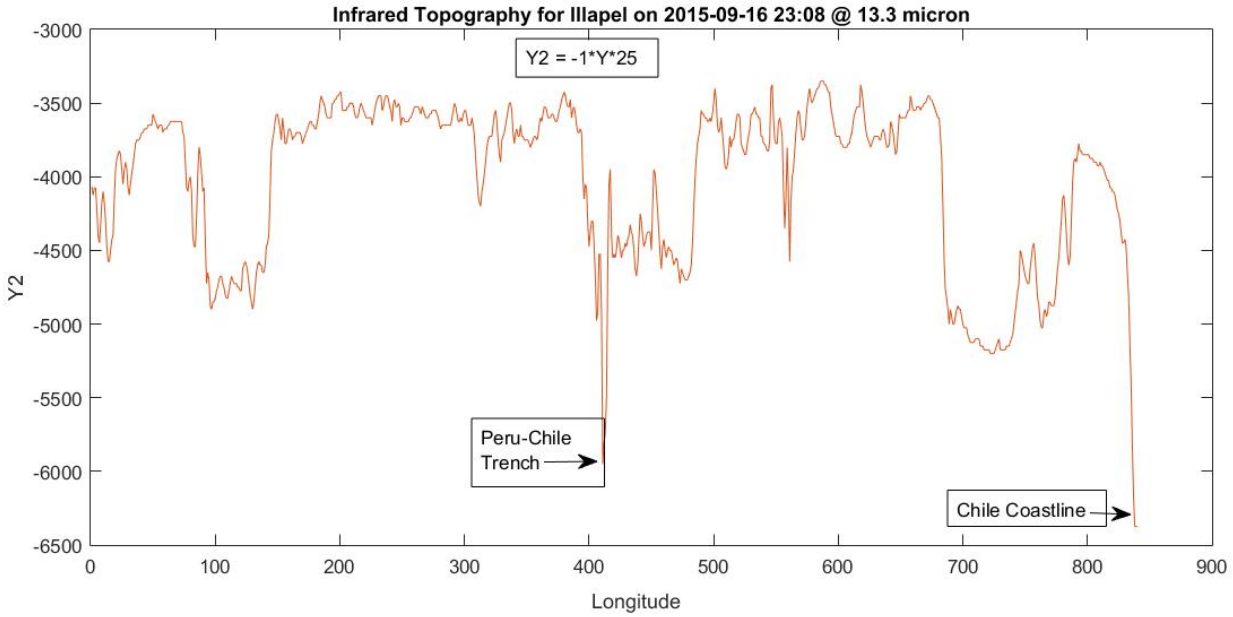

Fig. 5: Topographical Representation of Seabed at Illapel in Infrared Space

In Fig. 5 we show a topographical relief map in infrared space taken by the satellite on 2015-09-16 at 23:08 UTC, which is just 43 seconds after the eruption took place. This map is obtained by applying the following transformation (a mirror reflection) to the Signal Diagram:

$$Y2 = -1 * Y * \theta \qquad (1)$$

where Y is the Signal strength in pixels (Fig 3),
Y2 is the elevation in meters (Fig. 2)
and θ is a scaling factor (=25 in this case).

This transformation is possible since the elevation, or depth, is inversely correlated with the

temperature or heat content. The deeper the probe into the mantle, the higher is the temperature. While Fig. 3 depicts the physical feature of the terrain, Fig. 5 yields information on the *thermal* energy emitted. We emphasize, however, that the water molecules are stimulated by the heat of the volcanic eruption, in contradistinction to the case of tsunami radiation, where the water molecules are stimulated by mutual collisions at high speed. They, and not the volcanic output, give off this radiation.

We note that, in comparing Fig. 3 with Fig. 5, both figures exhibit the same gross topological features such as the Peru-Chile trench and the Chilean coastline, but the former was measured by sonic waves, whereas the latter was measured by electromagnetic radiation.

2. THE 30 MAY 2015 CHICHI-SHIMA EARTHQUAKE

On 30 May 2015 at 11:23 UTC a magnitude 7.8 seaquake with a deep focal depth of 664 km occurred WNW of Chichi-Shima, Japan at the latitude 27.8˚ N and 140.9˚ E. It centered in the vicinity of Torishima, which is a strategic location of considerable interest to geologists, since it is situated at the bisection point of the Izu-Ogasawara arc (Fig. 6).

The seaquake occurred within the interior of the Pacific plate, which subducts beneath Japan begginning at the Izu trench, a region marked by active volcanism. At this latitude, the Pacific plate moves westwards with respect to the Philippine Sea plate at the rate of 39 mm/yr. Structurally, the southern segment of the arc is underlain by thin crust of approximately 15 km on average, whereas the northern segment of the arc is underlain by an approximately 35 km thick crust. Andesitic magmas dominate volcanic eruptive products from the former and mostly basaltic lavas erupt from the latter. Where the crust is thin, melting occurs at relatively low pressures in the mantle wedge producing andesitic magmas. Where the crust is thick, the melting pressures are higher and only basaltic magmas tend to be produced. Since soon after subduction was initiated on earth most crust was thin, the rate of continental crust accumulation, which is andesitic in composition, would have been greatest. [Tamura et al, 2016].

The Izu-Ogasawara arc is produced by subduction of the Pacific plate beneath the Philippines Sea Plate. The subduction zone is characterized by rapid plate convergence and high-level seismicity extending to depth of over 600 km. It extends from 35˚N near Tokyo to 24˚N, the northern end of the Mariana arc. All volcanoes along the southern segment, except Sofigan and Nishinoshima, are submarine. We are, however, able to illuminate submarine features using electromagnetic radiation accompanying volcanic eruptions.

In Fig. 6 we show artist's version of the physical features of Japan [5], and in Fig. 7 the physical relief by sonic measurements. The Izu-Ogasawara arc is visible in Fig. 6 at approximately 140˚ longitude.

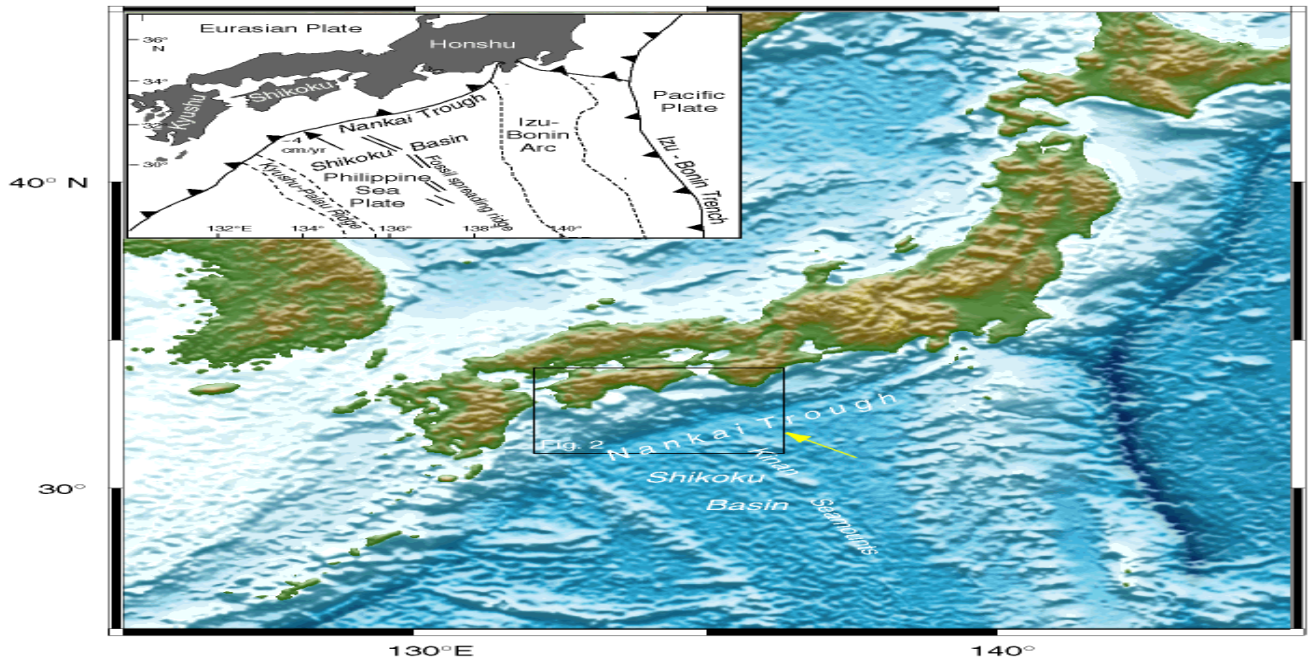

Fig. 6: Physical Features Map of Japan

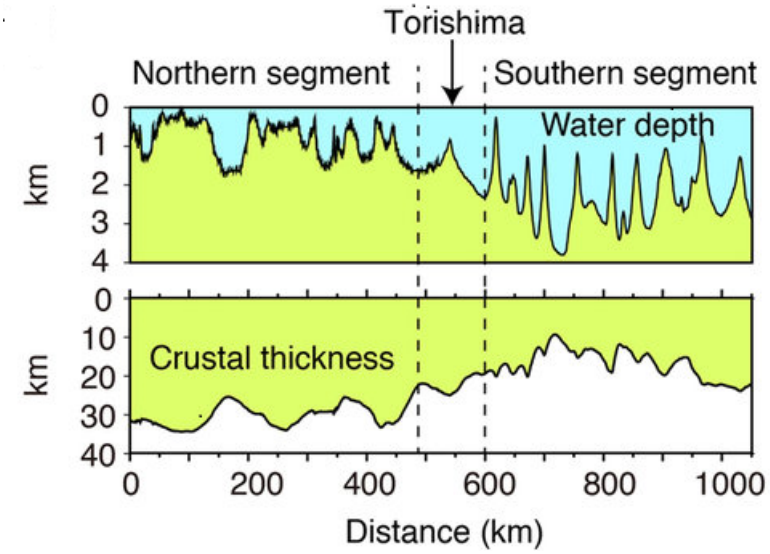

Fig. 7: Submarine Topology and Crustal Thickness at Tonishima

The Izu-Ogasawara arc is situated between a large depression, called the Shikoku Basin to the west, and the Japan Trench to the East. We shall show these features in the Infrared Topography derived from photographs obtained by the MTSAT-2 geostationary satellite at the time of the volcanic eruption. The satellite image shown below (Fig. 8) was obtained by the Japanese geostationary satellite MTSAT-2 on 2015-05-30 11:32 UTC at 10.8 μm wavelength [2].

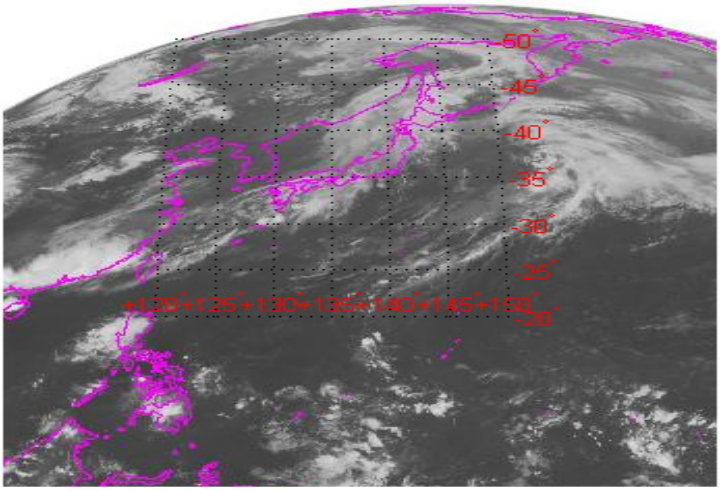

Fig. 8: Chichi-Shima Satellite image at 2015-05-30 11:32 UTC @10.8μm

The exposure is made 9 minutes after the occurrence of the volcanic eruption. At 10.8 μm, this is the long wavelength or IR-C (also classified as IR-4) band [Lin et al 2010; Lin and Sookhanaphibarn 2011; Lin et al. 2011; Lin et al. 2012; Lin et al. 2013; Lin et al. 2014]. The IR photon energy is between 0.001 and 1.7 eV. This is the atmospheric window covered by detectors such as HgCdTe and microbolometers. Satellite images in this frequency region can be used to determine cloud heights and types, to calculate land and surface water temperatures, and to locate ocean surface features. These infrared pictures are also used to depict ocean eddies or vortices and map currents. This infrared electromagnetic radiation resulted from the transition of the water molecules from the vibrational-rotational level (7 4 4) to the ground state (0 0 0). Quantum mechanically this corresponds to a [R L1 L2] (rotation, liberation) configuration conversion [Lin et al 2011; Lin et al 2012; Lin et al 2015; Lin et al 2015; Lin et al 2016]. Sulphur compounds, such as S-H or S-S, or Silicon compounds, such as Si-H or $Si-O_2$, that may be present in the volcanic output, do not emit photons at this frequency, which corresponds to a wave number of 925 cm^{-1}.

In order to be able to locate the epicenter on the satellite image we superimposed a geodetic grid onto the satellite image. The result is shown in Fig. 8. The algorithm to accomplish this is shown in Fig. 9.. We used the Robinson projection for the overlay. The Robinson projection is neither conformal nor equal-area, but is defined by a table at 5 degree intervals. It stretches the poles into long lines instead of leaving them as points. The straight parallels imply severe angular distortion at the high latitudes toward the outer edges of the map, a fault inherent in any pseudo cylindrical projection. Consequently, since distances are not conserved, it is possible that errors may be introduced. We attempt to minimize this error by choosing reference points as close as possible to each other, with the epicenter within the extent of these reference points, such as using two arbitrary points A and B with A:(30.145) degrees, or (296,193) pixels, and B:(25,135) degrees, or (242,225) pixels.

```
I = imread('chi-chi 2015-05-30 11_32 L=27.8 LN=140.5.jpg');
latlim = [-20 -50];
lonlim = [120 150];
figure, imshow(I);
axesm('Robinson','MapLatLimit',latlim,'MapLonLimit',lonlim,...
    'Scalefactor',[390],'falseeasting', [289],'falsenorthing',[356],...
    'Frame','on','Grid','on',...
    'mlinelocation', [5], 'mlinevisible','on',...
    'plinelocation',[5], 'plinevisible', 'on',...
    'mlabellocation',[5],'meridianlabel','on',...
    'plabellocation', [5],'parallellabel','on',...
    'fontcolor',[1 0 0],  'labelformat', 'signed',...
    'MLabelParallel', 'north','glinestyle', ':','PLabelMeridian','east',...
    'MeridianLabel','on','ParallelLabel','on')
%
```

Fig. 9: Algorithm to overlay geodetic lines on satellite image

By applying the MATLAB software as described in the Appendix of Ref. [Lin et al 2016] using the satellite image of Fig.8 as input, we obtain the East West Signal Diagram shown below (Fig. 10):

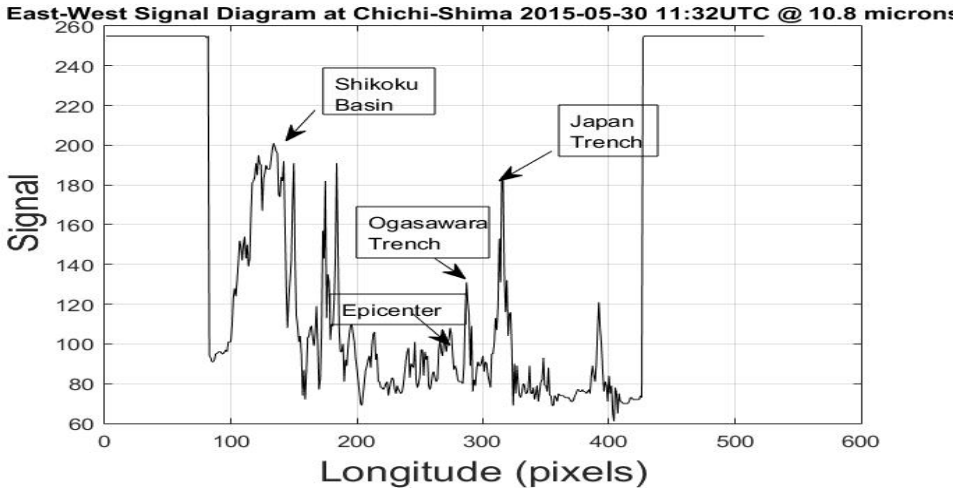

Fig. 10: Signal Diagram at Chichi-Shima 2015-05-30-11:32UTC @10.8μm

This Signal Diagram represents a slice across the satellite image in the East-West direction at the epicenter of the seaquake. The Signal on the y-coordinate is the pixel brightness. The spikes, therefore, represent the relative intensity of the infrared radiation emitted by water molecules at the corresponding locations. Since the Signal Diagram is not intuitively accessible to interpretation, we have, as before, converted it into the Infrared Topography.

At the boundary of subduction of the tectonic plates, a vast amount of heat is generated resulting in prominent spikes or jigged plateaus, some of which we have identified in the Infrared Topography, shown in Fig. 11 below, which is obtained by applying Eq. (1) to the Signal Diagram while setting the scaling constant to θ=0.1.

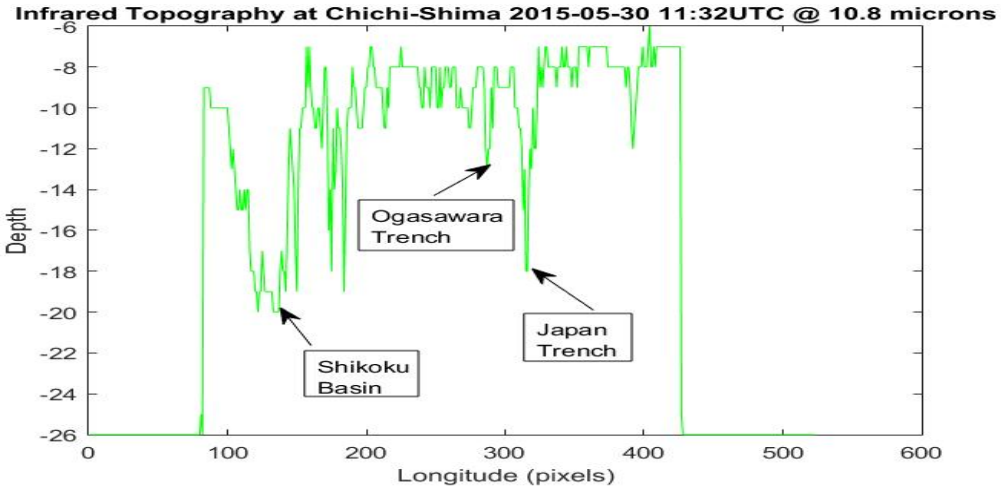

Fig. 11: Infrared Topography of Chichi-Shima, Japan

It is instructive to compare the Infrared Topography, Fig.10, with the Physical Topography, Fig.6. While both exhibit the same gross features, there are considerable differences, as to be expected.

The electromagnetic wave as a probing medium is capable of 'seeing' many 'fine structure', such as seamounts and thermal vents, as we have mentioned earlier. A thorough survey of the entire ocean will furnish us with detailed information on the geomorphology at active zones of the ocean both past and present.

3. CONCLUSION

In conclusion, in the case of Illapel, Fig2 is the physical relief obtained by sonic measurements using a naval vehicle, whereas Fig.4 is the Infrared Topography obtained by electromagnetic radiation using a geostationary satellite. In the case of Chichi-Shima, Fig.6 is the physical relief obtained by sonic measurements using a naval vehicle, whereas Fig.10 is the Infrared Topography obtained by electromagnetic radiation using a geostationary satellite. In conjunction, both methods will give us a more complete picture of the ocean's floor.

We have also shown that water molecules in the ocean, when stimulated by the heat of submarine volcanic eruption, will emit infrared radiation.

REFERENCES

[1] https://en.wikipedia.org/wiki/2015_Illapel_earthquake. Accessed 2016./9./20

[2] http://inventory.ssec.wisc.edu/inventory/ Accessed 2016/10/20

[3]
https://www.google.co.th/search?q=peru+chile+trench+diagram&sa=X&biw=1024&bih=674&tbm=isch&imgil=vLtAkJQk5LaNuM%253A%253Bx0oZviQnlRduxM%253Bhttps%25253A%25252F%25252Fcaninoesciproject.wordpress.com%25252F2013%25252F05%25252F09%25252Fsecond-stop-peru-chile-trench%25252F&source=iu&pf=m&fir=vLtAkJQk5LaNuM%253A%252Cx0oZviQnlRduxM%252C_&usg=__VY1HCOugm5w3Qljf-_FM2r8SKCo%3D&ved=0ahUKEwjCo8eFvpvPAhUEl5QKHfUYDqwQyjcILw&ei=HOHfV8KlMYSu0gT1sbjgCg#imgdii=vLtAkJQk5LaNuM%3A%3BvLtAkJQk5LaNuM%3A%3BH1DsiT3bnjhROM%3A&imgrc=vLtAkJQk5LaNuM%3A Accessed 2016/9/19

[4]
https://www.google.co.th/search?q=ocean+bottom+relief,+chile&biw=1024&bih=674&tbm=isch&imgil=XnCxNYPdY1kOwM%253A%253Bs01lr10WhhoM7M%253Bhttps%25253A%25252F%25252Fopentextbc.ca%25252Fgeology%25252Fchapter%25252F18-1-the-topography-of-the-sea-floor%25252F&source=iu&pf=m&fir=XnCxNYPdY1kOwM%253A%252Cs01lr10WhhoM7M%252C_&usg=__zeYR-MLDEVHsIrliLUYn_jBCoyo%3D&ved=0ahUKEwjMpIyTvZvPAhURtJQKHSKCCMYQyjcIIw&ei=LODfV8zeLpHo0gSihKKwDA#imgrc=jcxb8qdbEyxjSM%3A . Accessed 2016/9/20

[5]
https://www.google.co.th/search?q=ocean+bottom+relief,+japan&biw=1024&bih=710&tbm=isch&tbo=u&source=univ&sa=X&ved=0ahUKEwi-5-bK25jPAhXFm5QKHRFzAFEQsAQIHw#imgrc= wvGsBSZ6lsXfSM%3A .accessed on 2016/9/19

[6] Lin F.C., K. Na Nakornphanom, K. Sookhanaphibarn, and C. Lursinsap, 2010. "A New Paradigm for Detecting Tsunamis by Remote Sensing"; International Journal of Geoinformatics, Vol.6, No.1, March 2010, pp.19-30.

[7] Lin F.C. and K. Sookhanaphibarn, 2011. "Representation of Tsunamis in Generalized Hyperspace" Proceedings of the IEEE International Geoscience and Remote Sensing Symposium (IGARSS'11), Sendai/Vancouver, July 21, 2011. pp. 4355-4358

[8] Lin. F.C., K. Sookhanaphibarn, W. Choensawat and G. Pararas-Carayannis, 2016. "Detection of Tsunami Radiation at Illapel, Chile on 2015-09-16 by Remote Sensing"; Science of Tsunami Hazards, Vol.35, No.1, p.1

[9] Lin, F.C., K. Sookhanaphibarn, V. Sa-yakanit and G. Pararas-Carayannis, 2014. "REMOTE: Reconnaissance & Monitoring of Tsunami Events"; Science of Tsunami Hazards, Vol.33, No.2, pp.86-111

[10] Lin. F.C., K. Sookhanaphibarn, G. Pararas-Carayannis, 2015. "On The Frequency Spectrum of Tsunami Radiation"; Science of Tsunami Hazards, Vol.34, No.3, p.144

[11] Lin F.C., W. Zhu and K. Sookhanaphibarn, 2011. "Observation of Tsunami Radiation at Tohoku by Remote Sensing"; Science of Tsunami Hazards, Vol.30, No.4, pp. 223-232.

[12] Lin, F.C., W. Zhu and K. Sookhanaphibarn, 2012. "A Detail Analysis of the Tohoku Tsunami by Remote Sensing"; Proceedings of the IEEE International Geoscience and Remote Sensing Symposium (IGARSS'12), Munich, Germany, pp.1166-1169.

[13] Lin. F.C., W. Zhu and K. Sookhanaphibarn and P. Silapasuphakornwong, 2013. "REMOTE:-A Satellite Based Tsunami Early Warning Detection System"; Proceedings of the IEEE International Geoscience and Remote Sensing Symposium (IGARSS' 13), Melbourne, Australia, pp. 3694-3697.

[14] Pararas-Carayannis, G., 2010."Chile Earthquake and Tsunami of 27 February, 2010 - Evaluation of Source Mechanism and of Near and Far-field Tsunami Effects", International' Journal "Science of Tsunami Hazards", Vol. 29, No. 2, (2010)

[15] Tamura Y., Sato T., Fujiwara T., Kodaira S. and Nichols A., 2016. "Advent of Continents: A New Hypotheses: Scientific Reports 6"; Article #33517, Accessed 2016/10/25. http://www.odp.tamu.edu/publications/prosp/196_prs/196f01.html

ISSN 8755-6839

SCIENCE OF TSUNAMI HAZARDS

Journal of Tsunami Society International

Estimation of Coseismic Deformation from the Sea Level Measurements during the Mw 7.8 Earthquake of 13 Nov 2016 in New Zealand

A. Annunziato

Letter to the Editor, 15 Nov 2016

Dear Dr. Pararas-Carayannis

I would like to inform you that as a consequence of the large Earthquake and following Tsunami Mw. 7.8 that occurred two days ago in New Zealand, a phenomenon, that was already identified in the case of Mw. 9.0 Tohoku Tsunami has occurred again. Infact the sea level measurement present in the area of the larger deformation has shown a behaviour typical of an uplift of about **0.95 m**. In the case of the Japan event, instead, the sea level demonstrated a subsidence on the coasts of Japan, confirmed by GPS measurements.

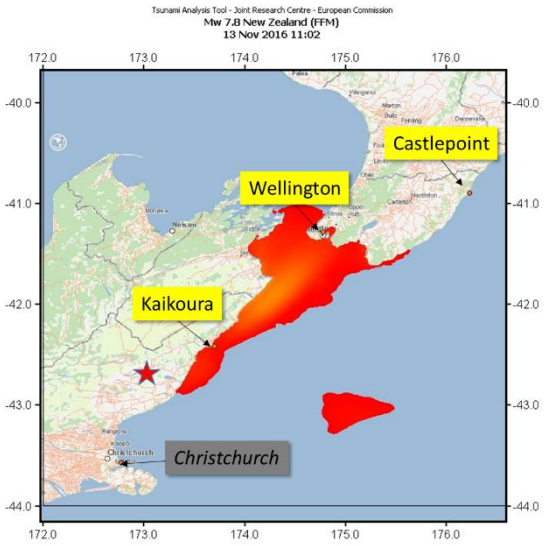

On 13th November at 11:03 UTC a Mw 7.8 earthquake occurred in New Zealand with epicentre 42.757°S 173.077°E. As a consequence a Tsunami was generated that was measured by all the sea level stations in the area. The closest stations in the area are indicated in the map aside and are: Kaikoura, Wellington and Castlepoint. The tide gauge of Christchurch was unavailable at the time of the event.

The largest sea level change occurred in Kaikoura whose measurement level toped to about 1.5 m above the normal tide level.

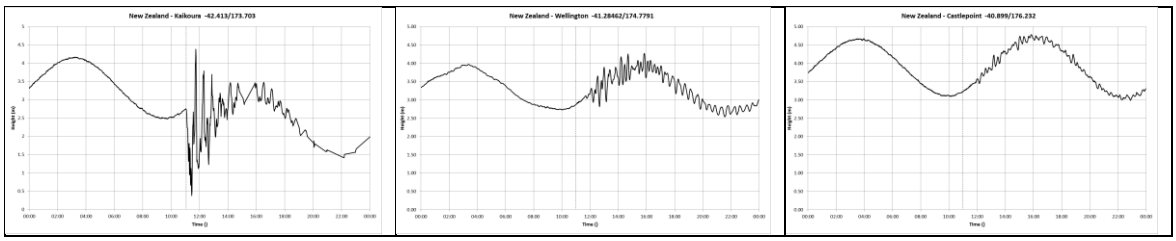

What is interesting is that following the sea level measurements in Kaikoura before and much later after the event it is possible to recognize that the station shows a sea level change corresponding to about **0.95 m**. As it can be seen on the next figure the sea level in the long term is about 0.95 m lower than it was before the event: the dash curve represents the expected sea level, following the normal tide , if the event had not occurred. This means that the sensor of the tide gauge has been lifted by the

same amount (i.e. coseismic uplift). The measurement in the other tide gauge locations did not show any significant long term deformation.

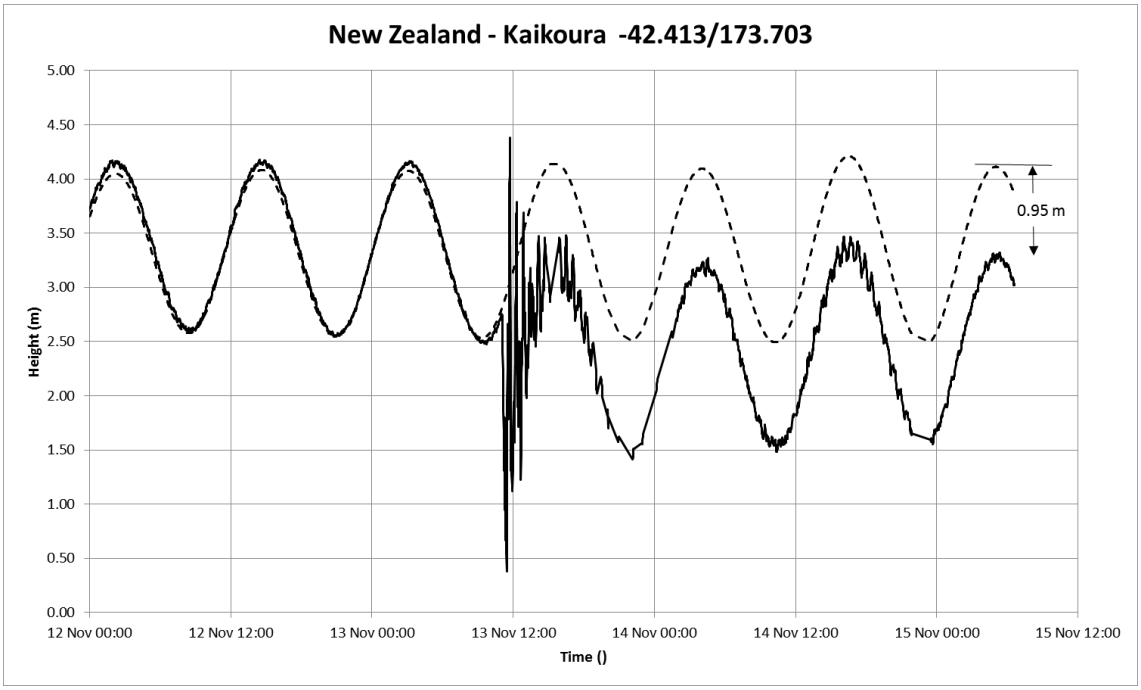

In the case of Japan event a similar behaviour was present in several Japanese tide gauges and measurement sites, as shown in Annnunziato (2012)[1]. In that case the sea level increase after the event identified a subduction, confirmed by GPS measurements in the area.

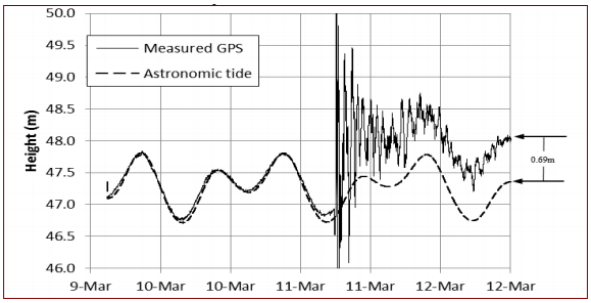

North Myagi sea level measurement after the Tohoku event of 2011 in Japan

(From Annunziato 2012 paper)

It will be interesting in the case of New Zealand, to compare this value obtained by the sea level with values obtained by other measurements, as GPS ones or satellite radar spectrometry, when available.

Applying the correction factor of 0.95 m to the measurement signal after the event, the resulting final curve of the sea level is shown below.

[1] A. Annunziato – 'SEA LEVEL SIGNALS CORRECTION FOR THE 2011 TOHOKU TSUNAMI' - http://tsunamisociety.org/312Annunziato.pdf (2012)

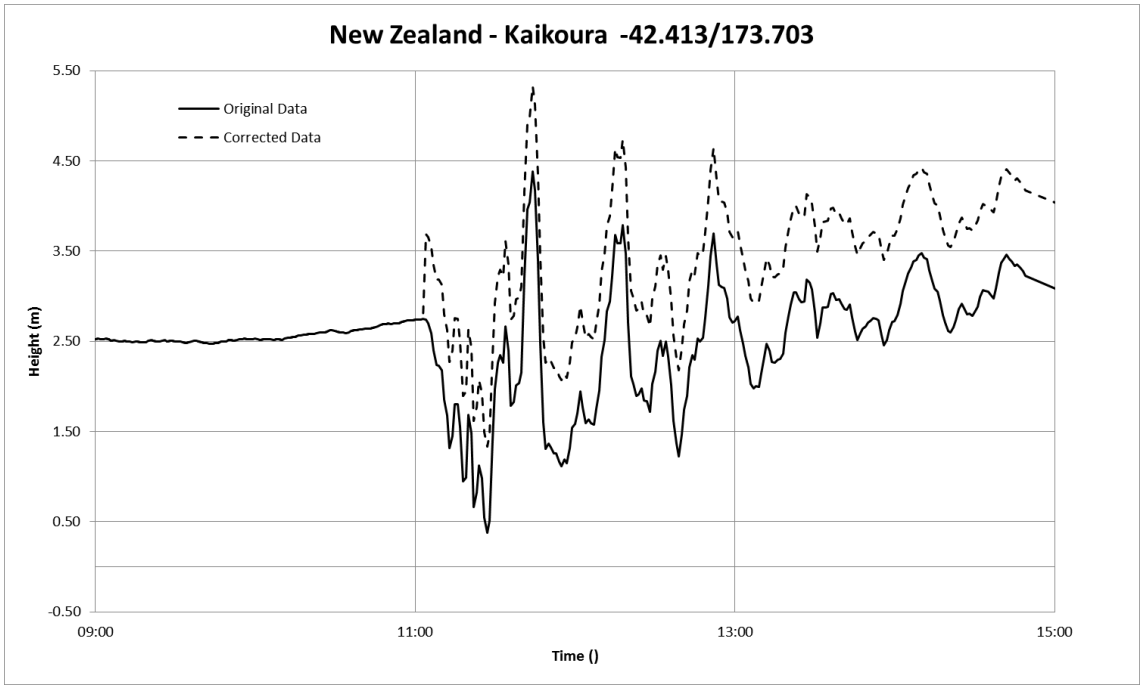

Measured (solid line) and Corrected data (dash line) for Kaikoura

The next figure indicates the difference with the expected tide, i.e. the net sea level increase above the expected tide level. The sea level therefore increase was about **2.3 m** above the normal sea tide.

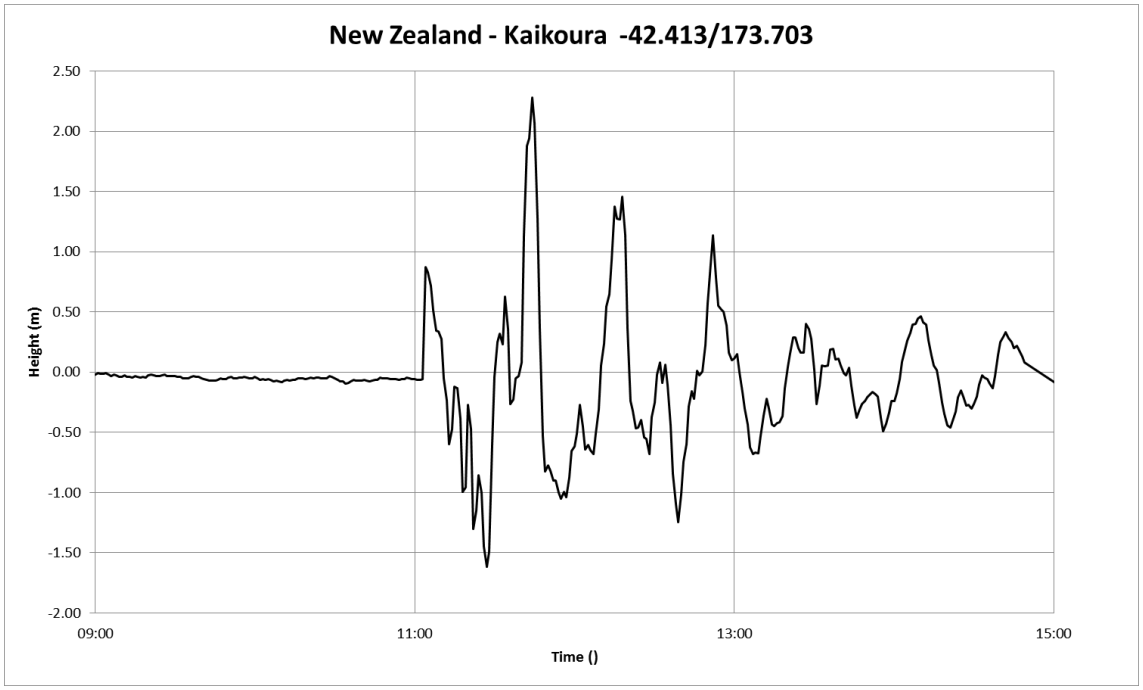

Net sea level increase over the expected tide, after the correction of 0.95 m after time 0

ISSN 8755-6839

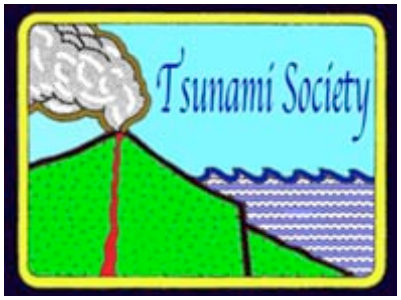

SCIENCE OF **TSUNAMI HAZARDS**

Journal of Tsunami Society International

Volume 35 **Number 3** **2016**

Copyright © 2016 - TSUNAMI SOCIETY INTERNATIONAL

TSUNAMI SOCIETY INTERNATIONAL, 1741 Ala Moana Blvd. #70, Honolulu, HI 96815, USA.

WWW.TSUNAMISOCIETY.ORG